TECHNISCHE UNIVERSITÄT MÜNCHEN

Lehrstuhl für Theoretische Chemie

Investigations into Superhard Nitride- and Oxide-based Nanocomposites by Means of Combined *ab initio* DFT and Thermodynamic Calculations

Shuhong Sheng

Vollständiger Abdruck der von der Fakultät für Chemie der Technischen Universität München zur Erlangung des akademischen Grades eines

Doktors der Naturwissenschaften

genehmigten Dissertation.

Vorsitzender: Univ. -Prof. Dr. K. Köhler
Prüfer der Dissertation:

1. Univ. -Prof. Dr. Dr. h.c. St. Vepřek (i.R)
2. Univ. -Prof. Dr. W. Domcke

Die Dissertation wurde am 04.11.2009 bei der Technischen Universität München eingereicht und durch die Fakulität für Chemie am 08.01.2010 angenommen.

Abstract

We studied the de-mixing properties of the ternary Zr-Al-N, Zr-Si-N, Al-Si-N and Zr-Al-O systems with the goal to find if they may be suitable candidates for new superhard nanocomposites. For this purpose we used a combined *ab initio* density functional theory (DFT) and thermodynamic modelling based on the sublattice solution model, which has been recently developed by Zhang and Veprek and applied to the study of several ternary nitride systems that are applied in the industry as wear protective coatings on tools, such as metastable solid solutions $Al_{1-x}Ti_xN$, $Al_{1-x}Cr_xN$ or superhard nanocomposites nc-TiN/a-Si_3N_4, nc-$Al_{1-x}Ti_xN$/a-Si_3N_4 or nc-$Al_{1-x}Cr_xN$/a-Si_3N_4. The important advantage of the combined method, as compared with the quantum molecular dynamic (e.g. Car-Parrinello) approach, is orders of magnitude shorter computing time needed (approximately a factor of 10^5).

For the *ab initio* DFT calculation we used the well tested Vienna Ab-initio Simulation Program (VASP). In order to verify the reliability of our calculations and of the potentials used, we first calculated, by means of *ab initio* DFT, the fundamental properties, such as the dependence of the total energy on volume, lattice constant, bulk modulus, its derivative and cohesive energy of the relevant, stable binary compounds ("terminal phases"), such as fcc(NaCl)-ZrN, hcp(ß)-Si_3N_4 and others, and compare them with published data. Because in all cases very good agreement has been obtained, these calculations were extended to the ternary solid solution phases of interest, and to their corresponding hypothetical terminal phases (e.g. hcp(ß)-Zr_3N_4, fcc(NaCl)-SiN etc.), which have to be used in the DFT calculations in order to preserve the given crystal symmetry, because the calculation are done in the reciprocal space. From the formation energy calculated by the *ab initio* DFT at 0 K as function of the composition, we determined the composition-dependent interaction parameter which has been then used in the sublattice solution model to calculate the Gibbs free energy of the mixed solid solution phases at ambient pressure and different temperatures.

The results were then used to study, by means of the thermodynamic sublattice solution model, the phase stabilities and de-mixing properties of the solid solutions with the appropriate structures. Finally, the temperature-composition diagrams were constructed to determine the spinodal and binodal regimes of each of the above mentioned systems. We have also investigated the effect of different temperature dependence of the interaction parameter on the final results. It has been found that the exponential dependence yields the most reliable results whereas using T-independent interaction parameter, as done in several recent papers of other researchers, is obviously incorrect. Based on the calculated chemical spinodal and considering the effect of the interfacial lattice misfit elastic energy, we discussed the possibilities of the occurrence of "coherently" spinodal phase segregation and of the formation of stable nanocomposites in the above mentioned systems.

In the second part of this work, the mechanical properties of the stable terminal phases and the metastable $Zr_{1-x}Al_xN$ solid solution have been studied by calculating the stress-strain curves in tension (relevant for crack growth and brittle fracture) and shear (relevant for plastic deformation) for several slip systems. The results for bulk phases showed only a small reduction of the ideal strengths for the ternary solid solution as compared with the pure binary terminal phases. Afterwards, the calculations have then been extended to heterostructures consisting of few nm thick slabs of ZrN with one monolayer thick pseudomorphic AlN interface. In contrast to the TiN/1 ML SiN_x/TiN system, no enhancement of the strength has been found for the ZrN/1 ML-AlN/ZrN heterostructures. These findings are in agreement with experimental results because hardness enhancement has been reported for the TiN/1 ML-SiN_x/TiN and ZrN/1 ML SiN_x/ZrN heterostructures, but not for the VN/1-ML AlN/VN ones.

Acknowledgments

I would like to thank my supervisors, Prof. Dr. Stan Veprek and Prof. Dr. Wolfgang Domcke for their sincere supervision, guidance and valuable discussions throughout this work as well as for their encouragement and support in science and different aspects of life. Without their kind help it is not possible for me to overcome many difficulties along the way to finish the work.

My thanks are also to Dr. Ruifeng Zhang for introducing me into the field of first principles calculation and many valuable advices in this work.

I am also grateful to Dr. Maritza Veprek-Heijman for much help and support in the work and living throughout the last three years.

Thanks to LRZ (Leibniz-Rechenzentrum) for providing the facility of this work.

My special thanks are to my parents Zengpo Sheng and Fenguzhi Wang for their never ending encouragement and support through my life.

Contents

Chapter 2: Computational Methods Used

Chapter 3: Results

Chapter 1: Introduction

The present work attempts to contribute to the understanding of the formation and properties of superhard nanocomposites, which were developed at the former Institute for Chemistry of Inorganic Materials of the Technical University Munich during the last 14 years [Veprek et al. 95] [Veprek et al. 96] (see also reviews [Veprek 99] [Veprek et al. 05]), and introduced into large-scale industrial applications by the company SHM (Czech Republic) [Veprek & Jilek 02] [Jilek et al. 03] [Jilek et al. 03b] [Holubar et al. 00] and PLATIT (Switzerland) [Cselle 05] [Cselle 05b] [Veprek & Veprek-Heijman 08].

Nanocomposites comprise at least two phases: either a nanocrystalline and amorphous, or two nanocrystalline phases. The two phases should be incommensurable, such as e.g. cubic (c-BN) and wurtzite (w-BN) boron nitride [Durbovinskaia et al. 07], strongly immiscible and refractory, to ensure high thermal stability of the nanostructure. With the decrease of the crystallite size, the strength and hardness of the materials increases due to the decrease of dislocation activity by the Hall-Petch strengthening [Hertzberg 89]. However, when the crystallite size reaches about 10 nm (the "strongest crystallite size") softening is found due to increasing grain boundary shear with a further decrease of the size [Argon 08]. The overall hardness enhancement achievable by this "nano-size" mechanism is about a factor of ≤ 2. In the superhard nanocomposites developed by Veprek et al., the grain boundary shear is hindered by the formation of about 1 monolayer (1 ML) thick SiN_x interface, that is strengthened by valence charge transfer from the transition metal nitride. Consequently, a much higher strengthening can be achieved with crystallite size decreasing to 3-4 nm and hardness reaching > 100 GPa, more than diamond.

The development of these novel superhard nanocomposites has been, so far, done on the basis of the generic design principle as formulated in [Veprek et al. 95]. Accordingly, the formation of a nanocomposite occurs due to self-organization upon spinodal phase segregation in strongly immiscible quasi-binary systems, such as stoichiometric, hard transition metal nitride (TiN, W_2N, VN, ZrN, $(Ti_{1-x}Al_x)N$, $(Al_{1-x}Cr_x)N$, …) in combination with a covalent nitride (Si_3N_4, BN). During their preparation, a sufficiently high pressure of nitrogen of $\geq 10^{-2}$ mbar is needed to provide the thermodynamic driving force, and a high temperature of ≥ 550 °C is required to assure a sufficiently fast diffusion that enables the phase segregation to be kinetically completed during the preparation [Veprek et al. 95] [Veprek et al. 96] [Veprek 99] [Veprek et al. 05] [Zhang & Veprek 06]. Nanocomposites prepared in this way consist of 3-4 nm small nanocrystals of the hard transition metal nitride "glued" together by about 1 monolayer (1 ML) of the covalent nitride. Based on their experimental findings, Veprek et al. postulated that the self-organization occurs by the spinodal decomposition of the ternary phases (e.g. $Ti_{1-x}Si_xN$), and that the 1 ML interfacial layer is stabilized by some, at that time unknown mechanism, because in the optimum composition, where maximum hardness is achieved, the crystallite size is at a minimum, i.e. the specific interfacial area reaches a maximum [Veprek et al. 95] [Veprek et al. 96] [Veprek 99] [Veprek et al. 05]. In collaboration with Professor A. S. Argon (Massachusetts Institute of Technology, Cambridge, USA), the researchers also explained the unusual combination of mechanical properties, such as high hardness exceeding 100 GPa (diamond 70 – 100 GPa), high elastic limit and high resistance against brittle fracture, by the ideal behavior of an almost defect-free material [Veprek & Argon 02] [Veprek et al. 03]. They also showed the importance of high purity in these nanocomposites, because oxygen impurities of ≥ 0.1 at. % strongly degrade the hardness [Veprek et al. 05] [Veprek et al. 05b]. As an explanation of this detrimental role of oxygen, both size and electronic effect, i.e. weakening of neighbor bonds by valence charge transfer to oxygen, has been suggested [Veprek et al. 05b]. Therefore, the very high hardness of ≥ 100 GPa has been achieved only in ultra-pure nanocomposites.

Until about 2006, the theoretical understanding of the formation and properties of the superhard nanocomposites has been limited to the above quoted papers. Using the sublattice thermodynamic model and experimentally determined interaction parameter, Zhang and Veprek have shown in 2006 that the phase segregation in the Ti-Si-N system indeed proceeds by spinodal mechanism [Zhang & Veprek 06]. More recently, these researchers developed new computational approach based on a combined *ab initio* density functional theory (DFT) and thermodynamic modeling [Zhang & Veprek 08] [Zhang & Veprek 07] [Zhang & Veprek 07a] [Zhang & Veprek 07b], and applied it to several ternary systems including Ti-Si-N. In such a way they confirmed that the phase segregation occurs by spinodal mechanism in this system, in agreement with the semi-empirical calculations in [Zhang & Veprek 06]. In collaboration with Prof. Argon [Veprek et al. 07], they also explained the high hardness of ≥ 100 GPa, reported earlier for nc-TiN/a-Si_3N_4/$TiSi_2$ nanocomposites (see [Veprek et al. 05] and references therein). They used the values of the shear strength of the TiN/1 ML-SiN_x/TiN sandwich calculated by the *ab initio* DFT method, Sachs's average of the shear resistance of randomly oriented nanocrystals, Tabor's ratio between the yield stress and hardness, and the pressure-enhancement of the flow stress in order to show that hardness in excess of 100 GPa should be achieved in many similar systems [Veprek et al. 07]. The reason of this surprising result is the strong enhancement of the strength of 1 ML interfacial layer, the fact that the 3-4 nm small nanocrystals which are free of flaws deform only elastically, their random orientation which enhances the shear resistance as compared with a single crystal, and the pressure enhancement of the flow stress. These conclusions were more recently further supported by the non-linear finite element modeling [Veprek-Heijman et al. 09].

The strong enhancement of the strength of a sandwich, consisting of TiN and 1 ML interfacial SiN_x, is due to partial transfer of the valence charge from TiN to that interface. Such a sandwich displays significantly higher shear strength than bulk SiN_x [Hao et al. 06] [Hao et al. 06b] [Veprek et al. 07]. During the last two years, Zhang et al. applied the *ab initio* DFT method for the calculation of de-cohesion and ideal shear strength of variety of crystalline phases of silicon nitride [Zhang et al. 07d], aluminium nitride [Zhang et al. 07b], rhenium diboride [Zhang et al. 07c] and boron nitride [Zhang et al. 08c], and to the study of the mechanism of the B3-to-B1 and B4-to-B1 transition in AlN [Zhang et al. 07] [Zhang et al. 08]. Similar calculations have been recently published by other researchers for different hard and superhard materials. Here we focus only on papers related to the subject of the present work.

Hao et al. [Hao et al. 06] [Hao et al. 06b;c] conducted extensive studies of the TiN/Si_3N_4 –like system[1] by means of *ab initio* DFT using large cells and supercomputing facilities available at the University of Sydney, and obtained similar results as Zhang et al. who studied the fcc-TiN/1 ML-SiN/TiN system. Hao et al. have shown that also the de-cohesion strength of a 1 ML-Si_3N_4 interfacial layer in the $TiN/Si_3N_4/TiN$ sandwich is higher than the de-cohesion strength of bulk Si_3N_4 crystal, thus confirming the strengthening of such interface as discussed above. However, for a theoretical modeling of plasticity in the nanocomposites, the knowledge of the shear strength, as calculated by Zhang et al., is important because plastic deformation occurs in shear. Based on the calculation of electronic structure, Hao et al. have confirmed the detrimental effect of oxygen impurities, which substitute nitrogen within the interfacial Si_3N_4 thus weakening the neighbour bonds. Interestingly, they could show that this effect is absent in the case of a titanium silicide interface because in that case the oxygen is incorporated as interstitials within the metallic TiN nanocrystals. These results explained why the highest hardness has been found in nc-TiN/a-Si_3N_4/$TiSi_2$ nanocomposites with total oxygen impurity of about 100 ppm, where the silicide acts as a "getter" of oxygen, thus removing it from the Si_3N_4 interface.

The aim of the present work is to apply and extend the theoretical modeling of Zhang et al. to new ternary systems in order to investigate to what extent do the results obtained for the TiN/SiN_x system apply also for other ones, and to identify which of them may be suitable for the development of new super- and ultrahard nanocomposites. An important part of the work will be

---

[1] Depending on the crystallographic nature, the exact stoichiometry of 1 ML interface may somewhat differ form the Si_3N_4 one. For simplicity we use her the term "Si_3N_4".

also a deeper clarification of the mechanism of the strengthening of the 1 ML of Si_3N_4 and possibly other interfacial layers consisting of a covalent nitride. The present status of the experimental and theoretical work in the field of hard and superhard coatings will be briefly summarized in the next section, followed by the specification of the goal of the present work in Sect. 1.2.

1.1 The present status of the experimental and theoretical work in the field of hard and superhard coatings

During the last 3 decades, a large effort has been devoted to the development of new super- and ultrahard materials (see e.g. [Liu & Cohen 90] [Sproul 96] [Teter 98] [Veprek 99] [Haines et al. 01] [Brazhkin et al. 02] [Kaner et al. 05] and references therein), because of fundamental scientific interest and their possible applications [Veprek et al. 05] [Jilek et al. 03] [Veprek & Veprek-Heijman 08]. Besides of the intrinsically superhard materials, such as diamond ($H \approx 70 - 100$ GPa) and cubic boron nitride ($H \approx 48$ GPa) [Veprek 99], the research work focused on extrinsically superhard materials, such as heterostructures [Barnett 93] [Barnett & Madan 98] [Clemens et al. 99] and the nanocomposites, in which the hardness of the nano-structured system is significantly higher than that given by the rule-of-mixtures.

Wear protective coatings made of transition metal nitrides and carbides with hardness between about 20 and 30 GPa are commercially available and used because of the combination of a high hardness, high thermal stability and a relatively high-temperature strength [Zhang et al. 07d] [Sundgren & Hentzell 86] [PalDey & Deevi 03]. TiN, which has been introduced as protective coating on tools in 1980s, is, during the last 4 – 6 years, being replaced by ternary Me-Al-N (Me = transition metal) systems, such as $Ti_{1-x}Al_xN$ [Münz 86] [Knotek et al. 86] [Jehn et al. 86] [Münz 90] [Tanaka et al. 92] [Suzuki et al. 00] [Adibi et al. 91] [Jilek et al. 03b] [Zhang & Veprek 07] [Mayrhofer et al. 06] [Mayrhofer et al. 06b] [Mayrhofer et al. 03], $Al_{1-x}Cr_xN$ [Knotek et al. 91] [Hofman & Jehn 90] [Vetter et al. 98] [Sanjines et al. 02] [Kawate et al. 03] [Schram et al. 04] [Park & Baik 05] [Reiter et al. 05] [Hasegawa et al. 05] [Kalss et al. 06] [Willmann et al. 06] [Zhang & Veprek 07b] [Reiter et al. 07] and others, because of their higher hardness and oxidation resistance. Therefore, these coatings were most widely investigated, whereas very limited studies have been dedicated to the Zr-Al-N, Zr-Si-N and Al-Si-N systems, which are the primary subject of the present work from the scientific point of view, as well as potential candidates for new superhard nanocomposites. ZrN has a lower coefficient of friction than TiN and other transition-metal nitrides, and is relatively hard [Holleck 86] [Berg et al. 00], which makes it interesting as protecting coatings on tools. However, its poor oxidation resistance is hampering a broader range of applications. Therefore its alloying with Al was suggested in order to improve the oxidation resistance and possibly also the mechanical properties [Li 06]. Recent experimental studies have shown that the fcc (NaCl-type)-$Zr_{1-x}Al_xN$ solid solution exists for $0< x<0.43$, and the hardness increases from 21 GPa to 28 GPa when the Al fraction increase from $x = 0$ to 0.43 [Lamni et al. 05]. With further addition of Al, hcp (ZnS-type)-AlN appears and the hardness of the coatings decreases. $Zr_{1-x}Si_xN$ coatings on machining tools have shown an excellent cutting performance, but no detailed investigation into their performance has been done [MACHERENA 07].

In the past decades, theoretical investigations of hard transition metal nitrides attracted much interest. These studies include mainly the first principles *ab initio* DFT calculations [Hugosson et al. 01] [Hugosson et al. 03] and empirical thermodynamic modeling [Spencer 98] [Spencer 01]. The advantage of the *ab initio* method is the fact that no experimental input data are needed, and a much deeper physical insight can be obtained. However, its application to a larger number of different systems is limited to the ground state properties at 0 K, because the quantum mechanics and dynamics computations, such as the Car-Parrinello method, require much larger CPU time (for our case we estimate by a factor of 10^5 or more). Furthermore, because the exact *ab initio* DFT modeling of solids is based on reciprocal space methods, only perfect crystal structures can be considered which, in turn limits the composition range that can be treated. The thermodynamic modeling is much simpler and faster, it can cover the whole composition range and account for variety of chemical activities at different temperatures. However, the calculations of ternary solid solutions require the knowledge of the relative stability of different structures of the solution as well as of the terminal binary phases, and of the interaction parameter between the involved binary phases. Such experimental data are not available for strongly immiscible systems.

These problems have been solved by the above mentioned combined method of Zhang and Veprek, which applies the *ab initio* DFT calculations for the determination of the relative lattice stabilities and interaction parameters of the involved phases that are then used in the thermodynamic modeling. This method has been already applied to the $Ti_{1-x}Si_xN_y$ [Zhang & Veprek 06] [Zhang & Veprek 08], $Ti_{1-x}Al_xN$ [Zhang & Veprek 07], $Cr_{1-x}Al_xN$ [Zhang & Veprek 07b] and $Ti_{1-x}B_xN$ [Zhang et al. 08b] systems.

Because of the limited experimental data available for the Zr-Al-N, Zr-Si-N and Al-Si-N systems, it is of interest to study their phase stability as well as the thermal decomposition mechanism of the ternary solid solution phases by means of a combined *ab initio* DFT calculations and thermodynamic modeling. This will enable to predict their properties, the possibility of the formation of superhard nanocomposites by spinodal phase segregation, and to compare them with other systems. An important question to be addressed is if the Al-containing systems can also form superhard nanocomposites with AlN as interfacial phase instead of SiN_x. It is known that few monolayers thin interfacial AlN between TiN crystals forms pseudomorph cubic phase with diffuse interphase. The study of the Zr-Si-N system is motivated by the expectation that, by analogy to Ti-Si-N, it may also form superhard nanocomposites with high hardness and high oxidation resistance, and possibly lower coefficient of friction. In the case of the Al-Si-N system, for which only limited experimental studies are available [Pelisson et al. 07], we want to address also the question as which of the possible interfacial phases (1 ML-SiN_x or 1 ML-AlN) will provide larger strengthening. This should be complemented by similar studies on oxides, such as Zr-Al-O in order to elucidate if superhard nanocomposite can be prepared also in these systems. The oxide-based superhard nanocomposite coatings would offer a great advantage because of their essentially "unlimited" oxidation resistance. High oxidation resistance is important in dry and minimum lubricant, hard and fast machining where the oxidation of the coatings is the dominant wear mechanism [Veprek & Veprek-Heijman 08].

The results of the calculations of the ideal shear strength of these different sandwiches and of the possible strengthening of the interfacial phases will be compared with similar data reported by Zhang et al. [Zhang et al. 07d] [Veprek et al. 07] [Zhang et al. 09] and Hao et al. [Hao et al. 06] [Hao et al. 06b;c] on the Ti-Si-N system in order to obtain a deeper understanding of the strengthening phenomena.

1.2 The goal of the work

The goal of the present work is divided into the following work packages:

- In-depth studies of combined *ab initio* DFT and thermodynamic modelling for the calculations of the free energy of the mixed pseudo-binary nitride systems and of the possibility of spinodal decomposition. This includes the phase stability and phase segregation in the ternary Zr-Al-N systems by *ab initio* DFT and thermodynamic calculation in order to verify if the system is "chemical spinodal". Using a simple model to estimate the elastic strain energy it will be verified if the phase segregation can be also coherent spinodal.

- Based on the experience obtained with Zr-Al-N system, the work will be extended to the Zr-Si-N and Al-Si-N nitride and Zr-Al-O oxide systems that are of interest from the scientific point of view and may be also important for large-scale industrial applications. For systems, which show sufficiently pronounced chemical spinodal curve, the interfacial strain energy (coherent, semi-coherent and incoherent interfaces) will be included into the combined *ab initio* DFT and thermodynamic modelling, in order to clarify its effect on the mechanism of the phase segregation (spinodal vs. nucleation and growth).
- The mechanical properties of the stable and metastable phases involved in these systems will be studied by using the *ab initio* DFT method to calculate the stress-strain relationships in order to obtain the ideal tensile de-cohesion and shear strength of the binary and ternary phases. In order to further improve the understanding of the strengthening mechanism in the nanocomposites, such relationships will be calculated for sandwiches consisting of 6-8 monolayers (ML) of the transition metal nitride with 1 ML of pseudomorphic interfacial AlN phase. It should be clarified if the strengthening, as reported for the TiN-Si_3N_4 system by Hao et al. and Zhang et al., also applies to other systems, and if it scales with the enhancement of the negative valence charge density at that interface.
- The results will be analyzed in terms of changes of the valence charge density at the interfacial monolayer. Comparison of these data and their correlation with the strengthening (or weakening?) obtained in all these systems should provide a deeper understanding of this new and interesting phenomena.

Chapter 2: Computational Methods Used

2.1 Brief description of the DFT and VASP code

2.1.1 The DFT method

The *ab initio* methods are based on the solution of Schrödinger's equation for the many-body problem in order to obtain the electronic structure [Martin 04] [Lazar 06]. Since the wave function of many-particle system depends on the coordinates of each particle and their interactions, the complexity of this approach is obvious. Because the computing time strongly increases with increasing number of the atoms in the system, one has to design the cell to be calculated as small as possible, but yet representative for the given system and problem. Furthermore, the calculations being conducted in this work are limited to temperature of 0 K because considering the thermal movement of the atoms within the framework of quantum molecular dynamic (e.g. Car-Parrinello) increases the computing time by several orders of magnitude.

The DFT is based on theorems of Hohenberg and Kohn [Hohenberg & Kohn 1964], who demonstrated that the total energy E of a system of interacting particles in ground state is completely determined by the electron density ρ. Therefore, the total energy can be expressed as a function of the electron density, $E(\rho)$, which satisfies the variational principle. Kohn and Sham [Kohn & Sham 1965] derived more rigorous functional equations in terms of a simplified wave function concept, separating the contributions to the total energy as

$$E(\rho(r)) = T_s(\rho) + \int V(r)\rho(r)dr + \frac{1}{2}\int \frac{\rho(r)\rho(r')}{r-r'}drdr' + E_{xc}(\rho(r)) \,. \qquad (2.1.1)$$

Here, T_S represents the kinetic energy of a non-interacting electron gas, V is the potential of the nuclei. The third term corresponds to the electron-electron interaction and the last one, E_{xc}, comprises the many-body particle interactions.

Introducing the Kohn-Sham orbitals, the solution of the variational Euler equation corresponding to the functional of equation 2.1.1 results in Schrödinger-like equation for the orbitals $\psi(r)$

$$\left(-\frac{\hbar^2}{2m}\nabla^2 + V_{eff}(r)\right)\psi(r) = \varepsilon\psi(r) \qquad (2.1.2)$$

These, well known Kohn-Sham equations are then solved under approximations described below. Equation 2.1.2 transforms the many-particle problem into a problem of one electron moving in an effective potential

$$V_{eff}(r) = V(r) + \int \frac{\rho(r')}{|r - r'|} dr' + \frac{\delta E_{xc}(\rho)}{\delta \rho} \qquad (2.1.3)$$

which describes the electronic field induced by the other particles. The actual role of the auxiliary orbitals is to build up the true ground state density by summing over all occupied states,

$$\rho(r) = \sum_{occ} \psi^{*}(r)\psi(r) \qquad (2.1.4)$$

The reformulation of Kohn and Sham provides a suitable basis, which transforms the functional equation into a set of differential equations, which can be solved in a self-consistent manner. The crucial point for actual applications is the functional E_{xc}, which has no analytical expression, and therefore requires approximations. The historically first and widely used approximation is the local density approximation (LDA), which is based on the assumption that the exact exchange-correlation energy can, at the point r, be locally replaced by the expression for homogeneous electron gas,

$$E_{xc}(\rho) = \int \rho(r)\varepsilon_{xc}(r)\rho(r)dr \qquad (2.1.5)$$

in which $\varepsilon_{xc}(\rho)$ is the exchange-correlation energy per particle in that gas. The function $\varepsilon_{xc}(\rho)$ has to be approximated as well, but this can be done accurately by computer simulations. Several methods have been utilized to parameterize the many-body interactions of a homogeneous gas of interacting electrons, for instance by many body perturbation theory or by quantum Monte-Carlo techniques. Because the differences between the different parameterizations are small, $\varepsilon_{xc}(\rho)$ can be considered as a well-defined quantity.

Although it yields in many cases surprisingly reliable results, LDA is a relatively crude approximation. Therefore, it is nowadays considered not to be accurate enough for all problems. Various improvements have been proposed beyond the simple LDA assumption, taking into account the gradient of the electron density within the framework of the generalized gradient approximation (GGA) [Perdew et al. 1992]. In many applications, GGA provides a substantially improved description of the ground state properties, in particular for 3d transition metals, as demonstrated e.g. for the ground state of iron [Singh et al. 1991].

Ab initio DFT methods have great capabilities and are widely applied, in particular since the last two decades when sufficient computing capacity became available. Their significance for the scientific community was honored by the Nobel Prize awarded to W.

Kohn and J. Pople in 1998. DFT proved to be a general and predictive tool for calculating various properties which can be derived from the electronic ground state, such as equilibrium crystal structures and lattice constants, elastic constants, ideal strengths, surface energies, phonon dispersions, etc. [Freeman & Wimmer 1995].

2.1.2 The VASP code

The *ab initio* DFT calculations were done using Vienna *ab-initio* Simulation Package (VASP) developed at the Institute of Materials Physics of the University of Vienna [Kresse & Hafner 93] [Kresse & Furthmüller 96] [Kresse & Furthmüller 96b]. The calculations were conducted using the projector augmented wave (PAW) method employed to describe the electron-ion interaction [Kresse & Joubert 99] [Blöchl 94]. The exchange and correlation terms were described by the generalized-gradient approximation proposed by Perdew and Wang [Pedrew & Wang 92]. The integration in the Brillouin zone has been done on special k points (e.g. 8×8×8 Monkhorst-Pack grid) determined according to the Monkhorst-Pack scheme [Monkhorst & Pack 76] with energy cutoff of 600 eV, and tetrahedron method with Blöchl corrections for the energy calculation and the calculations of electronic properties, e.g. density of state (DOS) and valence charge density. The Gaussian smearing method with typical smearing width of 0.2 is used for the stress calculations. The conjugate gradient algorithm is used to relax the ions into their instantaneous ground state. We refer to the quoted publications [Kresse & Hafner 93] [Kresse & Furthmüller 96] [Kresse & Furthmüller 96b] and to the VASP-manual for further details.

The specific choice of the *ab initio* parameters for a given system, and cells including the information of their symmetries and positions of the atoms of the different systems used for the calculations will be described in the corresponding sections of Chapter 3.

2.2 Calculations of the total energies, lattice constants, bulk moduli, their derivatives, and of the interaction parameter

The total energies were taken from the calculated $E - V$ relationships at equilibrium volume V_0. The cohesive energies E_c were calculated from the total energy of compounds at equilibrium by subtracting the total energies of spin-polarized free atom. In order to study the relative stabilities of the ternary compounds with reference to the terminal phases, we define in Eq. (2.2.1) the formation energy of the ternary phase with reference to the terminal phases, i.e. the de-mixing energy $\Delta E_{demixing}$, as the difference between the total energy of the ternary phase $(TM)_{1-x}X_xN_y$, $E_{TM_{1-x}X_xN_y}$, (TM = transition metal, X = Si or Al) and of the reference states of the isostructural, terminal phases (TM)N, E_{TMN}, and XN, E_{XN}.

$$\Delta E_{demixing} = E_{TM_{1-x}X_xN} - (1-x)E_{(TM)N} - xE_{XN} \tag{2.2.1}$$

From the total energies obtained by *ab initio* DFT method, we calculated the formation energies of the ternary $(TM)_{1-x}X_xN_y$ phases for several compositions given typically by the fractions $x =$ 0.25, 0.5 and 0.75, in all phases relevant for the given system. The choice of reference state needed to meet the composition balance of a given reaction, e.g. Zr-Si-N → ZrN+Si_3N_4+Zr or Zr-Si-N+N_2 → ZrN+Si_3N_4, will be given in corresponding sections.

In order to verify the reliability of our calculations, we have in each case first calculated the total energy E as a function of the volume V, and fitted the calculated $E-V$ dependence by the Murnaghan's equation of state [Murnaghan 44] (Eq. (2.2.2)),

$$E_{Murn}(V) = -E_0 + \frac{B_0 V}{B_0^{'}}[\frac{(V_0/V)^{B_0^{'}}}{B_0^{'}-1} + 1] - \frac{B_0 V_0}{B_0^{'}-1} \tag{2.2.2}$$

to determine the equilibrium properties, such as bulk modulus B_0, its first derivative $B_0^{'}$, equilibrium volume V_0 and lattice constant a, and compared the results with experimental and theoretical data available in the literature. Zhang and Veprek have shown the using either the Birch's [Birch 47&78] or Vinet's equation of state [Vinet et al. 86] [Vinet et al. 87] yields the same results as the Murnaghan's EOS.

2.3 Calculations of the stress-strain curves and the determination of the enhanced valence charge density

The knowledge of the stress-strain relationship in both tension and shear is important for the understanding of the mechanical behavior of an ideal, defect-free material and for the estimate of the upper limit of its strength and hardness [Veprek et al. 07]. The ideal de-cohesion strength yields information about the inter-planar bond strength in the given crystallographic direction, whereas the ideal shear strength is a measure of the resistance of the material against plastic deformation. It correlates with the onset of dislocation formation, which commences by a series of subsequent shear events in an ideal crystal [Vliet et al. 03] [Li et al. 02]. The *ab initio* DFT calculations of stress-strain curves have been recently developed and applied to a number of different materials (e.g. [Y. Zhang et al. 05] [Roundy et al. 01] [Umeno et al. 07] [Pokluda et al. 04]).

The importance of the knowledge of the stress-strain curves is illustrated by the following example: Based on the first principle calculations of zero-pressure elastic moduli, which describe the elastic response of the crystal upon small strains near equilibrium, Cohen predicted about 20 years ago that C_3N_4 should be harder than c-BN and almost as hard as diamond [Cohen 85] [Liu & Cohen 90]. His report has inspired a large experimental effort of many researchers around the world to prepare this material. However, this effort remained without success because the maximum reported hardness of stoichiometric C_3N_4 was only 26-28 GPa [Veprek et al. 95b]. Y. Zhang et al. have recently calculated the stress-strain curves and the corresponding changes of the electronic structure upon strain. Their work explained that C_3N_4 can not be harder than c-BN, because it undergoes phase transformation into a soft graphite-like phase upon a relatively moderate, finite strain [Y. Zhang et al. 06; 06b].

Some researchers recently attempted to explain the hardness enhancement of B-N-C materials by the difference of the ideal strength of c-BN and several hypothetical B-N-C solution phases [Pan et al. 07] [Chen et al. 07]. However, one has to keep in mind that the hardness and strength of engineering materials is determined by structural defects (flaws), such as impurities, dislocations, microcracks, grain boundaries etc. [Haines et al. 01] [Brazhkin et al. 02] [Gilman 03], and it is usually orders of magnitude smaller than the ideal one [Hertzberg 89]. This has been illustrated by the strong reduction of maximum achievable hardness in the superhard nanocomposites by oxygen impurities [Veprek et al. 05b] mentioned in the introduction.

The *ab initio* DFT calculations of the stress-strain dependences have been done starting from the fully relaxed cell, by incrementally deforming the modeled cell in the direction of the applied strain, and simultaneously relaxing both the atomic basis vectors and the atoms inside the unit cell, at each step. To ensure that the strain path is continuous, the starting position at each strain step is taken from the relaxed coordinates of previous strain step. This approach with a relaxed loading path has been successfully applied to the calculation of the strength of several strong solids [Y. Zhang et al. 05] [Roundy et al. 01].

The valence charge density (VCD) is obtained directly from the *ab initio* DFT calculation by solving the Schrödinger equation [Martin 04]. VCD and bond lengths provide information about the relative stabilities of different bulk phases as well as of interfaces. This is particularly interesting for the interfaces because one can directly see the strengthening or softening of the bonds therein. As already mentioned in the introduction, Hao et al. [Hao et al. 06] [Hao et al. 06b;c] and Zhang et al. [Zhang et al. 07d] [Veprek et al.

07] have shown that there is a large strengthening of the 1 ML thin SiN_x interfacial layer sandwiched between 6–8 ML thick slabs of TiN. Based on the valence charge density distribution, Zhang et al. have also shown that pseudomorphic fcc-SiN is instable as bulk material. However it has not been clarified if this material is metastable or inherently unstable. Therefore this question will be clarified in this work. A comparison of the valence charge densities of different polymorphs will be also used to study the relative stabilities of different phases, of the interfaces and their behavior under applied strain. The aim of the present work is to extend the study of the strengthening of the 1 ML interfacial SiN_x monolayer reported by Hao et al. and by Zhang et al. to other systems in order to obtain a deeper understanding of its mechanism, and if possible, to identify other interfacial materials which could provide an even stronger effect. Because these calculations are very much time consuming, we shall concentrate on the ZrAlN system only.

2.4 Description of the thermodynamic calculations

Based on the sub-lattice solution model [Hillert 98] [Saunders & Miodownik 98], a ternary compound $(A,B)_aC_c$ can be described as a continuous solid solution composed of two compounds A_aC_c and B_aC_c. Thus, in the ternary $(A,B)_aC_c$ phase, a and c give the numbers of different sites per formula unit. The ternary system can be treated as a quasi-binary substitutional phase. The simplest model for such a solution can be obtained by assuming random mixing of the atoms within each sub-lattice.[2] It is then convenient to define mole fractions for each sub-lattice. They are called site fractions and denoted y. The site fractions are used to define the frame of reference for the Gibbs energy of the ternary solution phase. The Gibbs energy of the ternary $(A,B)_aC_c$ phase with a structure ψ, is given by Eq. (2.2.3) [Hillert 98] [Saunders & Miodownik 98] [Zhang & Veprek 07] [Zhang & Veprek 07b].

$$\begin{aligned} G^{\psi}_{(A,B)_aC_c} &= y_A({}^0G^{\delta}_{A_aC_c} + G^{\delta\to\psi}_{A_aC_c}) + y_B({}^0G^{\gamma}_{B_aC_c} + G^{\gamma\to\psi}_{B_aC_c}) \\ &\quad + aRT(y_A \ln y_A + y_B \ln y_B) + a y_A y_B L^{\psi}_{A,B:C} \end{aligned} \tag{2.2.3}$$

Here, ${}^0G^{\delta}_{A_aC_c}$ and ${}^0G^{\gamma}_{B_aC_c}$ are the Gibbs free energy of end-member phases of $\delta - A_aC_c$ and $\gamma - B_aC_c$ in the most stable structures whose thermodynamical data are available from experiments. $G^{\delta\to\psi}_{A_aC_c}$ and $G^{\gamma\to\psi}_{B_aC_c}$ are the lattice instability of metastable or unstable phases of $\psi - A_aC_c$ and $\psi - B_aC_c$ with respect to the stable phases $\delta - A_aC_c$ and $\gamma - B_aC_c$,

---

[2] Note that this is the extreme case. When considering immiscible systems, clustering will decrease the value of the de-mixing energy because it represents the onset of the phase segregation by the mechanism of nucleation and growth [Zhang & Veprek 07].

respectively. Index a is the number of sites of the sub-lattice (A,B) per formula unit, and y_A and y_B are the site fraction of elements A and B in the sub-lattice (A,B), respectively. y_A and y_B are defined by $y_A = x_A/(x_A + x_B)$ and $y_B = x_B/(x_A + x_B)$, where x_A and x_B are the fractions of the elements. The first two terms in Eq. (2.2.3) are the contributions of the pure phases, the third one is the mixing entropy contribution, and $L^{\psi}_{A,B:C}$ in the last term is the interaction parameter between $\psi - A_aC_c$ and $\psi - B_aC_c$ in the $\psi - (A,B)_aC_c$ phase.

For the stable terminal phases, the temperature-dependence of the Gibbs free energy ${}^0G^{\delta}_{A_aC_c}$ and ${}^0G^{\gamma}_{B_aC_c}$ above 298 K is given by Eq. (2.2.4) [Hillert 98] [Saunders & Miodownik 98] [Zhang & Veprek 07] [Zhang & Veprek 07b].

$$G(T) = a + bT + cT\ln T + dT^2 + eT^{-1} + fT^3 \qquad (2.2.4)$$

The polynomial coefficients a to f in Eq. (2.2.4) can be obtained for equilibrium stable phases by numerical fitting to the experimental data.

The dependence of interaction parameter on composition and temperature can be expressed as Eq. (2.2.5) [Redlich & Kister 48] [Hillert 98] [Saunders & Miodownik 98] [Zhang & Veprek 07] [Zhang & Veprek 07b].

$$L^{\psi}_{A,B:C}(y_B,T) = \sum_{k=0}^{n}(1-2y_B)^k(A_{ij} + B_{ij}T + C_{ij}T\ln T + D_{ij}T^2 + E_{ij}T^{-1} + F_{ij}T^3) \qquad (2.2.5)$$

Here, n is the order of the Redlich-Kister series, and A_{ij} to F_{ij} are the model parameters. Similar to the previous studies [Zhang & Veprek 07] [Zhang & Veprek 07b] [Zhang & Veprek 08], two simplifications were assumed in present calculations: Due to the immiscibility of the stoichiometric (TM)N-XN systems (TM = transition metal, X = Si or Al), only two coefficients of A_{ij} and B_{ij} were applied in the temperature dependent part. The Gibbs free energy of the ternary $(TM)_{1-x}X_xN_y$ phases in their given structure, that will be specified for each particular system in the respective section, as a function of temperature, given by Eqs. (2.2.3) to (2.2.5), has been used to construct the Gibbs free energy diagram over the whole range of composition. Based on these diagrams, the phase stabilities and selections in the quasi-binary TMN and XN system will be discussed. In addition, recently reported exponential dependence of interaction parameter on temperature will be used for the Zr-Si-N, Al-Si-N and Zr-Al-O systems in order to show its importance. We refer to the corresponding sections for further details.

2.5 Combined *ab initio* DFT calculation with thermodynamic modeling

For the immiscible quasi-binary (TM)N-XN systems, the ternary $(TM)_{1-x}X_xN_y$ phases with a structure ψ can be regarded as a continuous solid solution composed of a given fraction of the stoichiometric $\psi-(TM)N$ and $\psi-XN$ phases with the same structure ψ. According to Eq. (2.2.3), the molar Gibbs free energy of $\psi-(TM)_{1-x}X_xN$ solution phase can be expressed by Eq. (2.2.6).

$$\begin{aligned} G^{\psi}_{((TM)_{1-x}X_x)N_y} &= (1-x)({}^0G^{\alpha}_{(TM)N} + G^{\alpha\to\psi}_{(TM)N}) + x({}^0G^{\beta}_{XN} + G^{\beta\to\psi}_{XN}) \\ &\quad + RT[(1-x)\ln(1-x) + x\ln x] + x(1-x)L^{\psi}_{((TM)_{1-x}X_x)N_y} \end{aligned} \qquad (2.2.6)$$

When ψ represents α structure it means that in the ternary phase α-$(TM)_{1-x}X_xN_y$ the TM-atoms of the α-(TM)N are substituted by atoms X.

The Gibbs free energies of the stable phases can be obtained directly from the published literature [Barin 93] [Chase et al. 85], whereas they are not available for the unstable phases (e.g. fcc-AlN, hcp-ZrN etc.). However, the Gibbs free energy of an unstable phase can be approximately calculated from the Gibbs free energy of the stable one plus the lattice instability of the unstable phase, which will be obtained from the *ab intio* DFT calculation. For simplicity, we regard the lattice instability as a temperature independent parameter (this simplification has been justified in [Zhang & Veprek 07] [Zhang & Veprek 07b] [Zhang & Veprek 08]). For example, the lattice instability of the unstable fcc-AlN with respect to the stable hcp-AlN, $G^{hcp\to fcc}_{AlN}$, of about 35.19 kJ/mol (per formula unit) has been calculated by the *ab initio* DFT method. In a similar way, the lattice instability of hcp-ZrN with respect to fcc-ZrN, $G^{fcc\to hcp}_{ZrN}$, of about 92.99 kJ/mol (per formula unit) has been obtained for ψ corresponding to the hcp structure. For the stable phases, the temperature dependence of the Gibbs free energies ${}^0G_{(TM)N}$ and ${}^0G_{XN}$, respectively, can be obtained from the data compiled in the literature [Barin 93] [Chase et al. 85] and fitted by Eq. (2.2.4) in order to obtain the resulting polynomial coefficients *a* to *f*. The Gibbs free energy at 0 K is then approximately estimated from linear extrapolation of Eq. (2.2.4).[3]

---

[3] Such approximation will not change the relative values of Gibbs free energy of different phases at 0 K.

2.6 Thermodynamic calculations including the temperature and composition dependence of the interaction parameter

The interaction parameters of the ternary phase $(TM)_{1-x}X_xN_y$ with a given structure ψ, $L^{\psi}_{TM,X:N}$, at 0 K is obtained by fitting Eq. (2.2.7), using the total energies of the isostructural terminal phases (TM)N, XN and $(TM)_{1-x}X_xN_y$ phases with ψ structure obtained from the *ab initio* calculation,

$$E^{\psi}_{(TM)_{1-x}X_xN_y} - (1-x)E^{\psi}_{(TM)N_y} - xE^{\psi}_{XN_y} = x(1-x)L^{\psi}_{TM,X:N} \qquad (2.2.7)$$

The composition dependence of the interaction parameter is approximated by a polynomial of the type $({}^0L^{\psi}_{TM,X:N} + {}^1L^{\psi}_{TM,X:N} \cdot x + {}^2L^{\psi}_{TM,X:N} \cdot x^2 + {}^3L^{\psi}_{TM,X:N} \cdot x^3)$, where ${}^0L^{\psi}_{TM,X:N}$, ${}^1L^{\psi}_{TM,X:N}$, ${}^2L^{\psi}_{TM,X:N}$ and ${}^3L^{\psi}_{TM,X:N}$ are the composition dependent parameters. By fitting the values of the de-mixing energies (with reference to isostructual terminal phases) as a function of the composition calculated by the *ab initio* DFT method, we obtained the composition dependence of the interaction parameter for the given ternary phase with the given structure ψ, $L^{\psi}_{TM,X:N}$ at 0 K. More details about the exact fitting procedure used for a given system will be given in the corresponding section.

In the majority of papers, one assumes a linear dependence of the interaction parameter on temperature, i.e. only the coefficients A_{ij} and B_{ij} in Eq. (2.2.5). This dependence can be obtained from the calculated value of interaction parameter at 0 K and at another, higher temperature. For a variety of hard materials, the interaction parameter of about 20–50 kJ/mol has been assumed at a temperature close to the melting point, in a fairly good agreement with the experimental miscibility gaps [Holleck 88] [Spencer & Holleck 90] [Stolten 91] [Spencer 94] [Anderbouhr et al. 99]. The specific choice of the value of the interaction parameter at high temperature for a given system will be described in the corresponding sections. It should be emphasized that, the high temperature interaction parameter is unavailable in both experiments and *ab initio* calculations. However a reasonable estimation can be done based on the facts that, with increasing temperature the interaction parameter will decrease. Thus, the choice of a lower value than that at 0K is a realistic first approximation. This is in agreement with the previous empirical estimation of high temperature interaction parameter for some nitride systems like Ti-Al-N. As will be shown, it is important to consider the temperature dependence of interaction parameter, which has been absolutely ignored in many studies (e.g. [Mayrhofer et al. 06b]). In order to obtain information about the sensitivity of the final results to such a fit, we used in the work on the ZrAlN system both of the above mentioned values for comparison (see Sect. 3.1.1.). It will be shown in that section, that the results are relatively insensitive to the exact choice of that value.

Chapter 3: Results:

3.1 Combined *ab initio* DFT calculation and thermodynamic modeling

3.1.1 Zr-Al-N system

There is limited knowledge of this system available in the literature. Recent experimental studies have shown that only the fcc(NaCl-type)-$Zr_{1-x}Al_xN$ solid solution exists for $0<x<0.43$, and the hardness increases from 21 GPa to 28 GPa when the Al content increase from $x = 0$ to 0.43 [Lamni et al. 05]. With further addition of Al content, hcp-AlN appears and the hardness of the coatings deceases.

3.1.1.1 Structural properties and phase stabilities by ab initio DFT calculation

For the Zr-Al-N system, the following phases and structures were used: The fcc (NaCl-type) structure (space group Fm-3m, No. 225), with atoms placed in (0, 0, 0) and (1/2, 1/2, 1/2) positions, has been allowed to relax in volume, i.e. in lattice constant *a*, keeping the relative position of atoms and the cell shape constant. The hcp (ZnS-type) structure (space group P63mc, No. 186) has two metal atoms placed in (1/3, 2/3, 0) and (2/3, 1/3, 1/2), and two nonmetal atoms placed in (1/3, 2/3, *u*) and (2/3, 1/3, *u*+0.5) positions. Here, *u* is the internal structural parameter, which determines the vertical position of the nonmetal atoms. We used the initial ideal value of $u = 0.375$ for further calculations, and performed a full relaxation of the lattice constant, internal structural parameter and the cell shape. Both fcc and hcp structures were studied using a super-cell setup containing four metal and four nonmetal atoms. For ternary $Zr_{1-x}Al_xN$ phases in fcc and hcp structure, Zr and Al atoms were randomly distributed over the whole metal sublattice. As mentioned in Chapter 2, the choice of the position of metal sublattice in substitution was found to have no significant effect on the results of the present calculations. The total energies and the lattice constants of metastable hcp-ZrN and fcc-AlN, stable fcc-ZrN and hcp-AlN, and the ternary fcc- and hcp-$Zr_{1-x}Al_xN$ (x=0.25, 0.5, 0.75) phases were calculated and optimized. The optimized values were used for the determination of the lattice stabilities of metastable hcp-ZrN and fcc-AlN phases with respect to the corresponding stable fcc-ZrN and hcp-AlN phases, as well as for the determination of the interaction parameters of the ternary fcc- and hcp- $Zr_{1-x}Al_xN$ solid solution phases.

Figure 3.1.1.1 shows the calculated relationships between the total energy, *E,* and average volume, *V*, per atom for binary ZrN, AlN compounds and ternary $Zr_{1-x}Al_xN$ (x=0.25, 0.5, 0.75) solution phases with fcc (dashed lines) and hcp (solid lines) structures. It can be seen that in agreement with the experimental results, the fcc structure is more stable than the hcp one for ZrN, whereas the hcp structure is more stable for AlN. With the Al content of 0.25, the ternary fcc-$Zr_{0.75}Al_{0.25}N$ phase is more stable than the hcp one, in agreement with the experimental results which showed that only $Zr_{0.80}Al_{0.20}N$ phase with fcc structure has been found [Spillmann et al. 01]. At an Al content of about 0.5, the minima of the total energy of hcp and fcc structures are nearly equal. This is consistent with the experimental results that both fcc-ZrN and hcp-AlN were found in $Zr_{1-x}Al_xN$ coatings with a high Al content of about $x \geq 0.43$ [Lamni et al. 05].

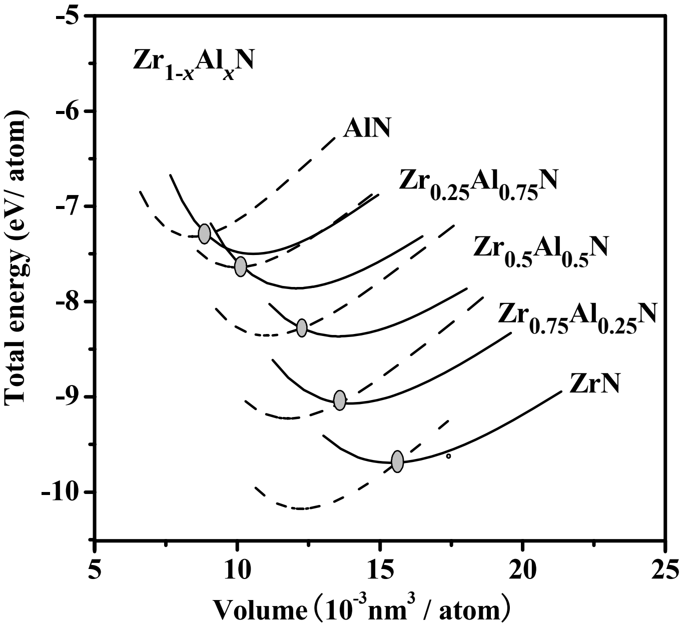

Fig. 3.1.1.1: The dependence of the total energy on average atomic volume for binary ZrN, AlN compounds, and ternary $Zr_{1-x}Al_xN$ (x = 0.25, 0.5, 0.75) phases in fcc (dashed lines) and hcp structures (solid lines).

The calculated values of the lattice constant a, axial ratio c/a, internal parameter u, bulk modulus B_0, its first pressure derivative B_0' and cohesive energy E_c of AlN, ZrN and $Zr_{1-x}Al_xN$ in fcc and hcp structure are listed in Table 3.1.1.I, together with the experimental and theoretical data reported in the literature [Stampfl & Walle 99] [Hirai et al. 00] [Spillmann et al. 01] [Nagao et al. 06] [Siegel et al. 06]. It can be seen that the calculated value of lattice constant a, of about 0.461nm for fcc-ZrN agrees with the experimental one, as does also the value of bulk modulus B_0 [Spillmann et al. 01] [Nagao et al. 06]. The calculated value of 0.4069 nm for fcc-AlN is between the experimental values of 0.411 nm [Hasegawa et al. 05] and 0.404 nm [Hirai et al. 00] and close to the theoretical value of

0.406 nm [Siegel et al. 06]. Also the calculated values of the lattice constant *a,* of the *c/a* ratio, of the internal parameter *u* and cohesive energy E_c, as well as of the bulk modulus B_0 and its pressure derivative B_o' obtained from the fit of the *E-V* curves by the Murnaghan equation of state (see chapter 2 and [Murnaghan 44]) for hcp-AlN, are all in good agreement with the published experimental and theoretical data [Stampfl & Walle 99]. The values of all the parameters calculated for the ternary $Zr_{1-x}Al_xN$ solid solution (x = 0.25, 0.5 and 0.75) in both structures are also reported in Table 3.1.1.I. To best of our knowledge, there are no related experimental data about these ternary solid solutions reported in the literature. The very good agreement of our calculated values for AlN and ZrN shows that our data calculated for the ternary $Zr_{1-x}Al_xN$ solid solutions are reliable.

Table 3.1.1.I: Calculated lattice constant a, axial ratio c/a, internal parameter u, bulk modulus B_0, its pressure derivative B_0' and the cohesive energy E_c of AlN, ZrN and $Zr_{1-x}Al_xN$ in fcc(NaCl) and hcp(ZnS) structure using *ab initio* DFT calculation, compared with the experimental and previous theoretical data (e – experimental data, t – theoretical data).

Phase	Structure	a (nm)	c/a	u	B_0 (GPa)	B_0'	E_c (eV)
ZrN	fcc(NaCl)	0.461 0.461±0.002 e[i]	---	---	256.56 257.9 t[ii]	4.632	8.72702
	hcp(ZnS)	0.3542	1.600	0.379	179.01	3.961	7.75744
AlN	fcc(NaCl)	0.4069 0.411 e[ii] 0.404 e[iii] 0.406 t[iv]	---	---	241.47	4.116	11.193
	hcp(ZnS)	0.3117 0.3111 e[ix] 0.3113 t[ix]	1.609 1.60 e[ix] 1.619 t[ix]	0.381 0.385 e[ix] 0.380 t[ix]	189.28 185-212 e[ix] 192 t[ix]	3.925 5.7-6.3 e[ix] 3.96 t[ix]	11.557 11.669 e[ix] 11.403 t[ix]
$Zr_{0.75}Al_{0.25}N$	fcc(NaCl)	0.4550	---	---	228.55	4.580	5.283
	hcp(ZnS)	0.3439	1.585	0.412	187.03	4.278	8.017
$Zr_{0.5}Al_{0.5}N$	fcc(NaCl)	0.4455	---	---	212.26	4.250	7.468
	hcp(ZnS)	0.3364	1.645	0.410	176.09	4.264	7.485
$Zr_{0.25}Al_{0.75}N$	fcc(NaCl)	0.4305	---	----	213.93	4.300	8.390
	hcp(ZnS)	0.3243	1.632	0.405	177.98	4.180	8.828

[i] = [Spillmann et al. 01]; [ii] = [Nagao et al. 06]; [iii] = [Hirai et al. 00]; [iv] = [Siegel et al. 06]; [ix] = [Stampfl & Walle 99]

Figure 3.1.1.2 shows the lattice constant *a* of $Zr_{1-x}Al_xN$ phases with fcc and hcp structures as a function of the Al fraction *x*, calculated with full relaxation, i.e. for the stress- and force-free state. It is found that with increasing *x* the lattice constants decrease approximately linearly following the relationships $a_{fcc} = 0.461 - 0.0541 \cdot x$ and $a_{hcp} = 0.3542 - 0.0425 \cdot x$ for fcc-$Zr_{1-x}Al_xN$ and hcp- $Zr_{1-x}Al_xN$, respectively. Accordingly, the lattice constants for fcc- $Zr_{0.80}Al_{0.20}N$, $Zr_{0.65}Al_{0.35}N$ and $Zr_{0.57}Al_{0.43}N$ phases are about 0.450 nm, 0.442 nm and 0.438 nm, respectively, close to the experimental data of 0.453 nm [Spillmann et al. 01], of 0.448 nm [Sanjinés et al. 06] and 0.445 nm [Sanjinés et al. 06].

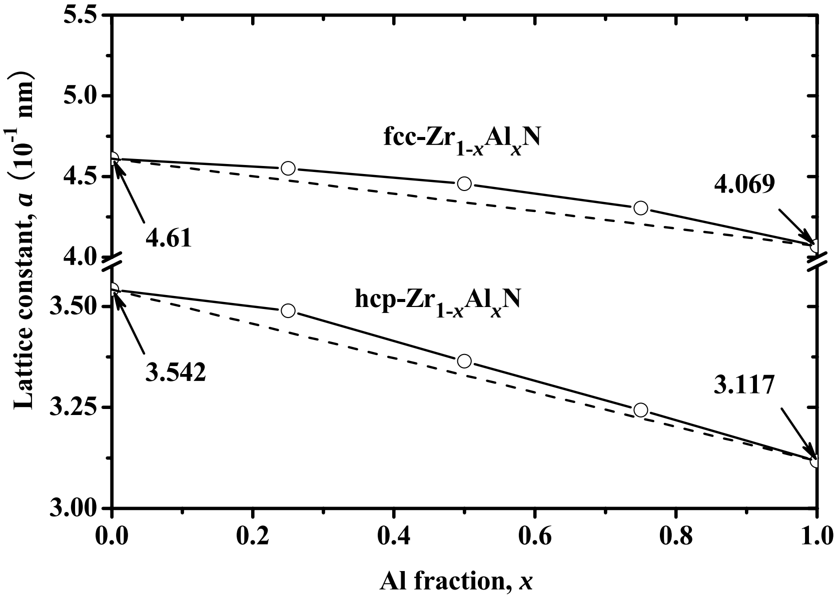

Fig. 3.1.1.2: The calculated lattice constant *a* as a function of the composition *x* in the ternary $Zr_{1-x}Al_xN$ phases with fcc and hcp structures, respectively.

The phase stability of the ternary phase $Zr_{0.5}Al_{0.5}N$, expressed in terms of the de-mixing energy (see chapter 2, Eq. (2.2.1)), amounts to 92.63 kJ/mol and 90.97 kJ/mol for fcc and hcp structures, respectively. Both values are positive, which means that these ternary $Zr_{1-x}Al_xN$ phases are thermodynamically unstable. Thus, only when kinetic constraints hinder the system to reach the equilibrium state, as found e.g. by plasma induced physical and chemical vapor deposition at a relatively low temperature, the metastable ternary $Zr_{1-x}Al_xN$ phases in fcc or hcp structures may be obtained. Upon annealing to a sufficiently high temperature for a sufficiently long period, both of them should decompose to the equilibrium mechanical mixture of fcc-ZrN and hcp-AlN.

3.1.1.2 Combined DFT & Thermodynamic calculations

For the immiscible quasi-binary ZrN-AlN systems, the ternary $Zr_{1-x}Al_xN$ phases with a structure ψ can be regarded as a continuous solid solution composed of a given fraction of the stoichiometric $\psi - ZrN$ and $\psi - AlN$ phases with the same structure ψ. According to Eq. (2.2.3), the molar Gibbs free energy of $\psi - Zr_{1-x}Al_xN$ solution phase can be expressed by Eq. (3.1.1.1).

$$\begin{aligned} G^{\psi}_{(Zr,Al)N} &= (1-x)({}^0G^{fcc}_{ZrN} + G^{fcc\to\psi}_{ZrN}) + x({}^0G^{hcp}_{AlN} + G^{hcp\to\psi}_{AlN}) \\ &\quad + RT[(1-x)\ln(1-x) + x\ln x] + x(1-x)L^{\psi}_{Zr,Al:N} \end{aligned} \tag{3.1.1.1}$$

When ψ represents fcc structure, it means that in the ternary phase $fcc - Zr_{1-x}Al_xN$, Zr atoms of the fcc-ZrN are substituted by Al. The Gibbs free energy of the fcc-ZrN can be obtained directly from the published literature [Barin 93], whereas it is not available for fcc-AlN phase due to its instability with respect to hcp-AlN. However, the Gibbs free energy of the fcc-AlN can be approximately expressed by the Gibbs free energy of the stable hcp-AlN plus the lattice instability of fcc-AlN, which can be obtained from the *ab intio* DFT calculation. For simplicity, we regard the lattice instability as a temperature independent parameter (this simplification has been justified in [Zhang & Veprek 07] [Zhang & Veprek 07b] [Zhang & Veprek 08]). Accordingly, the lattice instability of fcc-AlN with respect to hcp-AlN, $G^{hcp\to fcc}_{AlN}$, of about 35.19 kJ/mol has been calculated by the *ab initio* DFT method. In a similar way, the lattice instability of hcp-ZrN with respect to fcc-ZrN, $G^{fcc\to hcp}_{ZrN}$, of about 92.99 kJ/mol has been obtained for ψ corresponding to the hcp structure.

We shall now discuss the Gibbs free energy of the stable phases fcc-ZrN and hcp-AlN, i.e. ${}^0G^{fcc}_{ZrN}$ and ${}^0G^{hcp}_{AlN}$, respectively. The compiled data of temperature dependence of Gibbs free energy above 273 K by Barin [Barin 93] were numerically fitted by Eq. (2.2.4). The resulting polynomial coefficients a to f in Eq. (2.2.4) are listed in Table 3.1.1.II. The Gibbs free energy at 0 K is then approximately estimated from linear extrapolation of Eq. (4) (Note, that such approximation will not change the relative values of Gibbs free energy of different phases at 0 K).

Table 3.1.1.II: The fitted parameters in Eq. (2.2.4).

Phase	*a* (10^5)	*b* (10^2)	*c* (10)	*d* (10^{-3})	*e* (10^5)	*f* (10^{-7})
fcc-ZrN	-3.829	2.919	-4.843	-2.150	4.603	-1.522
hcp-AlN	-3.385	3.006	-4.600	-3.550	9.882	4.2144

As the third step we determine the interaction parameters $L^{fcc}_{Zr,Al:N}$ and $L^{hcp}_{Zr,Al:N}$ at 0 K by fitting Eq. (3.1.1.2), using the total energies of ZrN, AlN and $Zr_{1-x}Al_xN$ phases with ψ structure obtained from the *ab initio* calculation,

$$E^{\psi}_{Zr_{1-x}Al_xN} - (1-x)E^{\psi}_{ZrN} - xE^{\psi}_{AlN} = x(1-x)L^{\psi}_{Zr,Al:N} \qquad (3.1.1.2)$$

The composition dependence of the interaction parameter is approximated by $({}^0L^{\psi}_{Zr,Al:N} + {}^1L^{\psi}_{Zr,Al:N} \cdot x + {}^2L^{\psi}_{Zr,Al:N} \cdot x^2)$, where ${}^1L^{\psi}_{Zr,Al:N}$ and ${}^2L^{\psi}_{Zr,Al:N}$ are the composition dependent parameters. By fitting the *ab initio* data as shown in Fig. 3.1.1.3, we obtained the composition dependence $L^{fcc}_{Zr,Al:N} = (1.51 + 3.24 \cdot x) \cdot 10^5$ and $L^{hcp}_{Zr,Al:N} = (2.64 + 5.89 \cdot x - 7.77 \cdot x^2) \cdot 10^5$ J/mol for fcc- and hcp- $Zr_{1-x}Al_xN$, respectively.

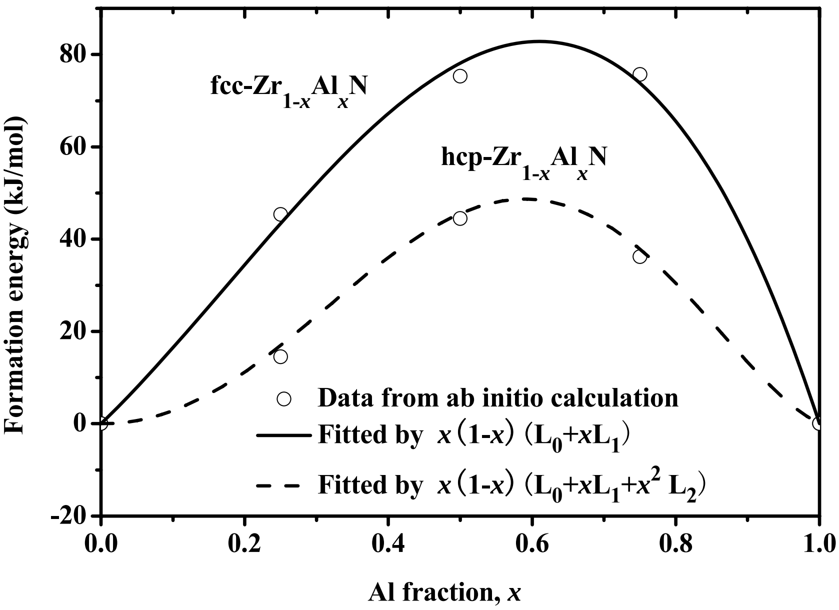

Fig. 3.1.1.3: Fit of the formation energies (lines) by *ab initio* DFT calculation (circles) to the function $x(1-x)(L_0 + xL_1)$ and $x(1-x)(L_0 + xL_1 + x^2L_2)$.

Now we assume a linear dependence of the interaction parameter on temperature, i.e. only the coefficients A_{ij} and B_{ij} are applied in Eq. (2.2.5). Accordingly, this dependence can be obtained from the calculated value of interaction parameter at 0 K and at another, higher temperature. As outlined above, for a variety of hard materials, the interaction parameter of about 20–50 kJ/mol has been estimated around the melting point, in a reasonable agreement with the experimental miscibility gaps [Holleck 88] [Spencer & Holleck 90] [Stolten 91] [Spencer 94] [Anderbouhr et al. 99]. In order to obtain information about the sensitivity of the final results to such a fit, we used in the present work both values 50 kJ/mol and of 20 kJ/mol as the maximum and minimum, respectively. The melting point of $Zr_{0.5}Al_{0.5}N$ solid solution of 3007.5 K used here is the average value of the melting points of ZrN and of AlN [Holleck 86]. Accordingly, the temperature dependent parameters of about -97 J/mol·K and -54 J/mol·K are calculated for fcc- and hcp- $Zr_{1-x}Al_xN$, respectively, when the minimum value of 20 kJ/mol is used, whereas the values of -87 J/mol·K and -44 J/mol·K are obtained when the maximum value of 50 kJ/mol is adopted. In the following, we shall use the temperature dependence parameters calculated with the maximum interaction parameter of 50 kJ/mol. The possible error should not exceed 10–15 %. Using these values and the calculated lattice stabilities of metastable hcp-ZrN and fcc-AlN phases, the Gibbs free energies of the mixed ternary $Zr_{1-x}Al_xN$ phase at different temperatures of 0 K, 273 K, 373 K, 573 K, 773 K, 1073 K, 1273 K and nitrogen pressure of 1 atm have been calculated from Eq. (2.2.6) over the entire composition range. Figure 3.1.1.4 shows the results for three selected temperatures of 0 K, 773 K and 1273 K. The solid lines represent the fcc and the dashed lines the hcp structures. One can clearly see that the fcc structure is more stable within the composition range of $0 \le x \le 0.472$, whereas the hcp structure becomes more stable at higher Al content for the temperature of 0 K. With the increasing temperature, the cross-over point moves to a higher Al content reaching a value of $x = 0.568$ at the temperature of 1273 K.

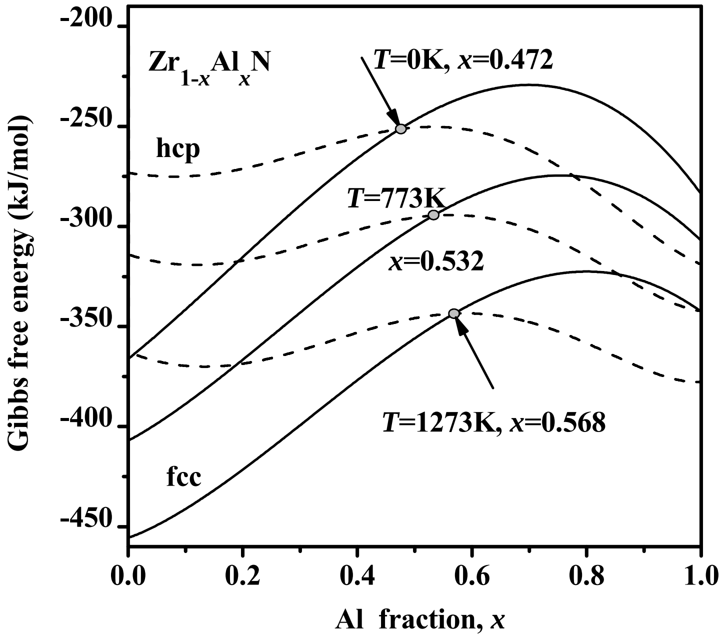

Fig. 3.1.1.4: Gibbs free energy of fcc- and hcp- $Zr_{1-x}Al_xN$ at three different temperatures of 0 K, 773 K and 1273 K. (Solid lines: fcc-structure; dashed lines: hcp-structure)

The cross-over point of the Gibbs free energy for the fcc to hcp phase transformation corresponds to the maximum "solubility" [4] of Al in the MeN. According to the experimental results of Sanjinés et al. [Sanjinés et al. 06], $Zr_{1-x}Al_xN$ coatings with $0 \le x \le 0.43$ deposited at 373 K crystallized in single-phase fcc solid solution, and at the critical point of $x = 0.43$, the maximum hardness has been obtained. Thus, the maximum "solubility" of Al in the $Zr_{1-x}Al_xN$

---

[4] The term "solubility" is not correctly used in the current papers because the $Zr_{1-x}Al_xN$ solid solutions are metastable whereas the "solubility" refers to an equilibrium state. We use it here as the other authors, however, with this limitation in mind.

coating should be $x = 0.43$. The theoretical calculations by Hugosson et al. [Hugosson et al. 03] have shown that the phase transition from fcc to hcp for $Zr_{1-x}Al_xN$ at 0 K occurs around $x = 0.5$. Thus both the experimental [Sanjinés et al. 06] and theoretical [Hugosson et al. 03] results are in a reasonable agreement with the present value for the cross-over point of $x = 0.472$ at 0 K. The relatively small increase of the critical Al fraction with the increasing temperature is similar to the results obtained for TiN-AlN system [Zhang & Veprek 07], but quite different from that for CrN-AlN one [Zhang & Veprek 07b]. In the latter system the cross-over point shifts strongly to lower Al-fraction with increasing temperature [Zhang & Veprek 07b], whereas in the TiN-AlN system the phase transformation from fcc to hcp is almost temperature independent [Zhang & Veprek 07].

3.1.1.3 Possibility of chemical and coherent spinodal decomposition

Decomposition of the $Zr_{1-x}Al_xN$ solution phase can occur either by nucleation and growth or by spinodal mechanism [Hillert et al. 61] [Ditchek & Schwartz 79] [Cahn & Hillard 58] [Cahn 61] [Cahn 63] [Cahn 68] [Cahn 91] [Porter & Easterling 01]. The spinodal mechanism occurs when the second derivative of the Gibbs free energy of the solution phase is negative ("chemical spinodal") and the interfacial misfit strain energy is sufficiently small compared to the de-mixing energy of the mixed phase ("coherent spinodal"). When the de-mixing energy is of the order of a few 10 kJ/mol, as in the case of the majority of metallic alloys and in the $Ti_{1-x}Al_xN$ system, the spinodal mechanism is possible only when the final, stable phases are coherent [Porter & Easterling 01].

Figure 3.1.1.5 shows the Gibbs free energy of the formation of fcc- $Zr_{1-x}Al_xN$ solid solution as a function of composition for temperatures 0 K, 273 K, 573 K, 773 K, 1073 K, 1273 K and nitrogen pressure of 1 atm, with stoichiometric fcc-ZrN and fcc-AlN as the reference states. It can be seen that, for the typical deposition temperature of ≤ 773 K and aging temperature of < 1073 K, the dependence of the Gibbs free energy of the immiscible system is typical of chemical spinodal, i.e. $\frac{\delta^2 G_f^0(x)}{\delta x^2} < 0$, within a large composition range. With increasing temperature, the Gibbs free energy of de-mixing decreases.

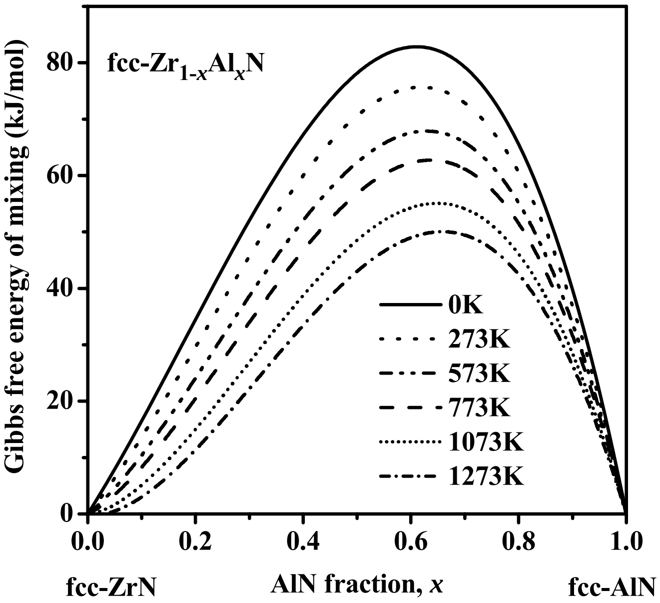

Fig. 3.1.1.5: Gibbs free energy of mixing of fcc-$Zr_{1-x}Al_xN$ phase ΔG as a function of composition for temperatures 0 K, 273 K, 573 K, 773 K, 1073 K, 1273 K, where ΔG > 0, with fcc-ZrN and fcc-AlN as reference states.

Figure 3.1.1.6 shows the calculated temperature-composition phase diagram for fcc-$Zr_{1-x}Al_xN$ showing the binodal (dashed line) and spinodal (short dashed line) curves with fcc-ZrN and fcc-AlN as reference states. In order to elucidate the possible effect of the choice of the critical interaction parameters, i.e., its temperature dependence (see above), we show in Fig 3.1.1.6 (a) and Fig. 3.1.1.6 (b) the binodal and spinodal curves with the critical interaction parameter of the maximum and minimum value of 50 kJ/mol and 20 kJ/mol, respectively. The binodal line corresponds to the co-existence of two stable phases, whereas below the binodal, phase segregation will occur either by (chemical) spinodal mechanism within the region below the (chemical) spinodal curve, or by nucleation and growth within the region between the spinodal and binodal curves. Thus, the solid solution is unstable within the spinodal and metastable between the spinodal and binodal curves. From Fig. 3.1.1.6 (a) and Fig. 3.1.1.6 (b) it can be seen that for temperatures of < 1000 K, which occurs during the deposition and application of the coatings for machining under mild conditions (relatively low cutting speed and sufficient cooling), the binodal curve is close to the y-axes, i.e. the ZrN and AlN nitrides are immiscible. The composition range for the chemical spinodal is from 0.289 to 0.994 in Fig. 3.1.1.6 (a) and from 0.299 to 0.994 in Fig. 3.1.1.6 (b), which illustrates the relatively small sensitivity of this result to the exact choice of the value of the critical interaction parameter at melting point for this system.

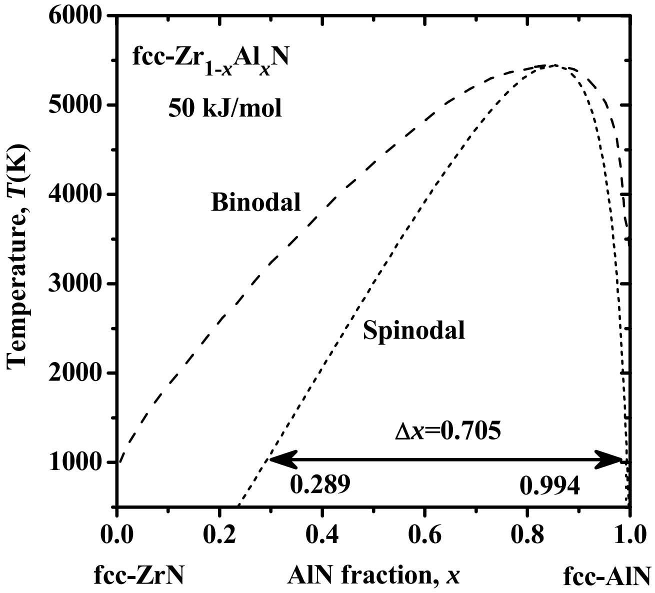

(a)

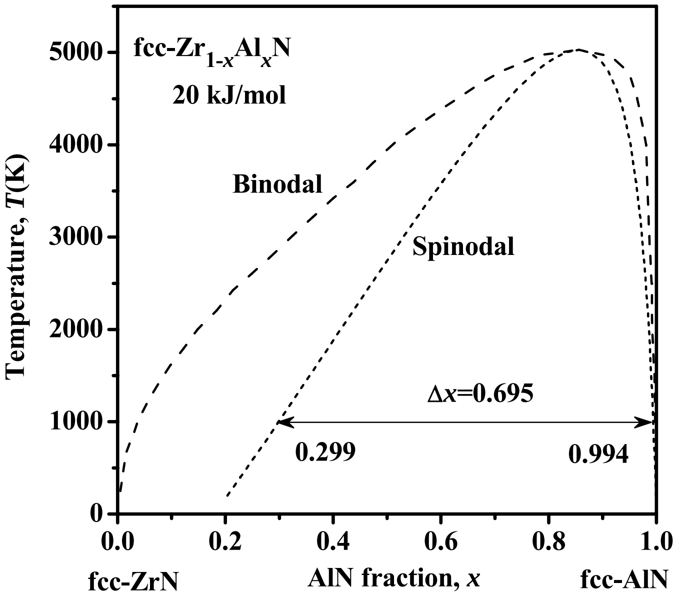

(b)

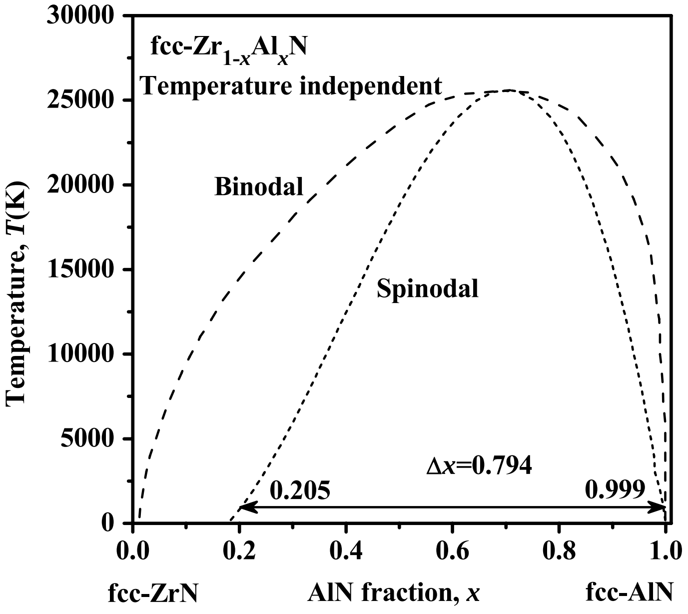

(c)

Fig. 3.1.1.6: Calculated temperature-composition phase diagram for fcc-$Zr_{1-x}Al_xN$ showing the binodal (dashed line) and spinodal (short dashed line) with fcc-ZrN and fcc-AlN as reference states. (a) with the maximum critical interaction parameter of 50 kJ/mol; (b) with the minimum critical interaction parameter of 20 kJ/mol; (c) with the constant critical interaction parameter obtained from *ab intio* DFT calculation at 0 K.

In order to illustrate the effect of the temperature dependence on the interaction parameter, we show in Fig. 3.1.1.6 (c) a diagram calculated with a constant interaction parameter as obtained from the *ab initio* DFT calculations at 0 K. It is clearly seen that the calculated top spinodal point approaches an unreasonably high temperature of about 25000 K. This is very important result because several recently published *ab initio* calculations used a constant value of the interaction parameter calculated at 0 K [Alling et al. 07] [Mayrhofer et al. 06b]. The results obtained in such a way have to be taken with care. A further improvement of the calculations may be obtained by considering also the effect of choice of different polynomial functions to fit the composition-dependent interaction parameter. We do not include it here because this effect is relatively small for the present case.

Of course, quantum dynamic (Car-Parrinello) calculations can in principle solve this problem because they allow one to perform the calculations at any chosen temperature. However, the CPU time needed in this case increases by several orders of magnitude.

Considering the fact that our *ab initio* DFT calculations at 0 K of the kind presented in this Thesis need several weeks on a modern work station with several parallel processors, the quantum dynamic approach is not realistic in this case. The fairly good similarity of the diagrams in Fig. 3.1.1.6 (a) and Fig. 3.1.1.6 (b), which were obtained by a combination of the "static" *ab initio* DFT at 0 K and relatively simple thermodynamics with a linear dependence of the interaction parameter on temperature, clearly shows the advantage of our combined computational approach.

Effect of the lattice mismatch

In this section, we consider the effect of the lattice mismatch and corresponding interfacial strain energy on the possibility of phase segregation according to the spinodal mechanism. In the theory of Cahn and Hillard et al. [Hillert et al. 61] [Ditchek & Schwartz 79] [Cahn & Hillard 58] [Cahn 61] [Cahn 63] [Cahn 68] [Cahn 91] [Porter & Easterling 01], the chemical spinodal discussed above should be modified by the contribution of elastic strain energy resulting from the composition fluctuation during the phase segregation. A simple thermodynamic estimate can be done by comparing the initial de-mixing energy with the final interfacial strain energy resulting from the mismatch between the demixed phases [Zhang & Veprek 07] [Zhang & Veprek 07b] [Zhang & Veprek 08] [Mayrhofer et al. 07]. When the interfacial strain energy is sufficiently small as compared with the chemical de-mixing energy, the decomposition by the spinodal mechanism is possible even for semi-coherent interfaces with a relatively large misfit [Zhang & Veprek 06] [Zhang & Veprek 08], because the misfit energy will be relaxed by the formation of misfit dislocations which are known to promote the spinodal phase segregation [Chen 02] [Léonard & Desai 98] [Hu & Chen 04]. Such diffusion-controlled phase segregation can be investigated by means of the phase-field model [Chen 02], which is, however, beyond the scope of the present work. Therefore we limit our discussion to a semi-quantitative estimate of the possible phase segregation and transformation path.

The misfit of the lattice constants between the fcc-ZrN and fcc-AlN of 12.47 % (see Table 3.1.1.I) is much larger as compared with that for the fcc-TiN/fcc-SiN and fcc-CrN/fcc-AlN interfaces of 0.117 % [Zhang & Veprek 08] and 0.75 % [Zhang & Veprek 07b], respectively. Therefore, the simple coherent model derived from the pseudomorphic growth of thin films, which yields the maximum possible elastic misfit strain energy [Zhang & Veprek 07b], cannot be used in the present case.

The continuum mechanical approach used recently by Mayhofer et al. for the decomposition of the Ti-Al-N systems [Mayrhofer et al. 07] does not consider the relaxation of the misfit strain energy by the formation of dislocations. Moreover, the assumption of the formation and growth of spherical TiN and AlN precipitates (see Eq. (2) and related discussion in Ref. [Mayrhofer et al. 07]) corresponds to the mechanism of nucleation and growth rather than to the spinodal one, which occurs by a growth of the amplitude of initially small compositional modulation with a characteristic period, as described by the theory of Cahn et al. [Cahn & Hillard 58] [Cahn 61] [Cahn 63] [Cahn 68] [Cahn 91] [Porter & Easterling 01]. Therefore, their approach is also not suitable for the present case. In the following we use a method of semi-quantitative estimate to analyze the possible phase segregation and transformation path.

The interfaces in alloys are classified as coherent when the misfit is lower than 5%, semicoherent when the misfit is larger than 5% but lower than 25%, and incoherent when the misfit is larger than 25% [Howe 97] [Porter & Easterling 01]. However, it is well known from the heteroepitaxial, pseudomorphic thin film growth that the relaxation of the elastic strain energy of a semicoherent interface by the formation of misfit dislocations depends on the thickness of the layer (see e.g., [Jain et al. 97] [Jain et al. 00] [Paul 04] and references therein), i.e. on the size of the precipitates in the case of alloys. Therefore, the high misfit of about 12.47 % for the fcc-ZrN/fcc-AlN interface must result in the formation of dislocations during the advanced stage of the phase segregation of the fcc-$Zr_{1-x}Al_xN$ solution, which is likely to facilitate the phase transition to hcp-AlN, because the misfit of fcc-ZrN(111)/hcp-AlN(0001) interface of 4.48 % is much smaller, and can be accommodated by the formation of misfit dislocations on the glissile fcc/hcp interfaces [Porter & Easterling 01]. The decomposition via a formation of coherent fcc-ZrN and fcc-AlN by spinodal mechanism, as experimentally reported [Mayrhofer et al. 03] and theoretically calculated [Zhang & Veprek 07] in the $Ti_{1-x}Al_xN$, is very unlikely in the $Zr_{1-x}Al_xN$ system. These ideas are also in accord with the consideration of the average volume per atom of 0.01056 nm^3 (10.56 $Å^3$) for the hcp-AlN, 0.00842 nm^3 (8.42 $Å^3$) for the fcc-AlN, 0.01105 nm^3 (11.05 $Å^3$) for fcc-$Zr_{0.5}Al_{0.5}N$ and 0.01224 nm^3 (12.24 $Å^3$) for fcc-ZrN. Obviously, the mismatch for both fcc-$Zr_{0.5}Al_{0.5}N$ and fcc-ZrN is smaller for hcp-AlN than for fcc-AlN. These consideration and conclusions are in agreement with the experimental results that no intermediate fcc-AlN has been observed in Zr-Al-N coatings so far [Sanjinés et al. 06]. The hardness enhancement during annealing of fcc-$Zr_{1-x}Al_xN$ has been attributed to the presence of the formation of the coherent strain regions, which are formed due to spinodal phase segregation towards Al-rich and Zr-rich zones, as suggested in Ref. [Sanjinés et al. 06]. However, in order to clarify the exact structure of the strained regions, and, particularly of the final stages of the phase segregation, further experimental work, in particularly annealing to higher temperatures until the structure and hardness of the films will reach a stable stage, is needed. In order to allow the system to remain stoichiometric, such annealing should be done under nitrogen.

3.1.1.4 Summary

The equilibrium properties, such as the lattice constant, bulk modulus, cohesive energy, and the relative stabilities of ZrN, AlN and ternary $Zr_{1-x}Al_xN$ phases in both the fcc(NaCl) and hcp(ZnS) structures have been studied by *ab initio* DFT calculations. The calculated values are in very good agreement with the published experimental and theoretical data thus assuring the reliability of present calculations.

Based on the calculated lattice stabilities of binary phases and interaction parameters of ternary solution phases, the phase selection in the $Zr_{1-x}Al_xN$ system has been studied over the entire composition range. The critical AlN concentration at which the phase transformation from fcc to hcp occurs is nearly independent of the temperature. This is in agreement with the phase transformation in $Ti_{1-x}Al_xN$ system [Zhang & Veprek 07], but different from the in $Cr_{1-x}Al_xN$ one [Zhang & Veprek 07b] where the critical Al concentration is temperature dependent.

The constructed chemically binodal and spinodal decomposition curves show that metastable fcc-$Zr_{1-x}Al_xN$ solution coatings might undergo phase decomposition into fcc-ZrN and fcc-AlN. However, considering the large value of interfacial strain, the fully coherent spinodal decompositon into the fcc-ZrN and fcc-AlN in large scale may be hindered, and decomposition into a mixture of fcc-ZrN and hcp-AlN is more preferable.

3.1.2 Zr-Si-N system

The Zr-Si-N system has been studied by several groups who used reactive sputtering. Unfortunately, the deposition conditions were, in most papers, chosen incorrectly and, therefore, did not enable the formation of fully segregated nanostructure. For example, Nose et al. [Nose et al. 02] used a low deposition temperature of ≤ 100°C. These researchers reported a hardness increase up to about 35 GPa with Si content increasing to about 3 at.%. The morphology changed from columnar to equi-axial at about 5 at.% Si. Films containing 12.8 at.% Si, which showed a hardness of 18 GPa, consisted of nanocrystal grains.. In a subsequent investigation [Zhou et al. 03], these authors reported that higher deposition temperature up to 400°C had only a little effect on the hardness. This may be due to impurities, which are however, not reported by these workers. Song et al. studied the microstructure and properties of the Zr-Si-N diffusion barrier films [Song et al. 04]. They have shown that with increasing substrate bias from -50 to -200 Volts, the Zr/Si ratio and the surface roughness increased, but the resistivity of the film decreased. With the decrease of the bias, the microstructure of Zr-Si-N film changed from composites consisting of ZrN nanocrystals in amorphous SiN_x to fully amorphous films. The reason for this change has not been clarified. In a series of studies, Sandu et al. also found hardness maximum of about 30 GPa for Si content of about 3 at.% in coatings deposited at a temperature of 240 and 440°C [Sandu 06a] [Sandu 06b] [Sandu et al. 07a] [Sandu et al. 07b] [Sandu et al. 08]. Coatings deposited at room temperature showed a maximum hardness of only 20 GPa for Si-content of about 6 at.%. In all these papers, the coatings had a pronounced columnar morphology instead of the fully isotropic one, as reported by Veprek et al. for fully segregated nanocomposites [Veprek et al. 95] [Veprek 99] [Veprek et al. 05] [Niederhofer et al. 99].

The relatively low hardness of about 30 to 35 GPa reported in all these papers is most probably due to oxygen impurities, which, however, have not been reported in majority of the papers. Only in the paper of Sandu, oxygen and carbon impurity content "below 2 at.% for each" (i.e., ≤ 4 at. % total) is mentioned [Sandu et al. 06a]. The hardness of such coating is determined by the strength of the oxygen-related defects within the SiN_x interface [Veprek et al. 05] [Veprek et al. 05b] [Hao et al. 06]. The papers of Sandu et al. and of the other quoted authors contain also a lot of speculations regarding the formation of the nanostructure which are not sufficiently supported by experimental data. For example, the columnar morphology with elongated ZrN nanocrystals is obviously responsible for the relatively low Si-content at which hardness maximum is found, because the specific interfacial area decreases with increasing average crystallite size.

ZrN/SiN_x nanomultilayers with different thickness of Si_3N_4 were investigated by Dong et al. [Dong et al. 06]. By analogy with the TiN/SiN_x heterostructures [Söderberg et al. 05] [Hu et al. 05], the maximum hardness of about 32 GPa has been achieved in the ZrN/SiN_x heterostrucutres for about 2 monolayers thin pseudomorphic fcc (NaCl)-SiN. When the SiN_x thickness was larger than about 1.1 nm, amorphous SiN_x has been formed and the hardness strongly decreased [Dong et al. 06].

The theoretical investigations of phase stabilities of the Zr-Si-N system are very limited. Therefore, in this chapter, we shall study its phase stabilities by means of the combined *ab initio* calculation and thermodynamic modeling as used in the foregoing section for the Zr-Al-N system, and in the recent papers of our research group [Zhang & Veprek 07] [Zhang & Veprek 07b] [Zhang & Veprek 08] [Sheng et al. 08].

In majority of the earlier studies, the temperature dependence of the interaction parameter has been expressed by the Redlich-Kister (RK) polynomial [Redlich & Kister 48] in linear approximation or even neglected by some authors, which may cause artefacts, such as too high spinodal temperature, apparent miscibility regions, and others. In order to avoid such problems, Kaptay recently recommended the use of the exponential temperature dependence [Kaptay 04]. This method has been successfully used for the thermodynamic modeling of Zn-Zr system [Arroyave & Liu 06]. Therefore we shall, in this chapter, compare the results obtained with the linear and exponential dependence of the interaction parameter on temperature.

Because of the importance of the pseudomorphically stabilized fcc-SiN, Zhang et al. studied the mechanical [Zhang et al. 07d] and thermodynamic [Zhang & Veprek 06] [Zhang & Veprek 07] [Zhang & Veprek 08] properties of the sub-stoichionmetric fcc-SiN. These studies have shown that this material is mechanically and thermodynamically unstable as compared to hcp-Si_3N_4. However, it was not clear from this work if fcc-SiN is metastable or inherently unstable. In a more recent work, Zhang et al. have shown that depending on their crystallographic nature, some of the 1ML fcc-SiN interfaces between TiN slabs are inherently unstable in their high-symmetry structure, but they stabilize by decreasing the symmetry [Zhang et al. 09]. Therefore, in this section we shall investigate the stability of bulk fcc-SiN by calculating the elastic constants and phonon dispersion relations.

3.1.2.1 Structural properties and phase stabilities by *ab initio* DFT calculation

In the study of the Zr-Si-N system, the following phase structures have been considered: the fcc(NaCl-type), space group Fm-3m, No. 225, and hcp (ß-type), space group $P6_3/m$, No. 176. The hcp(ß) and fcc(NaCl) structure were studied using a supercell of 14 and 16 atoms, respectively. For ternary $Zr_{1-x}Si_xN_y$ phases in fcc(NaCl) and hcp(ß)-Si_3N_4 structure (y is 1 in fcc(NaCl) and 4/3 in hcp(β) structure), Zr and Si atoms were randomly distributed over the whole metal sublattice. As mentioned in Chapter 2 and in section 3.1.1, the choice of the position of metal sublattice in substitution was found to have no significant effect on the results of the present calculations.

We calculated the total energies and the lattice constants of stable fcc-ZrN and hcp(ß)-Si_3N_4, metastable hcp-Zr_3N_4 and fcc-SiN, the ternary fcc-$Zr_{1-x}Si_xN$ (x=0.125, 0.25, 0.375, 0.5, 0.625, 0.75, 0.875) and hcp-$Zr_{1-x}Si_xN_y$ (x=0.167, 333, 0.5, 0.667, 0.833) phases. In the case of the high symmetry of the fcc-NaCl structure, the relaxations of the lattice constant (i.e., energy minimization) were performed without any optimization of the internal parameter. However, for the hcp(ß)-Si_3N_4 in $P6_3/m$ space group, the optimization of internal parameters is necessary in order to obtain the most stable structure. Therefore, the full geometry optimization for hcp(ß)-Si_3N_4 was performed with relaxations of both the lattice constant as well as all internal parameters. The optimum values were used for the determination of the lattice stabilities of metastable hcp(ß)-Zr_3N_4 and fcc-SiN with respect to the corresponding stable fcc-ZrN and hcp(ß)-Si_3N_4 phases, as well as for the determination of the interaction parameters of the ternary fcc- and hcp- $Zr_{1-x}Si_xN_y$ solid solutions.

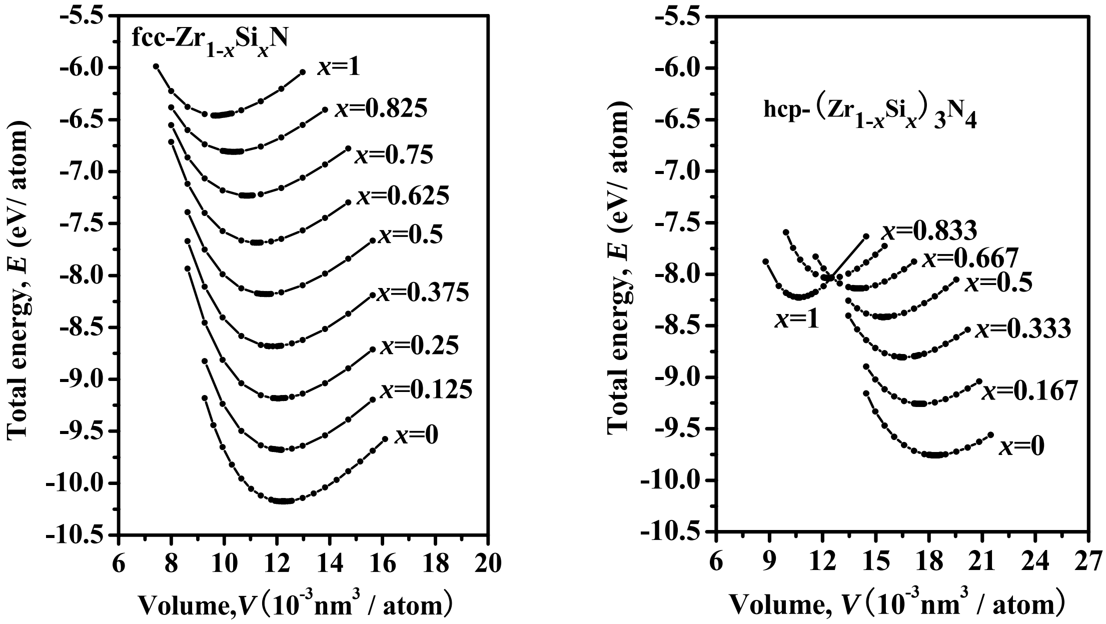

(a) (b)

Fig. 3.1.2.1: The dependence of the total energy on average atomic volume for binary ZrN_y, SiN_y compounds and the ternary $Zr_{1-x}Si_xN_y$ solid solutions in (a) fcc(NaCl) and (b) hcp(ß) structures.

Figure 3.1.2.1 (a) and (b) show the calculated dependence of the total energy, E, on volume, V, for binary ZrN, SiN, and ternary $Zr_{1-x}Si_xN$ with fcc (NaCl) structure, and for binary Zr_3N_4, Si_3N_4 and ternary $(Zr_{1-x}Si_x)_3N_4$ with hcp(ß) structures. It can be seen that, in agreement with the experimental results, the fcc-ZrN structure is more stable than hcp(ß) one, whereas the hcp(ß)-Si_3N_4 structure is more stable than the fcc- one. One can also notice that for hcp-$(Zr_{1-x}Si_x)_3N_4$ solution with Si fraction $x > 0.5$ in the (Zr, Si) sublattice, the local minima of the total energies for $x = 0.667$, 0.883 are higher than those of the stable binary hcp (ß)-Si_3N_4. To check for the possible reason, we have done the relaxation of these phases with Si content higher than 0.5. During the running of the program script, the output file reminded us that: "… sub-space-matrix is not hermitian in DAV …", which indicates that the ionic relaxation leads to unreasonable geometry. This is obviously due to the large difference of the atomic size of Zr and Si which introduces large strain resulting in an increase of the total energy.

In order to check the reliability of our calculations for the present system, the equilibrium volume V_0, lattice constant a, total energy E_0, bulk modulus B_0 and its first derivative (pressure dependence) B_0' were calculated for the three binary phases of fcc-ZrN, hcp(ß)-Si_3N_4 and fcc-SiN as well as for hcp-Zr and fcc-Si using the Murnaghan equation of state, Eq. (2.2.2), to fit the dependence of total energy on volume shown in Fig. 3.1.2.1. All the resulting values are summarized in Table 3.1.2.I. The corresponding cohesive energy E_c and the formation enthalpy ΔH_f (see Eq. (2.2.1)) are also included in Table 3.1.2.I together with experimental and theoretical data reported in the literature [Aguayo et al. 02] [Ziambaras & Schröder 03] [Nagao et al. 06] [Vogelgesang et al. 00] [Ching et al. 98]. The calculated bond length of N_2 molecule of about 0.1085 nm, is in good agreement with calculated (0.1085 to 0.111 nm) and the experimental (0.1098 nm) value reported by Stampfl et al. [Stampfl et al. 01]. The agreement of all the data in Table 3.1.2.I is very good.

Table 3.1.2.I: The equilibrium volume V_0, total energies E_0, bulk modulus B_0, and its pressure derivative B_0' for hcp-Zr, fcc(Diamond)-Si, fcc(NaCl)-ZrN, hcp(ß)-Si_3N_4 and fcc-SiN obtained from fitting the *E*-*V* data in Fig. 3.1.2.1 by the the Murnaghan's equations of state. The cohesive energy E_c and the formation enthalpy ΔH_f were also calculated and summarized in the table. The calculated results are compared with the published experimental (e) and theoretical (t) data. (Note: the formation enthalphy is obtained by calculating the difference of the total energies of the stable)

Phase		V_0 (nm^3/atom)	E_0 (eV/atom)	E_c (eV/atom)	B_0 (GPa)	B_0'	ΔH_f (kJ/mol·atom)
N_2	Present work		-8.313	5.144			
	Reference			5.28 t[i] 4.95 e[ii]			
hcp-Zr	Present work	0.023368	-8.458	6.404	96.69	5	
	Reference	0.0234 t[iii]			95 t[iii]		
fcc-Si	Present work	0.020457	-5.428	4.539	85.75	4.275	
	Reference	0.020.414 t[iv]			87.7 t[iv]		
fcc-ZrN	Present work	0.012238	-10.175	7.564	256.56	4.632	-172.7
	Reference				257.9 t[v]		
hcp (ß)-Si_3N_4	Present work	0.010629	-8.225	6.017	237.207	3.902	-129.5
	Reference				216 e[vi] 259 e[vi]	3.99 t[vii]	
fcc-SiN	Present work	0.00967	-6.457	4.432	177.41	3.411	39.17
	Reference				173.7-184.3 t[viii]		

[i] = [Zoroddu et al. 01]; [ii] = [Stampfl & Walle 99]; [iii] = [Aguayo et al. 02]; [iv] = [Ziambaras & Schröder 03]; [v] = [Nagao et al. 06]; [vi] = [Vogelgesang et al. 00]; [vii] = [Ching et al. 98]; [viii] = [Zhang et al. 07d].

Now we shall discuss the lattice instability of hypothetical fcc-SiN with respect to the hcp(ß)-Si_3N_4, $G_{SiN}^{hcp\rightarrow fcc}$. For simplicity, we regard the lattice instability as a temperature-independent parameter. Based on the reaction 4fcc-SiN = hcp(ß)-Si_3N_4 + Si, which corresponds to a low activity of nitrogen, a high lattice instability of fcc-SiN with respect to hcp-Si_3N_4 of 135.1 kJ/mol·atom has been obtained. Considering the reaction 3fcc-SiN + 0.5N_2 = hcp(ß)-Si_3N_4, which corresponds to high nitrogen pressure, an even higher lattice instability of 167 kJ/ mol·atom has been obtained in agreement with calculated results in [Zhang & Veprek 07a]. In a similar way, the lattice instability of hcp-Zr_3N_4 with respect to fcc-ZrN

$G_{ZrN}^{fcc\rightarrow hcp}$ of about 64.29 kJ/ mol·atom has been obtained based for reaction 4fcc-ZrN = hcp-Zr_3N_4 + Zr and of 14.96 kJ/ mol·atom, for reaction 3fcc-ZrN + $0.5N_2$ = hcp-Zr_3N_4. As expected, both fcc-SiN and hcp-Zr_3N_4 are unstable as compared to the stable hcp(ß)-Si_3N_4 and fcc-ZrN phases.

Figure 3.1.2.2 shows the calculated lattice constant *a* as a function of the Si fraction *x* in the ternary $Zr_{1-x}Si_xN_y$ phases with fcc and hcp structures, respectively. With increasing *x*, the lattice constant decreases, showing a slightly positive deviation from the Vegard's law $a_{fcc} = 4.61 - 0.35 \cdot x$ and $a_{hcp} = 9.23 - 1.55 \cdot x$ for fcc-$Zr_{1-x}Si_xN$ and hcp-$(Zr_{1-x}Si_x)_3N_4$, respectively. The decrease of the lattice constant is due to smaller radius of Si atoms of 0.118 nm as compared with that of Zr of 0.160 nm. The slight deviation from the Vegard's law is due to the change of the bonding character when the systems are changing from a stable fcc-ZrN (or instable hcp-Zr_3N_4) to instable fcc-SiN (or stable hcp(ß)-Si_3N_4).

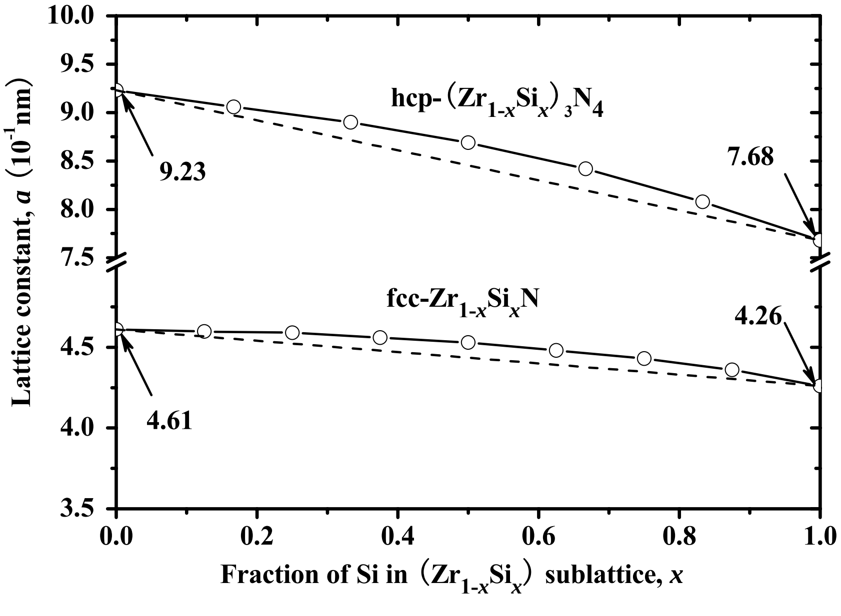

Fig. 3.1.2.2: The calculated lattice constant *a* as a function of the Si fraction *x* for the ternary fcc-$Zr_{1-x}Si_xN$ and hcp-$(Zr_{1-x}Si_x)_3N_4$, respectively.

3.1.2.2 Combined DFT & Thermodynamic calculations

For the immiscible quasi-binary ZrN$_y$-SiN$_y$ systems, the ternary Zr$_{1-x}$Si$_x$N$_y$ phase with a structure ψ can be regarded as a continuous solid solution composed of a given fraction of the stoichiometric $\psi - ZrN_y$ and $\psi - SiN_y$ phases with the same structure ψ. According to Eq. (2.2.3), the molar Gibbs free energy of $\psi - Zr_{1-x}Sil_xN_y$ solution phase can be expressed by Eq. (3.1.2.1).

$$\begin{aligned} G^{\psi}_{(Zr,Si)N} &= (1-x)({}^0G^{fcc}_{ZrN} + G^{fcc\to\psi}_{ZrN}) + x({}^0G^{hcp}_{Si_3N_4} + G^{hcp\to\psi}_{Si_3N_4}) \\ &\quad + RT[(1-x)\ln(1-x) + x\ln x] + x(1-x)L^{\psi}_{Zr,Si:N} \end{aligned} \qquad (3.1.2.1)$$

When ψ represents fcc structure, then in the ternary phase $fcc - Zr_{1-x}Si_xN$, Zr atoms of the fcc-ZrN are substituted by Si.

The Gibbs free energy of the stable phases fcc-ZrN and hcp(ß)-Si$_3$N$_4$, ${}^0G^{fcc}_{ZrN}$ and ${}^0G^{hcp(\beta)}_{Si_3N_4}$, can be obtained directly from the published literature [Barin 93]. The compiled data of temperature dependence of Gibbs free energy above 273 K by Barin were numerically fitted by Eq. (2.2.4). The resulting polynomial coefficients *a* to *f* in Eq. (2.2.4) for fcc-ZrN and hcp(ß)-Si$_3$N$_4$ are listed in Table 3.1.2.II. The Gibbs free energy at 0 K is then approximately estimated from linear extrapolation of Eq. (2.2.4). The Gibbs free energy of the fcc-SiN and hcp-Zr$_3$N$_4$ can not be directly obtained from available thermodynamic data but can be approximately expressed by the Gibbs free energy of the stable hcp(ß)-Si$_3$N$_4$ and fcc-ZrN plus the lattice instability of fcc-SiN and hcp-Zr$_3$N$_4$, which have been calculated in section 3.1.2.1.

Table 3.1.2.II: The fitted parameters in Eq. (2.2.4).

Parameter	*a*	*b*	*c*	*d*	*e*	*f*
Factor	(10^5)	(10^2)	(10)	(10^{-3})	(10^5)	(10^{-7})
fcc-ZrN	-3.829	2.919	-4.843	-2.150	4.603	-1.522
hcp(ß)-Si$_3$N$_4$	-7.735	4.143	-7.332	-57.00	3.265	49.37

Next we shall study the mixing properties of the fcc-$Zr_{1-x}Si_xN$ solid solution by considering the reaction $Zr_{1-x}Si_xN = (1-x)ZrN + \frac{x}{4}Si_3N_4 + \frac{x}{4}Si$, which should occur at low activity of nitrogen for the temperatures considered here. The de-mixing energy of fcc-$Zr_{0.5}Si_{0.5}N$ phase with respect to the stable fcc-ZrN, hcp(ß)-Si_3N_4 and pure Si is about 80.88 kJ/mol·atom. This value is higher than the previously calculated value of about 74.25 kJ/ mol·atom for the Ti-Si-N system [Zhang & Veprek 07a] [Zhang & Veprek 08]. For the case of a high nitrogen activity, where the reaction $Zr_{1-x}Si_xN + \frac{x}{6}N_2 = (1-x)ZrN + \frac{x}{3}Si_3N_4$ applies, the calculated de-mixing energy of fcc-$Zr_{0.5}Si_{0.5}N$ phase with respect to the stable fcc-ZrN, hcp(ß)-Si_3N_4 and pure N_2 of about 96.82 kJ/ mol·atom is also higher than that of 90.5 kJ/ mol·atom for the Ti-Si-N system [Zhang & Veprek 08]. These large values of de-mixing energy suggest that there is a large driving force for fcc-solution phase to segregate into the stable fcc-ZrN and hcp(ß)-Si_3N_4. The higher instability of the Zr-Si-N solid solution as compared with the Ti-Si-N one can be, in a somewhat simplified manner, understood in terms of a larger difference in the atomic size.

In order to determine the interaction parameters $L^{fcc}_{Zr,Si:N}$ and $L^{hcp(\beta)}_{Zr,Si:N}$ at 0 K, we calculated the mixing properties of the solid solution with respect to the isostructural terminal phases. As outlined in the introductory chapter, the interaction parameters for the phases with a structure Ψ are obtained from Eq. (3.1.2.2)

$$E^{\psi}_{Zr_{1-x}Si_xN_y} - (1-x)E^{\psi}_{ZrN} - xE^{\psi}_{SiN} = x(1-x)L^{\psi}_{Zr,Si:N} \qquad (3.1.2.2)$$

The composition dependence of the interaction parameter is approximated by the polynomial $({}^0L^{\psi}_{Zr,Si:N} + {}^1L^{\psi}_{Zr,Si:N} \cdot x + {}^2L^{\psi}_{Zr,Si:N} \cdot x^2)$, where ${}^0L^{\psi}_{Zr,Si:N}$, ${}^1L^{\psi}_{Zr,Si:N}$ and ${}^2L^{\psi}_{Zr,Si:N}$ are the composition dependent parameters. After fitting this dependence to the calculated data shown in Fig. 3.1.2.3, we obtained the composition dependence of the interaction parameters $L^{fcc}_{Zr,Si:N} = (2.26 + 2.45 \cdot x + 7.42 \cdot x^2) \cdot 10^4$ and $L^{hcp(\beta)}_{Zr,Si:N} = (1.63 + 0.41 \cdot x + 1.56 \cdot x^2) \cdot 10^5$ J/mol·atom for fcc- and hcp(ß)-$Zr_{1-x}Si_xN_y$ at 0 K, respectively. It is seen that the curves of both solution phases show positive mixing energies. Therefore, the solid solutions are unstable and should decompose to the isostructural terminal phases. This trend is clearly much more pronounced for the hcp-$(Zr_{1-x}Si_x)_3N_4$ than for the fcc-$Zr_{1-x}Si_xN$ one.

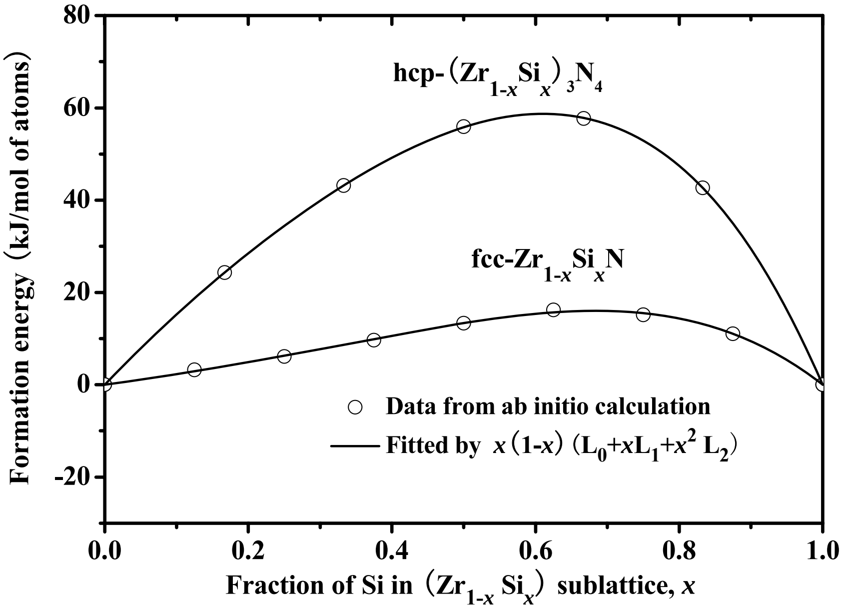

Fig. 3.1.2.3: Fit (lines) of the formation energies obtained by the *ab initio* DFT calculation (circles) to the function $x(1-x)(L_0+xL_1+x^2L_2)$ for fcc-$Zr_{1-x}Si_xN$ and hcp-$(Zr_{1-x}Si_x)_3N_4$.

We shall now compare the effect of the linear and exponential dependence of the interaction parameter on temperature. As mentioned earlier, the linear dependence has been used in majority of the studies so far. The linear dependence of the interaction parameter on temperature is obtained from the calculated value of interaction parameter at 0 K and at another higher temperature. For a variety of hard materials, the interaction parameter of about 20-50 kJ/mol has been estimated at their melting point, in a reasonable agreement with the experimental miscibility gaps (see [Zhang & Veprek 08] [Zhang et al. 08] and references therein). According to our results for the Zr-Al-N system presented above, there is relatively small effect of the choice between 20 and 50 kJ/mol on the final results in that system. Therefore, in the present work, we used the value of 20 kJ/mol·atom. To be sure, we have checked that using the value of 10 kJ/mol·atom has negligible effect on the results. The melting point of $Zr_{0.5}Si_{0.5}N$ solid solution of 2688 K used here is the average value of the melting point of fcc-ZrN and the decomposition temperature of hcp(ß)-Si_3N_4. Accordingly, the temperature dependent parameters of about -13.71 J/mol·K and -83.25 J/mol·K were calculated for fcc- and hcp- $Zr_{1-x}Si_xN_y$, respectively. Using these values and the calculated lattice instabilities of hypothetical hcp-Zr_3N_4 and fcc-SiN phases, the Gibbs free energy of the mixed ternary $Zr_{1-x}Si_xN_y$ phases at different temperatures has been calculated from Eq. (2.2.3) over the entire composition range. Fig. 3.1.2.4(a) shows the results at four typical temperatures of 373 K, 573 K, 773 K and 1073 K with stoichiometric fcc-ZrN and hcp(ß)-Si_3N_4 chosen as reference states. At the temperature of 373 K, the fcc structure is more stable within the composition range of $0 \leq x \leq 0.179$, whereas the hcp structure becomes more stable at higher Si content. With increasing temperature, the cross-over point moves to a lower Si content reaching a value of only $x = 0.123$ at the temperature of 1073 K.

The exponential dependence of interaction parameter on temperature given by Eq. (3.1.2.3) [Kaptay 04]

$$L_i = h_{oi} \cdot exp(-T/\tau_{oi}) \qquad (3.1.2.3)$$

will be now used to construct the phase diagrams for comparison. Here, the parameter L_i (J/mol) is the interaction parameter, h_{oi} (J/mol) is the enthalpy part of L_i at $T = 0\ K$, while parameter τ_{oi} is the temperature at which L_i would change its sign if it were extrapolated linearly from $T = 0\ K$. The interaction parameter depends on both the composition and temperature. From values of L_0 obtained from the fit of Fig.3.1.2.3, we first determine the value of h_{oi}. Using the value of 20 kJ/mol·atom for the interaction parameter at melting point we calculate the value of τ_{oi}. Accordingly, the temperature dependence is described by the equations $L = (2.2629 \cdot 10^4) \cdot e^{\frac{-T}{2482}}$ and $L = (1.6345 \cdot 10^5) \cdot e^{\frac{-T}{1011}}$ (J/mol·K) for fcc- and hcp- $Zr_{1-x}Si_xN_y$, respectively. Using these values and the calculated lattice instabilities of hypothetical hcp-Zr_3N_4 and fcc-SiN phases, the Gibbs free energy of the mixed ternary $Zr_{1-x}Si_xN_y$ phases at different temperatures has been calculated from Eq. (2.2.3) over the entire compositions. The results are shown in Fig. 3.1.2.4(b). The cross-over value of x at 373 K is about 0.149, and it decreases to 0.104 at 1073 K, i.e., somewhat lower than for the linear T-dependence.

Table 3.1.2.III summarizes the cross-over points of the fcc- and hcp-curves at the tempereature of 373 K, 573 K, 773 K and 1073 K calculated with the linear and exponential functions. Obviously, both T-dependence yield comparable cross-over points within about ≤ 20 %, and the corresponding values of x decrease with increasing temperature. This is in agreement with the experimental results of Sandu et al. [Sandu et al. 07a] [Sandu et al. 06a], who reported that with increasing substrate temperature the "solubility" limit of Si in ZrN lattice decreases. The cross-over points calculated with exponentially dependent interaction parameter are closer to the solubility limit of Si in ZrN lattice (10-12%) reported from the experiments [Sandu et al. 07a] [Nose et al. 02]. However, open questions remain regarding the effect of impurities (up to 2 at.% of O and C, each) and of possible nitrogen

substoichiometry in these experiments, because the solubility of Si in pure, stoichiometric ZrN is essentially zero [Rogl & Schuster 92].

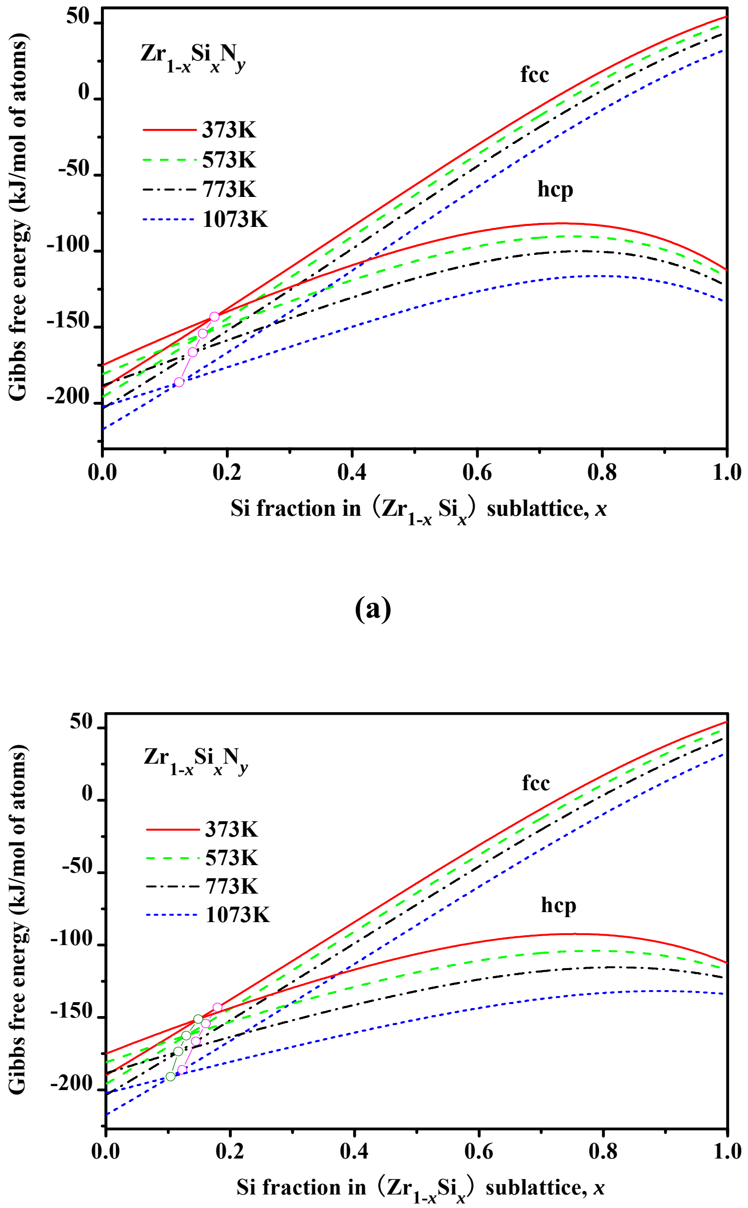

(a)

(b)

Fig. 3.1.2.4: Gibbs free energy of fcc- and hcp- $Zr_{1-x}Si_xN_y$ at temperatures of 373 K, 573 K, 773 K, 1073 K with stoichiometric fcc-ZrN and hcp(ß)-Si_3N_4 chosen as reference states for linear (Fig. (a)) and exponential (Fig. (b)) dependence of the interaction parameter on temperature. In Fig. (b), the red symbols are the cross-over points of the fcc- and hcp- curves corresponding to the exponential dependence whereas blue symbols correspond to the linear dependence from Fig. (a).

Table 3.1.2.III: The cross-over values of the fcc- and hcp- $Zr_{1-x}Si_xN_y$ curves under the tempereature of 373 K, 573 K, 773 K and 1073 K calculated by linear function, exponential function, respectively.

Temperature(K)	Cross-over point, x	
	Linear function	Exponential function
373	0.179	0.149
573	0.161	0.129
773	0.144	0.117
1073	0.123	0.104

The cross-over points correspond approximately to the "optimum" Si content of 7 – 9 at. %, where the maximum hardness has been found in a number of superhard ($H \geq 50$ GPa) nc-Me_nN/a-Si_3N_4 nanocomposites which were deposited under the conditions that enable the formation of fully segregated stoichiometric phases [Veprek et al. 05]. It has been shown in these papers that under the conditions of a sufficiently high pressure of nitrogen and sufficiently high deposition temperature, the Si_3N_4 percolates as about 1 interfacial monolayer because, due to the lattice mismatch, a thicker layer is unstable [Veprek & Veprek-Heijman 08].

Figure 3.1.2.5 shows the Gibbs free energy of mixing for the fcc-$Zr_{1-x}Si_xN$ solid solution as a function of composition for temperatures 373 K, 573 K, 773 K, 1073 K and nitrogen pressure of 1 atm, with isostructural, stoichiometric fcc-ZrN and fcc-SiN as the reference states, calculated with linear (Fig. (a)) and exponential (Fig. (b)) T-dependence, respectively. For the typical deposition temperature of ≤ 773 K and annealing temperature of < 1073 K, the dependence of the Gibbs free energy of the immiscible system is typical of chemical spinodal, i.e., $\frac{\delta^2 G_f^0(x)}{\delta x^2} < 0$, within the Si-rich composition range, but it should decompose by nucleation and growth for Zr-rich range. The coordinates of the peaks of the curves at the temperatures of 373 K and 1073 K are marked in the figures. At low temperature of 373 K, the maximum Gibbs free energy calculated with linear and exponential function are nearly the same. With increasing temperature from 573 K to 1073 K, the maximum Gibbs free energy of mixing calculated with exponential function decreases more rapidly than that calculated with linear function. The immiscibility gap is somewhat larger for the exponential *T*-dependence, particularly in the range of low Si content.

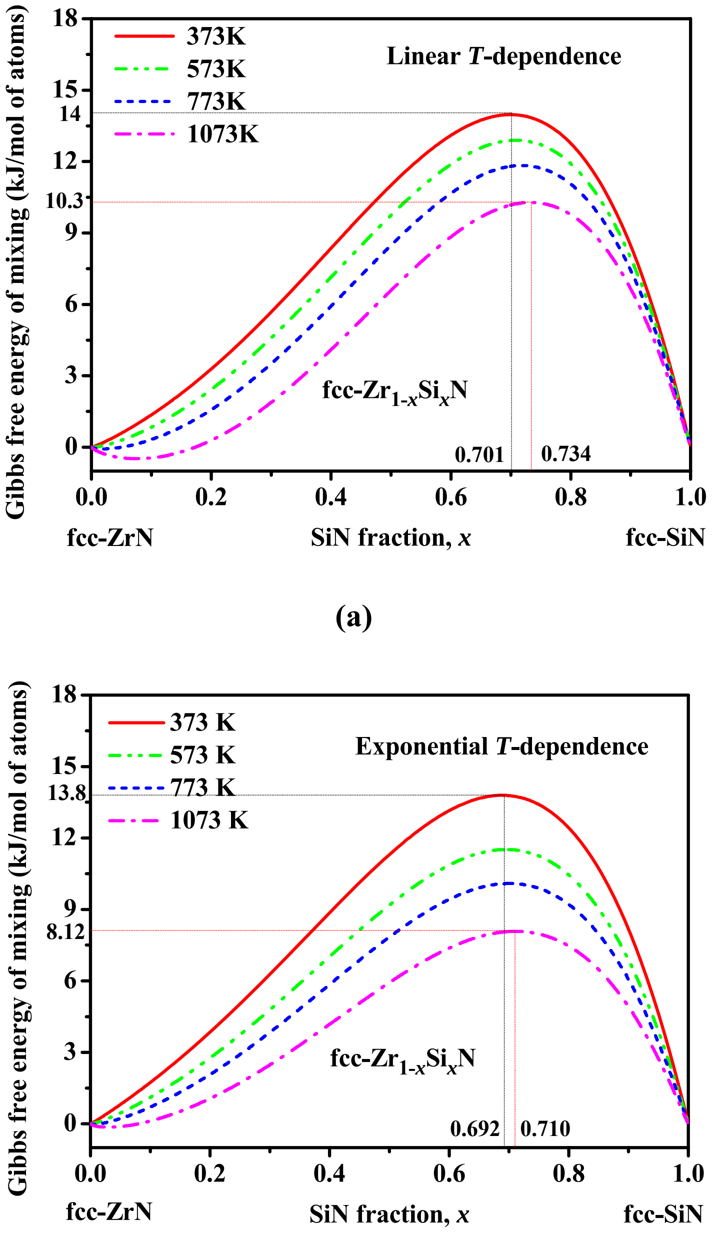

(a)

(b)

Fig. 3.1.2.5: Gibbs free energy of mixing of fcc-$Zr_{1-x}Si_xN$ phase, ΔG, as a function of composition *x* for temperatures 373 K, 573 K, 773 K, 1073 K, with fcc-ZrN and fcc-SiN as reference states calculated with (a) linear and (b) exponential temperature dependence of interaction parameter.

3.1.2.3 Possibility of chemical and coherent spinodal decomposition

Figure 3.1.2.6 shows the phase stability diagrams of fcc-$Zr_{1-x}Si_xN$ as a function of the composition for (a) temperature independent, (b) linearly, and (c) exponentially *T*-dependent interaction parameter. In the case of temperature dependent interaction parameter in Fig 3.1.2.6 (b) and (c), we used the value of 20 kJ/mol at the decomposition temperature.

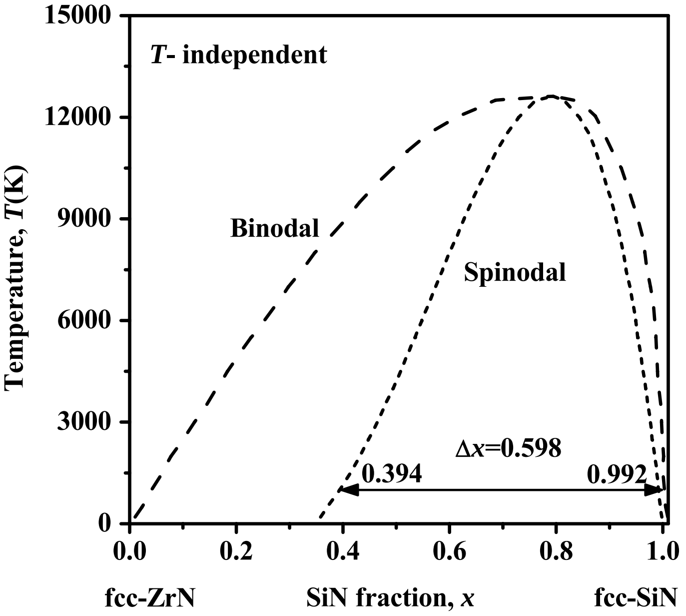

(a)

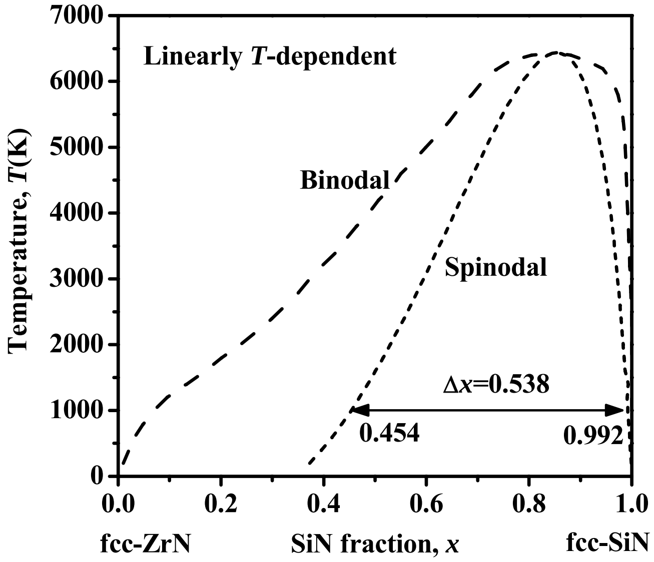

(b)

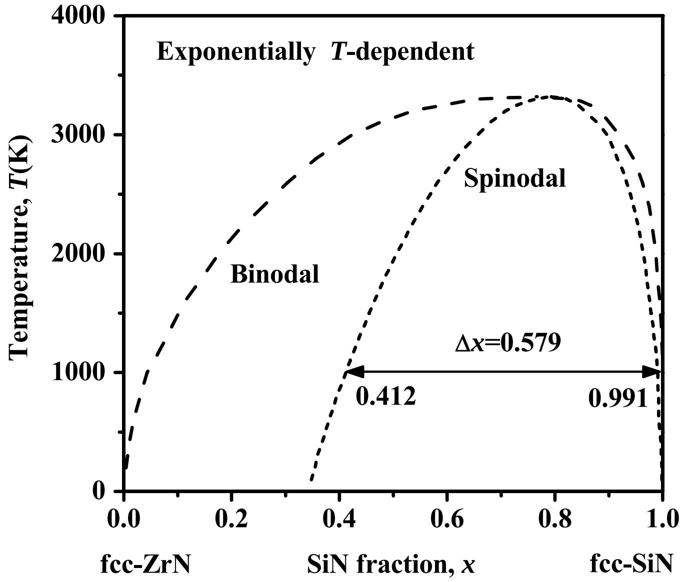

(c)

Fig. 3.1.2.6: Temperature-composition diagram for fcc-$Zr_{1-x}Si_xN$ showing the spinodal (short dashed line) and binodal (dashed lines) with fcc-ZrN and fcc-SiN chosen as reference states calculated with (a) temperature independent, (b) linearly and (c) exponentially temperature dependent interaction parameter.

It can be seen that, although the compositional range of the chemical spinodal is similar for all three cases, the maximum "spinodal temperature" is unreasonably high for the case of temperature independent interaction parameter shown in Fig.3.1.2.6 (a). This is in agreement with the results for Zr-Al-N system presented above. Therefore, neglecting the *T*-dependence of the interaction parameter, as found in many recent papers of other groups, yields unreliable results. Also the linear dependence yields a too high upper limit of the spinodal temperature of about 6300 K (Fig. (b)) whereas the exponential dependence (Fig. (c)) seems to be the best choice.

Compared with the Ti-Si-N system [Zhang & Veprek 08], the chemically spinodal occurs in the Zr-Si-N system at a much higher content of silicon of $x > 0.35$. Therefore, the formation of nc-ZrN/a-Si_3N_4 nanocomposites with 1 ML interfacial SiN_x by spinodal mechanism seems to be unlikely in this case. Phase segregation by nucleation and growth is more likely. In the Si-rich regime, spinodal phase segregation may occur because the thermodynamic driving force is high enough. Moreover, because the instability of the fcc(NaCl)-SiN with respect to the hcp(ß)-Si_3N_4 of 167 kJ/mol·atom is very high as compared with the de-mixing energy (see Fig. 3.1.2.3), such phase transformation during the later stage of the decomposition of the stoichiometric, Si-rich fcc(NaCl)-$Zr_{1-x}Si_xN$ solution will not hinder the decomposition of the solid solution into stoichiometric ZrN and Si_3N_4. Thus, the formation of nc-Si_3N_4/1ML-ZrN nanocomposites by spinodal mechanism should be thermodynamically possible, whereas that of nc-ZrN/a-Si_3N_4 is unlikely because of the dominance of the nucleation and growth. However, the formation of crystallins Si_3N_4 is kinetically hindered at temperatures below about 1000°C. It remains an open question if superhardness can be achieved in the nc-Si_3N_4/1ML-ZrN nanocomposite system, and, if another mechanism can be responsible for the hardness enhancement reported in Zr-Si-N polycrystalline films and heterostructures. One possible explanation may be the lowering of the energy of the ZrN grain boundaries by Si_3N_4 which should have a lower surface energy, high affinity to the surfaces of transition metal nitrides and also a larger structural flexibility to relax the interfacial energy of polycrystalline transition metal nitrides.

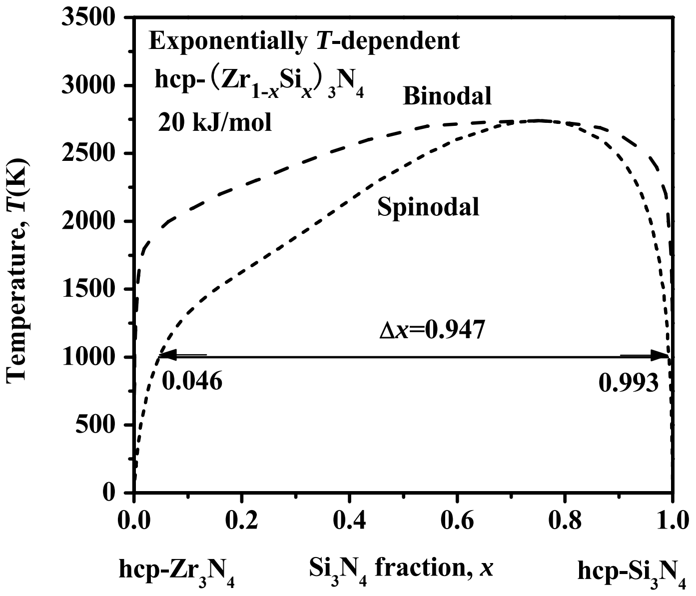

Fig. 3.1.2.7: Temperature-composition phase diagram for hcp-$(Zr_{1-x}Si_x)_3N_4$ showing the spinodal (short dashed line) and binodal (dashed lines) with hcp-Zr_3N_4 and hcp-Si_3N_4 chosen as reference states calculated with exponentially temperature dependent interaction parameter.

Figure 3.1.2.7 shows the phase stability diagrams of hcp(ß)-$(Zr_{1-x}Si_x)_3N_4$ as the function of Si fraction x with hcp(ß)-Zr_3N_4 and hcp(ß)-Si_3N_4 as reference states. On can see that, compared with Fig. 3.1.2.6 (c), both binodal and spinodal curves show different shapes, particularly for the region with smaller Si fraction, where the phase segregation by spinodal mechanism is possible for the hcp-$(Zr_{1-x}Si_x)_3N_4$ solid solution.

Effect of the lattice mismatch

In this section we discuss the effect of the lattice mismatch and the corresponding interface strain energy, and the possibility of phase segregation by the spinodal mechanism. According to the data presented above, the relatively large misfit between the fcc(NaCl)-ZrN and fcc(NaCl)-SiN phases of about 7.6 % suggests that semi-coherent interface should form in this case. In the case of heteroepitaxial, pseudomorphic thin film growth, the relaxation of the elastic strain energy by the formation of misfit dislocations depends also on the thickness of the film (see e.g., [Jain et al. 97] [Jain et al. 00] [Paul 04] and references therein), i.e. on the thickness of the interfacial layer in the case of the formation of the nanocomposites from a solid solution. Therefore, the large misfit of about 7.6 % for the fcc(NaCl)-ZrN/SiN interface can be accommodated only when the thickness of the interfacial phase is not much more than 1ML. In the case of the nc-TiN/a-Si_3N_4 nanocomposites, about 1 ML thick SiN_x interfacial layer correspond to maximum hardness and an Si concentration of about 7 - 9 at.%, i.e. the fraction x of about 0.14–0.18. However, as shown in Fig. 3.1.2.6, in the case of the fcc-$Zr_{1-x}Si_xN$ system, the decomposition of the solid solution with the formation of the stable fcc-ZrN should occur by nucleation and growth in this case. Only for the hypothetical hcp-$(Zr_{1-x}Si_x)_3N_4$ system with $x \cong 0.35–0.45$ spinodal mechanism may be possible. However, the terminal hcp-Zr_3N_4 phase is unstable. Therefore it is difficult to understand the results of Sandu et al. [Sandu et al. 08] that 1–2 ML SiN_x phase could be stabilized in their experiments. Here we are again facing the problem of up to 2 at.% of O and C impurities (each, i.e. about 4 at.% both together) and possibility of nitrogen substoichiometry in these experiments, because the "solubility" of Si, reported in their paper, is impossible in stoichiometric ZrN. Another problem which needs further experimental verification is the possibility of the formation of Si_3N_4/1 ML ZrN nanocomposites by spinodal mechanism which, according to the results presented in Figs. 3.1.2.6 and 3.1.2.7, should be thermodynamically possible. However, because Si_3N_4 crystallizes only at high temperatures of > 1000°C, the stoichiometric Si_3N_4 precipitates formed during the PVD at relatively low temperature should be amorphous, and the 1 ML thick ZrN interfacial layer should be charged positively, because the electronegativity of Zr (1.4) is smaller than that of Si (1.8).

For these reasons, the most likely mechanism of the formation of nc-ZrN/a-Si_3N_4 nanocomposites with 1 ML of SiN_x is the precipitation of fcc-ZrN nanocrystals and 1 ML of stoichiometric Si_3N_4-like interfacial layer by a "mixed" mechanism where the misfit is absent in the initial stage of the decomposition of the fcc-$Zr_{1-x}Si_xN$ solid solution, and the crystallite size of ZrN remains limited by the diffusion during the growth, as discussed in [Veprek et al. 09]. The only condition needed for such a process to occur is a sufficiently high nitrogen pressure that assures the formation of stoichiometric ZrN and Si_3N_4, which are immiscible [Rogl & Schuster 92].

3.1.2.4 The lattice stability and bonding nature of fcc-SiN

As discussed above, the substoichiometric fcc-SiN is thermodynamically unstable with respect to hcp(ß)-Si_3N_4, but it could be stabilized as pseudomorphic 1 to 2 ML thick layer sandwiched between several nm thick fcc-TiN and fcc-ZrN. In order to verify whether bulk fcc-SiN is a metastable or inherently unstable phase, we shall calculate, in this section, its elastic constant by means of the *ab initio* DFT calculations.

We apply a set of small distortions δ to different components ε of the strain tensor and calculate the corresponding change of the total energy ΔE. The elastic constants of interest are obtained from the following relations between the applied strain ε and the corresponding strain energy density changes $\Delta E/V_0$:

$$\varepsilon = (\delta,0,0,0,0,0) \text{ with } \Delta E / V_0 = \tfrac{1}{2} C_{11} \delta^2,$$

$$\varepsilon = (0,0,0,\delta,0,0) \text{ with } \Delta E / V_0 = \tfrac{1}{2} C_{44} \delta^2,$$

$$\varepsilon = (\delta,\delta,\delta,0,0,0) \text{ with } \Delta E / V_0 = \tfrac{3}{2} (C_{11} + 2C_{12}) \delta^2.$$

The elastic constants are related to acoustic phonons by well know relations which can be found in the literature (e.g. [Dove 93] p. 100). Negative values of elastic constants C_{44} and $(C_{11}-C_{12})/2$ suggest that the given structure is dynamically unstable against some transverse acoustic phonon modes. Here we limit our consideration only to C_{44} as the simplest, illustrative case, and because it shows the inherent instability of the fcc-SiN. When the elastic constant C_{44} is negative, the crystal is unstable against the transverse acoustic modes with frequencies ω related to this constant by $\rho\omega_{[001]}^2 = 2C_{44}\xi^2$ (ρ is the density and ξ is the corresponding wave vector) [Dove 93], because the phonon branches contain imaginary parts. Figure 3.1.2.8 shows the calculated relationships between ε and $\Delta E/V_0$ for the distortion $\varepsilon = (0,0,0,\delta,0,0)$. The local maximum at $\delta = 0$ means that $C_{44} < 0$, i.e., the system is inherently mechanically unstable [Born & Huang 54]. However, as seen from this figure, it may be stabilized by small distortion into the local minimum which lowers the symmetry of the system, in a way similar to that as found for the 1 ML pseudomorphic fcc-SiN interface [Zhang et al. 09]. The calculated values of the elastic constants $C_{11} = 202.461$ GPa and $C_{12} = 183.555$ GPa show that phonon branch with the wave vector along the [110] and polarization vector along $[1\bar{1}0]$ is stable because $C_{11} - C_{12} > 0$, i.e., the phonon frequencies are positive, i.e. the relationship $\rho\omega^2_{[110]} = 2(C_{11} - C_{22})\xi^2$ does not contain any imaginary solution.

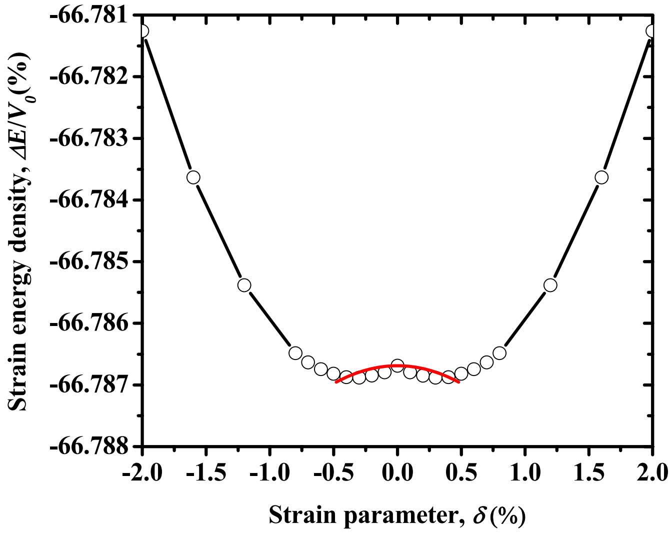

Fig. 3.1.2.8: Strain energy density variations vs. the distortion $\varepsilon = (0,0,0,\delta,0,0)$.

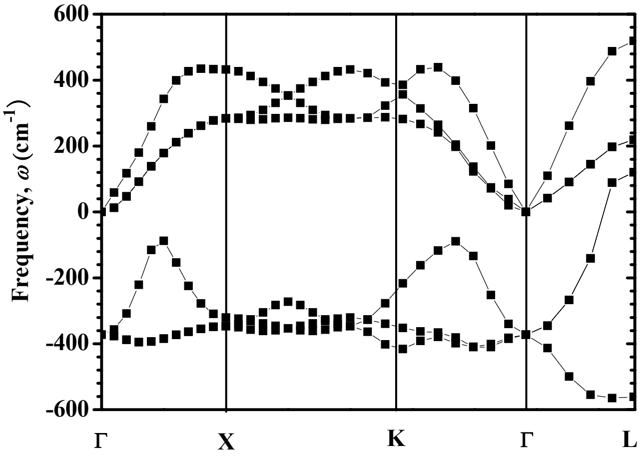

Fig. 3.1.2.9: Calculated phonon dispersion curves for bulk fcc-SiN for the $\varepsilon = (0,0,0,\delta,0,0)$ branch.

The phonon dispersion relationships were calculated using the density functional linear response method as complemented in Quantum-Espresso *ab initio* DFT code [link: http://www.quantum-espresso.org/]. Figure 3.1.2.9 shows the calculated phonon dispersion curves for bulk fcc-SiN. The presence of the negative phonon branches confirms that the bulk fcc-SiN in its fully symmetric structure is unstable. Similar results were recently reported also by Alling et al. [Alling et al. 08], thus confirming the reliability of our results.

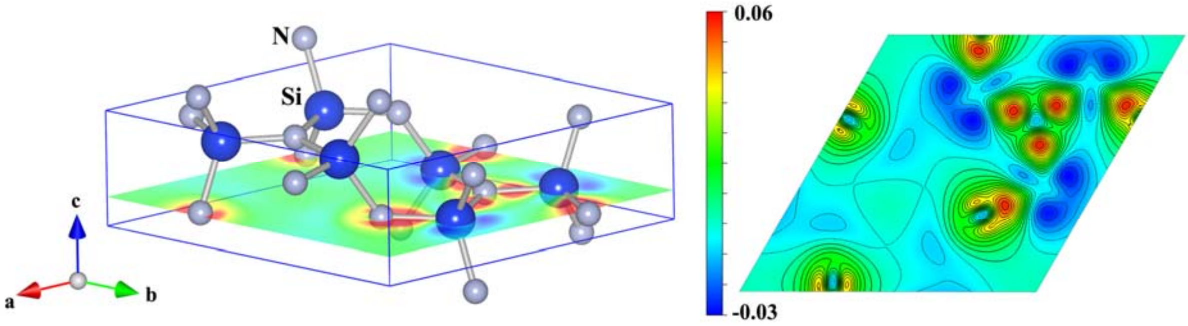

(a) hcp(ß)-Si$_3$N$_4$

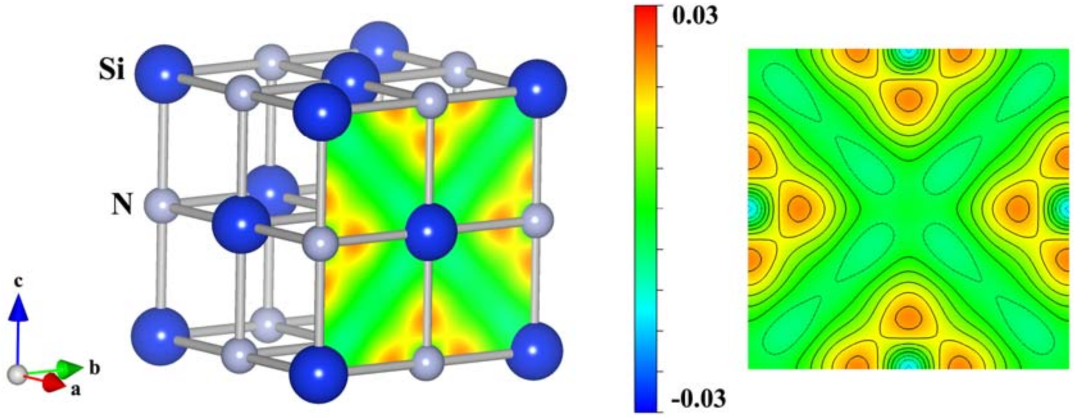

(b) fcc-SiN

Fig. 3.1.2.10: (color online) Left: Atomic structures and the Si-N containing planes for which the valence charge differences are shown on the right for the stable hcp(ß)-Si$_3$N$_4$ (Fig. (a)) and unstable fcc-SiN (Fig. (b)).

Now we shall try to explain the electronic origin of the instability of fcc-SiN. Figure 3.1.2.10 shows the atomic structure and relevant planes (left) for which the valence charge density difference (VCDD) are shown on the right. The VCDD are defined as the valence charge density of the system under consideration from which the valence charge densities of neutral atoms at the given lattice positions were subtracted. Figure 3.1.2.10 shows the VCDD along the Si-N bonds. One can see that total electron density in the polar, covalent bond of hcp(ß)-Si_3N_4 is much higher than those in fcc-SiN.

This is further illustrated by Fig. 3.1.2.11 which shows the VCDD between the Si and N atoms. The bond length in hcp-Si_3N_4 is much shorter and the total electron density in the polar, covalent bond is much higher than those in fcc-SiN. In our earlier paper we have shown, that fcc-SiN has a "metallic" character because of a finite density of states at the Fermi level [Zhang et al. 07b]. This is a consequence of the six-fold "over-coordination" of Si atoms in that crystal. Thus, all the results presented in this section unambiguously show that bulk fcc-SiN in its state of full symmetry is inherenly unstable.

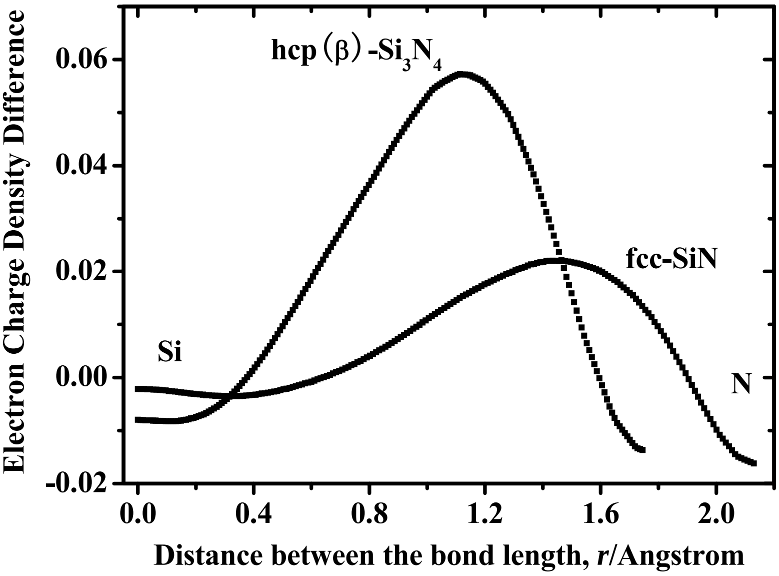

Fig. 3.1.2.11: Line plots of the valence-charge density difference along Si-N bond in fcc-SiN and hcp(ß)- Si_3N_4, respectively.

3.1.2.5 Summary

The fundamental properties, such as equilibrium lattice constant, total energy, bulk modulus, its derivative, and cohesive energy of binary fcc-ZrN, hcp(ß)-Si_3N_4 and fcc-SiN compounds, were calculated by *ab initio* density functional theory. The results are in good agreement with the published experimental and theoretical values. Similarly the ground state properties (total energy, lattice constant) have been also calculated for ternary fcc(NaCl)- and hcp(ß)-$Zr_{1-x}Si_xN_y$ solid solution phases. From these data the interaction parameter at 0 K has been obtained. Using its linear and exponential dependence on temperature, Gibbs free energies of the quasibinary ZrN_y-SiN_y system were constructed, respectively, in order to study the relative phase stability of the metastable ternary fcc(NaCl)- and hcp(ß)- $Zr_{1-x}Si_xN_y$ solution phases over the entire range of compositions. The cross-over points predicted by the exponential equation are in the range of x=0.10–0.15 which is in a good agreement with the experimental results.

The constructed binodal and spinodal curves show that metastable fcc-$Zr_{1-x}Si_xN$ solution phase should spinodally decompose to isostructural fcc-ZrN and hypothetical fcc-SiN as the intermediate state only at relatively high Si content, which would yield much thicker SiN interface. Therefore, the most likely mechanism of the phase segregation is the nucleation and growth of the fcc-ZrN within a tissue of SiN which, in course of continuing decomposition and reaction transform into the thermodynamically stable Si_3N_4. The spinodal decomposition of fcc-$Zr_{1-x}Si_xN$ is possible at high Si fraction. Such a system is, however, unlikely to yield strengthened thin ZrN interface.

The binodal and spinodal curves have also been constructed for hcp(ß)-$(Zr_{1-x}Si_x)_3N_4$. They show that, unlike to fcc(NaCl)-$Zr_{1-x}Si_xN$, the spinodal phase segregation is possible also at a low Si fraction x. However, such a process is unlikely to occur in reality because of the large instability of the hcp-Zr_3N_4 as compared with its fcc- counterpart. Instead, fcc(NaCl)-ZrN and thin X-ray amorphous Si_3N_4-like interfacial phase should form during the final stage of the phase segregation.

Finally we have shown that bulk fcc-SiN is inherently unstable in its fully symmetric configuration, but it may be stabilized by a small distortion that lowers its symmetry, in a similar way as shown recently for the 1 ML fcc-SiN interface.

3.1.3 Al-Si-N system

As outlined in the introduction, the generic design principle for the preparation of the superhard nanocomposites is based on the formation of a nanocomposite due to self-organization upon phase segregation in strongly immiscible quasi-binary systems, such as stoichiometric, hard transition metal nitride in combination with a covalent nitride, such as Si_3N_4 or BN which have been successfully tested so far. Because all these nanocomposites are metallic, it is of interest to elucidate the possibility of the formation of hard or superhard nanocomposites consisting of two, immiscible covalent nitrides. Due to the lack of data regarding the miscibility of Si_3N_4 and BN, we concentrate in this section on the Al-Si-N system which is, when stoichiometric, immiscible

[Rogl & Schuster 92]. Both AlN and Si_3N_4 have stable hexagonal crystal structure and a similar Young's modulus [Holleck 86]. Because both are insulators with relatively large band gap (≤ 5.5 eV for Si_3N_4 [Bekalda et al. 00] and 6 eV for AlN [Speck & Chibu 09]), nanocomposites consisting of these nitrides should be also transparent which would make them potential candidates for applications in optical and optoelectronic devices. SiN_x and AlN thin films were investigated as optical coatings by many researchers (e.g., [Piras et al. 08] and [Dimitrova et al. 98], respectively). Also the deposition of thin films of the ternary Al-Si-N system has been studied by several groups, however with somewhat different results. Some authors reported the formation of $Al_{1-x}Si_xN$ solid solutions [Pélisson et al. 07] [Musil et al. 08] [Liu et al. 09] [Kasu et al. 01], whereas others obtained a mixture of AlN and Si_3N_4 [Zirinsky & Irene 78] [Mazel et al. 97]. Pélisson et al. found that the Al-Si-N films are crystalline with the hexagonal AlN structure up to 12-16 at. % of Si [Pélisson et al. 07]. The observed shift of X-ray diffraction peaks indicates a substitutional incorporation of silicon in the h-AlN lattice up to a solubility limit of 6 at.% of Si. Upon a further increase of the silicon content, nc-$Al_{0.44}Si_{0.06}N_{0.5}$/a-$SiN_x$ nanocomposites were formed. Musil et al. investigated the properties of magnetron sputtered $(Al_{1-x}Si_x)N$ films [Musil et al. 08] and showed that the films with low Si content (≤10 at.%) were polycrystalline whereas those with high Si content of ≥25 at.% were amorphous. The amorphous films exhibited a high hardness of around 25GPa.

Hermann et al. studied the Si doping of AlN films grown by plasma-assisted molecular beam epitaxy (MBE) [Hermann et al. 05]. They reported substitutional Si doping of AlN grown "under N_2-rich" conditions and Si segregation to the surface under "Al-rich" growth conditions”, which obviously contradicts the equilibrium diagrams [Rogl & Schuster 92]. Because the growth conditions are not sufficiently specified in that paper, and in view of the fact that the molecular beam epitaxy operates far from chemical equilibrium, these results cannot be considered as representative for the behavior of the Al-Si-N system. Recently, Liu et al. prepared Al-Si-N nanocomposite films by means of RF balanced magnetron sputtering and showed that a different microstructure development has been found for the films deposited by balanced magnetron sputtering as compared with those prepared by unbalanced magnetron sputtering. A maximum hardness of ≥ 25 GPa has been obtained along with a transition from nanocrystalline to amorphous state, when the Si content increased up to 25 at.%. Si atoms substituted Al in AlN for Si content of ≤ 8 at.% [Liu et al. 09]. In similar studies, Kasu et al. found the formation of $Al_{1-x}Si_xN$ solid solution in a composition range of 0-12 at.% [Kasu et al. 01]. Obviously, the results of many papers quoted here contradict the equilibrium phase diagrams, because the deposition were done under conditions which were not sufficiently specified, but in most cases were remote from equilibrium. This makes an exact comparison and interpretation of the results difficult.

In the work of Weitzer et al. [Weitzer et al. 90] and, Hillert and Jonsson [Hillert & Jonsson 92], which were done under well specified conditions assuring nitrogen stoichiometry and low impurities, only a mixture of AlN and Si_3N_4 were obtained, but neither a ternary compound nor solid solution were found in this system. This is in agreement with the early work of Zirinsky and Irene in 1978 [Zirinsky & Irene 78], who deposited a mixture of AlN and Si_3N_4 films by thermal CVD from $AlCl_3$ and SiH_4 at temperature between 600 ^{o}C and 1100^{o}C. Also Mazel et al., who deposited thin films by means of low pressure CVD from a mixture of $AlCl_3$, $SiCl_3$ and NH_3 diluted by N_2 as carrier gas at temperature between 1000 and 1320°C, found only a mixture of crystalline AlN and Si_3N_4 [Mazel et al. 97].

To summarize this short overview of the experimental work, we conclude that solid solution does not exist in the Al-Si-N system if the deposition is done under conditions of sufficiently high nitrogen pressure and temperature that assure the formation of stoichiometric AlN and Si_3N_4, which are immiscible. The possible role of impurities remains an open issue because of the lack of information provided in the papers. However, one should remember that Al and Si have very high affinity to oxygen. Therefore, minor oxygen impurities may play a large role in these systems.

The theoretical studies of the Al-Si-N system are very limited. Therefore we shall concentrate, in this section, on the *ab initio* DFT and thermodynamic studies as conducted in the foregoing sections.

3.1.3.1 Structural properties and phase stabilities by *ab initio* calculation

For the $Al_{1-x}Si_xN_y$ system, two phase structures have been studied: the hcp(ZnS-type), space group $P6_3/mc$, No. 186 and hcp(ß-type), space group $P6_3/m$, No. 176. The nitrogen molar coefficient $y = 1$ for the hcp(ZnS) and $y = 4/3$ for the hcp(ß) structure. A supercell consisting of 14 atoms has been used for the hcp(ß) and that with 16 atoms for the hcp(ZnS) structure. In both cases, the Al and Si atoms were randomly distributed over the metal sublattice in order to avoid clustering which obviously falsifies the results by decreasing the apparent mixing energy (see remark in [Zhang & Veprek 07). A full relaxation of the lattice constants, internal structure parameters and cell shape for both structures was first performed in order to obtain the most stable geometry with minimum total energy.

Afterwards, the total energies and lattice constants of stable hcp(ZnS)-AlN and hcp(ß)-Si_3N_4, metastable hcp(ß)-Al_3N_4 and hcp(ZnS)-SiN, and the ternary hcp(ZnS)-$Al_{1-x}Si_xN$

(x=0.125, 0.25, 0.375, 0.5, 0.625, 0.75, 0.875) and hcp(ß)-$(Al_{1-x}Si_x)_3N_4$ (x=0.167, 333, 0.5, 0.667, 0.833) phases were calculated with the optimized structure parameters by *ab initio* calculation. These values were then used for the determination of the lattice stabilities of metastable hcp(ß)-Al_3N_4 and hcp(ZnS)-SiN phases with respect to the corresponding stable hcp(ZnS)-AlN and hcp(ß)-Si_3N_4 ones, as well as for the determination of the interaction parameters of the ternary hcp(ZnS)- and hcp(ß)- $Al_{1-x}Si_xN_y$ solid solutions.

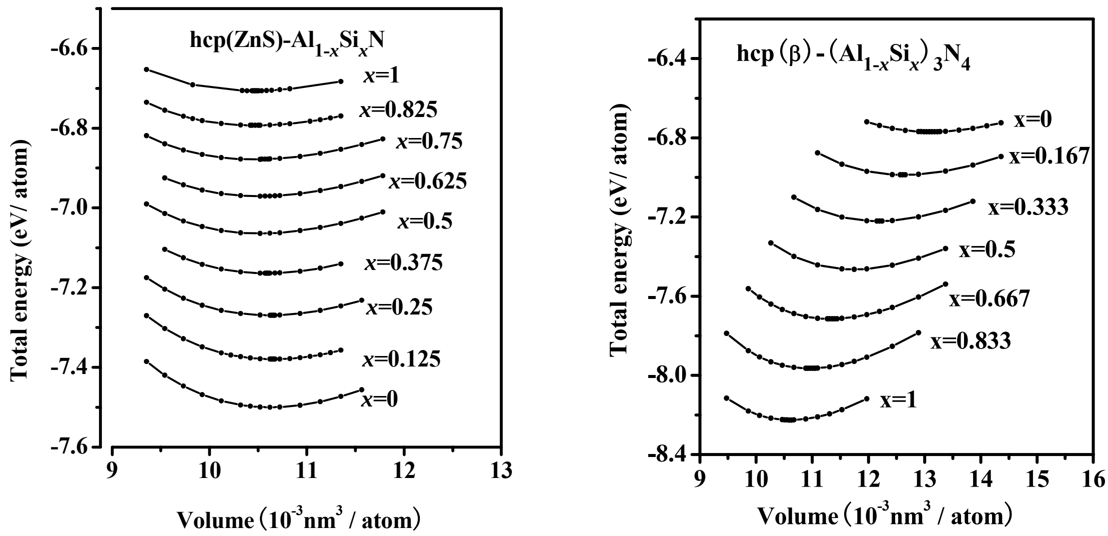

(a) **(b)**

Fig. 3.1.3.1: Dependence of the total energy on the average atomic volume for binary AlN_y, SiN_y compounds and ternary $Al_{1-x}Si_xN_y$ phases in (a) hcp(ZnS) and (b) hcp(ß) structure, respectively.

Because the supercells for hcp(ZnS) structure and hcp(ß) structure have different numbers of atoms, the calculated the *E-V* curves are normalized to the average value per atom, as shown in Fig. 3.1.3.1(a) for ternary hcp(ZnS)-$Al_{1-x}Si_xN$ solid solution with hcp(ZnS)-AlN and -SiN as terminal phases, and in Fig. (b) for hcp(ß)-$(Al_{1-x}Si_x)_3N_4$ solid solution with hcp(ß)-Al_3N_4 and -Si_3N_4 as terminal phases. One notices that the absolute values of the total energies in Fig. (a) and (b) cannot be directly compared because of the difference in the number of atoms in the cell. Nevertheless, it is seen from these figures that the hcp(ZnS) structure is more stable than hcp(ß) one for AlN, whereas the hcp(ß) structure is stable for Si_3N_4, in agreement with the experimental results. Moreover, one can also see from the figures that the change of the equilibrium volume with increasing Si fraction is much smaller for the hcp(ZnS) structure, but it is significant for the hcp(ß) one. This is related to the fact that in the hcp(ZnS) structure, which is the stable one for AlN, the Al atoms are substituted by smaller Si ones (size 0.143 → 0.118 nm) which obviously partially compensates the increasing instability of this phase with increasing Si fraction. In the case of the hcp(ß) structure, which is the stable one for Si_3N_4 but unstable for Al_3N_4, the smaller size of Si and increasing stability of that structure with increasing Si content logically results in the observed decrease of the equilibrium value.

Based on the reaction 4hcp(ZnS)-AlN = hcp(ß)-Al_3N_4 + Al, which corresponds to a low activity of nitrogen, a high lattice instability of hcp(ß)-Al_3N_4 with respect to hcp(ZnS)-AlN, $G_{AlN_y}^{hcp(ZnS)\rightarrow hcp(\beta)}$, of 122.9 kJ/mol·atom has been obtained. Considering the reaction 3hcp(ZnS)AlN + 0.5N2 = hcp(ß)-Al_3N_4, which corresponds to high nitrogen activity, the lattice instability of hcp(ß)-Al_3N_4 is 81.66 kJ/mol·atom. The difference of the two values is due to the different reaction paths and reference states of Al and N_2, respectively. In a similar way, the lattice instability of metastable hcp(ZnS)-SiN with respect to hcp(ß)-Si_3N_4, $G_{SiN_y}^{hcp(\beta)\rightarrow hcp(ZnS)}$, of about 112.8 kJ/ mol·atom has been obtained for the reaction 4hcp(ZnS)-SiN = hcp(ß)-Si_3N_4 + Si and of 145.2 kJ/ mol·atom for the reaction 3hcp(ZnS)-SiN + $0.5N_2$ = hcp(ß)-Si_3N_4.

Figure 3.1.3.2 shows the calculated lattice constants *a* as a function of the composition *x* in the ternary $Al_{1-x}Si_xN_y$ phases with hcp(ZnS) and hcp(ß) structures. With increasing *x*, the lattice constants decrease slightly, showing a negligible positive deviation from the Vegard's law $a_{hcp(ZnS)} = 3.135 - 0.022 \cdot x$ and $a_{hcp(\beta)} = 8.26 - 0.58 \cdot x$ for hcp(ZnS)-$Al_{1-x}Si_xN$ and hcp(ß)-$(Al_{1-x}Si_x)_3N_4$, respectively. This is in agreement with the experimental and theoretical results [Taniyasu et al. 01] [Liu et al. 09]. Taniyasu et al. found that the lattice constants of wurzite $Al_{1-x}Si_xN$ ternary alloys in the strain-free state decreased linearly with increasing Si conten and the lattice constant is obtained by a least-square method as $a_0 = 3.1113 - 0.1412 \cdot x$ with low Si content of $x \leq 8$ %. The X-ray diffraction experiments by Liu et al. also proved the result that the incorporation of Si atom into AlN crystal lattice resulting in a decrease in its lattice parameters. In the foregoing section on the Zr-Si-N system we have reported much larger deviation from the Vegard's law and explained it by the change of the bonding nature when going from the ionic ZrN nitride to the covalent SiN_x one. In the present case, both terminal nitrides are covalent and, therefore, the deviation from the Vegard's law is small.

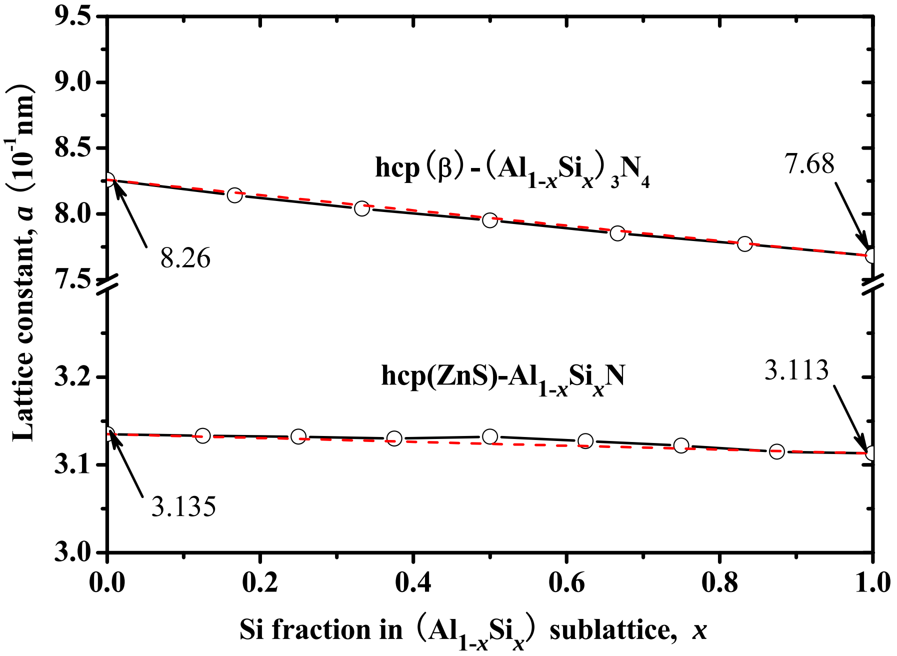

Fig. 3.1.3.2: The calculated lattice constants a as a function of the composition x for hcp(ZnS)- and hcp(ß)- $Al_{1-x}Si_xN_y$, respectively.

3.1.3.2 Combined DFT & Thermodynamic calculations

For the immiscible quasi-binary AlN_y-SiN_y systems, the ternary $Al_{1-x}Si_xN_y$ phases with a structure ψ can be regarded as a continuous solid solution composed of a given fraction of the stoichiometric $\psi - AlN_y$ and $\psi - SiN_y$ phases with the same structure ψ. According to Eq. (2.2.3), the molar Gibbs free energy of the $\psi - Al_{1-x}Si_xN_y$ solution can be expressed by Eq. (3.1.3.1).

$$\begin{aligned} G^{\psi}_{(Al,Si)N} &= (1-x)({}^{0}G^{hcp}_{AlN} + G^{hcp\to\psi}_{AlN}) + x({}^{0}G^{hcp}_{Si_3N_4} + G^{hcp\to\psi}_{Si_3N_4}) \\ &\quad + RT[(1-x)\ln(1-x) + x\ln x] + x(1-x)L^{\psi}_{Al,Si:N} \end{aligned} \qquad (3.1.3.1)$$

The temperature dependence of the Gibbs free energies of the stable phases hcp(ZnS)-AlN and hcp(ß)-Si_3N_4, i.e., ${}^{0}G^{hcp(ZnS)}_{AlN}$ and ${}^{0}G^{hcp(\beta)}_{Si_3N_4}$, respectively, have been obtained by fitting the published data [Barin 93] with Eq. (2.2.4). The resulting polynomial coefficients a to f in Eq. (2.2.4) for hcp-AlN and hcp(ß)-Si_3N_4 have been already reported in Table 3.1.1.II. and 3.1.2.II in the foregoing chapters. The Gibbs free energy of the hypothetical hcp(ZnS)-SiN and hcp(ß)-Al_3N_4 can be approximately expressed by the Gibbs free energy of the stable hcp(ß)-Si_3N_4 and hcp(ZnS)-AlN plus the lattice instability of hcp(ZnS)-SiN and hcp(ß)-Al_3N_4, respectively, which have been calculated in chapter 3.1.3.1.

Next we study the mixing properties of the hcp(ZnS)-$Al_{1-x}Si_xN$ solid solution by considering the reaction $Al_{1-x}Si_xN = (1-x)AlN + \frac{x}{4}Si_3N_4 + \frac{x}{4}Si$, which should occur at low activity of nitrogen for the temperatures considered here. The de-mixing energy of hcp-$Al_{0.5}Si_{0.5}N$ phase with respect to the stable hcp(ZnS)-AlN, hcp(ß)-Si_3N_4 and pure Si is about 60.2 kJ/mol·atom. This value is lower than the previously calculated value of about 74.25 kJ/ mol·atom for the Ti-Si-N system [Zhang & Veprek 07a] [Zhang & Veprek 08] and of 80.88 kJ/mol·atom for Zr-Si-N system. In the case of a high nitrogen activity, where the reaction $Al_{1-x}Si_xN + \frac{x}{6}N_2 = (1-x)AlN + \frac{x}{3}Si_3N_4$ applies, the corresponding de-mixing energy of hcp(ZnS)-$Al_{0.5}Si_{0.5}N$ phase with respect to the stable hcp(ZnS)-AlN, hcp(ß)-Si_3N_4 and pure N_2 is calculated to be about 76.37 kJ/mol·atom. This value is also smaller than the value of about 96.82 kJ/ mol·atom for the Zr-Si-N system calculated in the earlier section and of about 90.5 kJ/ mol·atom reported for the Ti-Si-N system by Zhang and Veprek [Zhang & Veprek 08]. Obviously, the driving force for the segregation of the hcp-$Al_{1-x}Si_xN$ solution to the stable hcp(ZnS)-AlN and hcp(ß)-Si_3N_4 is lower than that for the Ti-Si-N and Zr-Si-N systems. This lower instability of the Al-Si-N solid solutions can be in a somewhat simplified manner understood in terms of the relative smaller difference in the atomic size (atomic radii: Zr 0.160 nm, Ti 0.147 nm, Al 0.143 nm, Si 0.117 nm) and covalent bonding in both AlN and Si_3N_4.

As the next step, we determine the mixing properties with respect to the isostructural terminal phases, i.e., the interaction parameters $L^{hcp(ZnS)}_{Al,Si:N}$ and $L^{hcp(\beta)}_{Al,Si:N}$ at 0 K. As outlined in the introductory chapter, the interaction parameters for the phases with a structure ψ are obtained from Eq. (3.1.3.2)

$$E^{\psi}_{Al_{1-x}Si_xN_y} - (1-x)E^{\psi}_{AlN_y} - xE^{\psi}_{SiN_y} = x(1-x)L^{\psi}_{Al,Si:N} \qquad (3.1.3.2)$$

The composition dependence of the interaction parameter is approximated by the polynomial $({}^0L^{\psi}_{Al,Si:N} + {}^1L^{\psi}_{Al,Si:N} \cdot x + {}^2L^{\psi}_{Al,Si:N} \cdot x^2)$, where ${}^0L^{\psi}_{Al,Si:N}$, ${}^1L^{\psi}_{Al,Si:N}$ and ${}^2L^{\psi}_{Al,Si:N}$ are the composition dependent parameters. After fitting this dependence to the calculated data shown in Fig. 3.1.3.3, we obtained the composition dependence of the interaction parameters $L^{hco(ZnS)}_{Al,Si:N} = (18.305 - 6.286 \cdot x - 1.019 \cdot x^2) \cdot 10^3$ and $L^{hcp(\beta)}_{Al,Si:N} = (2.246 - 3.056 \cdot x - 2.165 \cdot x^2) \cdot 10^4$ J/mol·atom for hcp(ZnS) and hcp(ß)- $Al_{1-x}Si_xN_y$ at 0 K, respectively. It is seen that the curves of both solution phases show positive mixing energies, i.e., they are unstable.

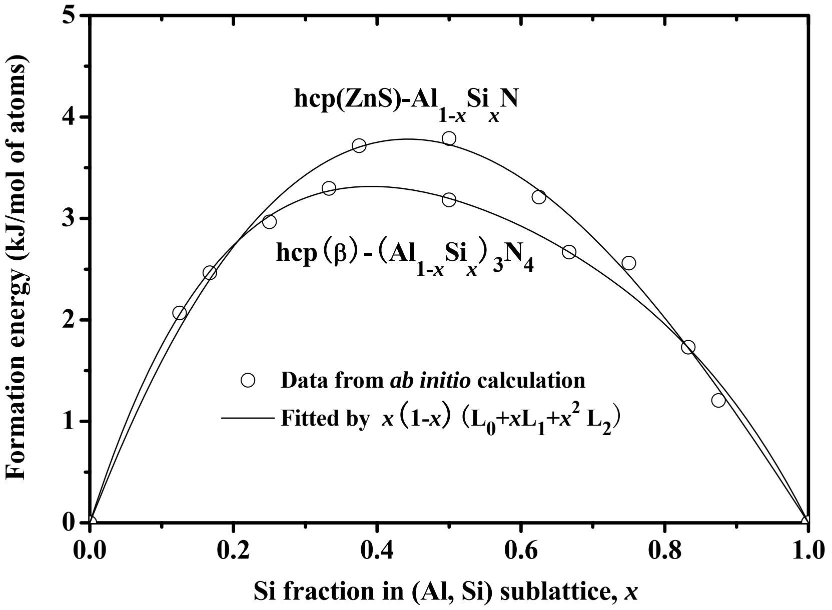

Fig. 3.1.3.3: Fit (lines) of the formation energies, calculated by by *ab initio* DFT (circles), with the function $x(1-x)(L_0+xL_1+x^2L_2)$ for hcp(ZnS)- and hcp(ß)- $Al_{1-x}Si_xN_y$.

As in the foregoing sections, we shall now compare the results obtained with temperature independent, linearly and exponentially dependent interaction parameter. We refer to the foregoing section for further details regarding the methodology, and present here only the results. The only difference is the choice of the critical value of the interaction parameter. In the Zr-Si-N system, only small differences in the results were found regardless if 20 or 50 kJ/mol at melting point were used. However, for Al-Si-N system, the critical interaction parameter around the melting point for hcp-$Al_{0.5}Si_{0.5}N$ is 30 kJ/mol. When a value larger than 30 kJ/mol is used, the *T*-dependence parameter is positive, which is not reasonable. Therefore we use in this study only the value of 20 kJ/mol for the interaction parameter around the melting point of 2470.5 K for hcp-$Al_{0.5}Si_{0.5}N$, which is the average value of the decomposition temperatures for hcp-AlN and ß-Si_3N_4 [Barin 93]. Accordingly, the temperature dependent coefficients of about -1.985 J/mol·K and -1.05 J/mol·K are obtained for hcp(ZnS)- and hcp(ß)-$Al_{1-x}Si_xN_y$ phases, respectively. These values are much less negative than those for Zr-Al-N (-97 and -44 J/mol·K for fcc- and hcp- $Zr_{1-x}Al_xN$, respectively) and for the Zr-Si-N system (-13.71 and -83.25 for fcc- and hcp- $Zr_{1-x}Al_xN$, respectively). Using these values and the calculated lattice instabilities of hypothetical hcp(ZnS)-SiN and hcp(ß)-Al_3N_4 phases, the Gibbs free energies of the mixed ternary Al_{1-}

$_{x}$Si$_{x}$N$_{y}$ phase at temperatures of 0 K, 373 K, 573 K, 773 K, 1073 K, 1273 K and nitrogen pressure of 1 atm have been calculated from Eq. (2.2.6) over the entire compositions. Figure 3.1.3.4 shows the results. The values of the cross-over points of the hcp(ZnS) and hcp(ß) lines corresponding to different temperatures are summarized in Table 3.1.3.I. One sees that at 0 K, the hcp(ZnS) structure is more stable within the composition range of $0 \leq x \leq 0.3577$, whereas the hcp(ß) structure becomes more stable at higher Si fraction. With increasing temperature, the cross-over point moves slightly to a higher Si fraction reaching a value of $x = 0.3612$ at the temperature of 1273 K.

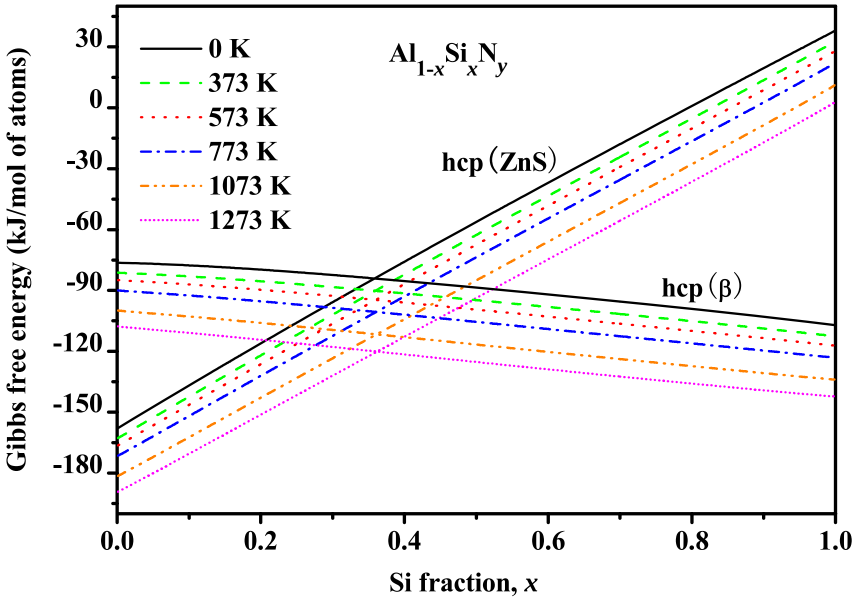

Fig. 3.1.3.4: Gibbs free energy of hcp(ZnS)- and hcp(ß)-Al$_{1-x}$Si$_{x}$N$_{y}$ at temperatures of 0 K, 373 K, 573 K, 773 K, 1073 K, 1273 K with stoichiometric hcp-AlN and hcp-SiN chosen as reference states. The results are within an error of ≤ 0.1 % identical for the choice of linear and exponential *T*-dependence of the interaction parameter (see text).

The exponential dependence of interaction parameter on temperature has been estimated in the same way as in the foregoing section for the Zr-Si-N system (see Eq. (3.1.2.3)). Accordingly, the temperature dependences are $L = (1.8305 \cdot 10^{4}) \cdot e^{\frac{-T}{6188}}$ and $L = (2.2465 \cdot 10^{4}) \cdot e^{\frac{-T}{10700}}$ for hcp(ZnS)- and hcp(ß)- Al$_{1-x}$Si$_{x}$N$_{y}$, respectively. Using these values and the calculated lattice instabilities of hypothetical hcp-Al$_3$N$_4$ and hcp-SiN phases, the Gibbs free energy of the mixed ternary Al$_{1-x}$Si$_{x}$N$_{y}$ phases at different temperatures has been calculated from Eq. (2.2.3) over the entire compositions. The results, when plotted in

Fig. 3.1.3.4, are indistinguishable from those calculated with the linear dependence. This is further supported by the values of the cross-over points in Table 3.1.3.I which show that the results obtained with linear or exponential equation are within an error of ≤0.1 % identical.

Table 3.1.3.I: The cross-over points of hcp(ZnS)- and hcp(ß)- $Al_{1-x}Si_xN_y$ curves , in terms of Si fraction x, for different temperatures as indicated, calculated with linear and exponential T-dependence of the interaction parameter.

Temeperature(K)		0	373	573	773	1073	1273
Cross-over values x	Linear equation	0.3577	0.3590	0.3597	0.3602	0.3609	0.3612
	Exponential equation	0.3577	0.3590	0.3599	0.3603	0.3611	0.3615

The experimental results have shown that incorporation of Si into AlN films increased their microhardness accompanied by changes in microstructure of the films [Liu et al. 09]. The incorporation of Si is substitutional in the hcp(ZnS)-AlN crystal lattice up to a critical concentration of 12 to 16 at.%, above which nanocomposites film forms and the hardness reaches a maximum of about 30 GPa [Pélisson et al. 07]. Also Kasu et al. has found similar results in the composition range of 0-12 at.% with the "maximum solubility" of Si in the hcp(ZnS)-AlN around 12 at.% [Kasu et al. 01]. However, Liu et al. reported a maximum hardness of ≥ 25 GPa for Si fraction of ≥ 25 at.% when the microstructure of the films transforms from nanocrystalline to amorphous. Obviously, there are some discrepancies between the different experimental works. The possible reasons are different deposition temperature used, possibly nitrogen substoichiometry and impurities. Let us point out that Pélisson et al. reported oxygen impurities in their film determined by XPS after sputter-cleaning of about 4±2 at.% [Pélisson et al. 07]. For these reasons, the possibilities of a comparison of the results obtained in our calculations with experiments are limited.

3.1.3.3 Possibility of chemical and coherent spinodal decomposition

Figure 3.1.3.5 shows the Gibbs free energy of the formation of hcp(ZnS)-$Al_{1-x}Si_xN_y$ solid solution as a function of composition for temperatures of 0 K, 373 K, 573 K, 773 K, 1073 K, 1273 K and nitrogen pressure of 1 atm, with isostructural hcp(ZnS)-AlN and hcp(ZnS)-SiN as the reference states for hcp(ZnS)-$Al_{1-x}Si_xN$ (Fig. (a)), and hcp(ß)-Al_3N_4 and hcp(ß)-Si_3N_4 as the reference states for hcp(ß)-$(Al_{1-x}Si_x)_3N_4$ (Fig. (b)). For the hcp(ZnS)-Al_{1-}

$_x$Si$_x$N, it can be seen in Fig. (a) that, for the typical deposition temperature of ≤ 773 K, the dependence of the Gibbs free energy of the immiscible system is typical of chemical spinodal, i.e., $\frac{\delta^2 G_f^0(x)}{\delta x^2} < 0$, within a large composition range, particularly on the Al-rich side. However, because the values of the de-mixing energies are relatively small, it is doubtful if the system may be also coherently spinodal. With increasing temperature, the Gibbs free energy of de-mixing decreases and the composition range for chemical spinodal decreases as well. At the temperature of 1273 K, the whole curve lies below zero showing that the Al-Si-N system is miscible within the whole composition range. The situation is similar for the hcp(ß)-$(Al_{1-x}Si_x)_3N_4$ phase (Fig. (b)). At the low temperatures of ≤ 573 K, the maximum Gibbs free energy is slightly lower than that for hcp(ZnS)-$Al_{1-x}Si_xN$, but it is somewhat higher for $T \geq$ 773 K. At the highest temperature of 1273 K, there is an immiscibility region for low Si-fraction. This is most probably related to the instability of the hcp(ß)-Al_3N_4.

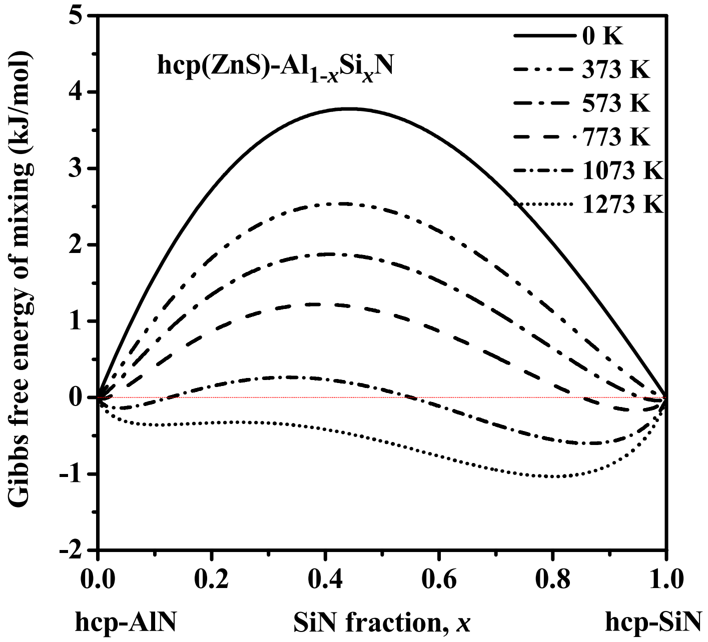

Fig. 3.1.3.5 (a): Gibbs free energy of mixing of hcp(ZnS)-$Al_{1-x}Si_xN$ phase ΔG as a function of composition for temperatures 0 K, 373 K, 573 K, 773 K, 1073 K, 1273 K, where ΔG>0, with isostructural hcp(ZnS)-AlN and hcp(ZnS)-SiN as reference states.

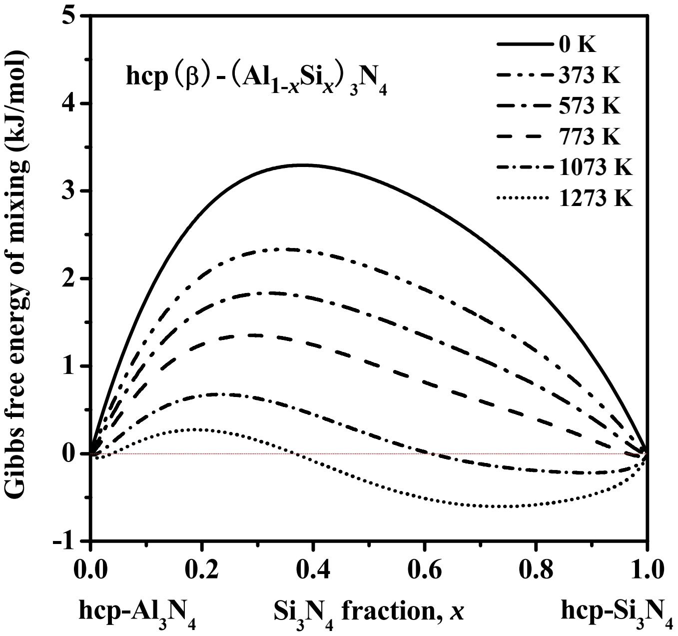

Fig. 3.1.3.5 (b): Gibbs free energy of mixing hcp(ß)-$(Al_{1-x}Si_x)_3N_4$ phase ΔG as a function of composition for temperatures 0 K, 373 K, 573 K, 773 K, 1073 K, 1273 K, where $\Delta G>0$, with isostructural hcp(ß)-Al_3N_4 and hcp(ß)-Si_3N_4 as reference states.

Figure 3.1.3.6 shows the phase stability diagrams of hcp(ZnS)-$Al_{1-x}Si_xN$ as the function of Si fraction x with hcp(ZnS)-AlN and hcp(ZnS)-SiN as reference states for (a) the temperature independent, (b) linearly, and (c) exponentially T-dependent interaction parameter. It can be seen that for a temperature of < 1000 K, the binodal curve is close to the y-axes, i.e. hcp(ZnS)-AlN and hcp(ZnS)-SiN are immiscible. The composition range for the chemical spinodal is within few % similar for all three case of the T-dependence of the interaction parameter considered. As in the previous examples, the maximum spinodal temperature is higher in the case of T-independent interaction parameter, but the difference of only about 6 % is very small as compared with the Zr-Si-N system.

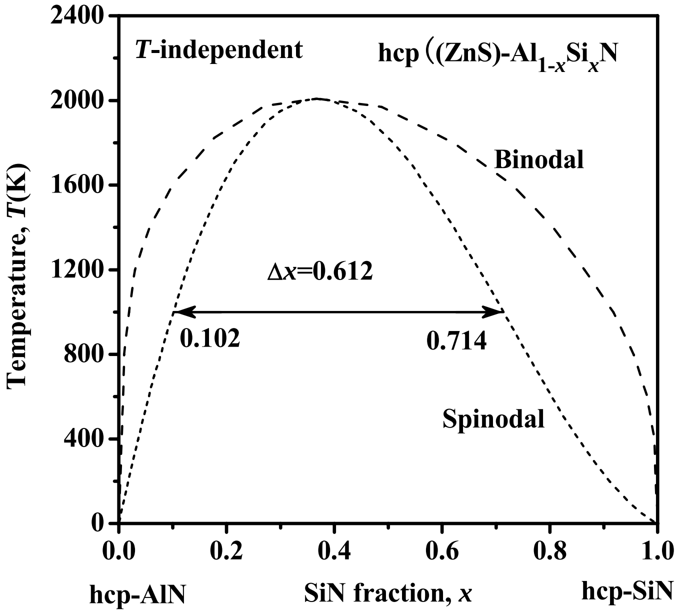
2400
2000
1600
1200
800
400
0
Temperature, T(K)
T-independent
hcp ((ZnS)-Al1-xSixN
Binodal
Δx=0.612
0.102
0.714
Spinodal
0.0
0.2
0.4
0.6
0.8
1.0
hcp-AlN
SiN fraction, x
hcp-SiN

(a)

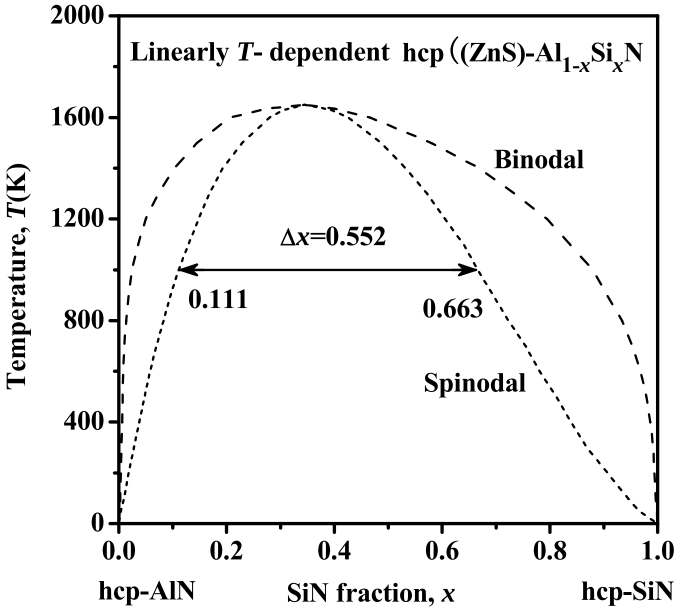
2000
1600
1200
800
400
0
Temperature, T(K)
Linearly T- dependent
hcp ((ZnS)-Al1-xSixN
Binodal
Δx=0.552
0.111
0.663
Spinodal
0.0
0.2
0.4
0.6
0.8
1.0
hcp-AlN
SiN fraction, x
hcp-SiN

(b)

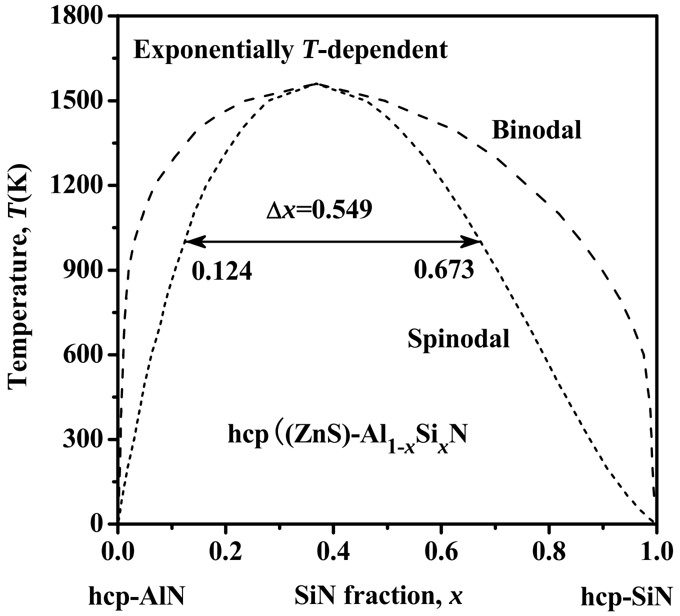

(c)

Fig. 3.1.3.6 Temperature-composition phase diagram for hcp(ZnS)-$Al_{1-x}Si_xN$ showing the spinodal (short dashed line) and binodal (dashed lines) curves with hcp(ZnS)-AlN and hcp(ZnS)-SiN chosen as reference states calculated with (a) temperature independent, (b) linearly and (c) exponentially temperature dependent interaction parameter.

Figure 3.1.3.7 shows the phase stability diagrams of hcp(ß)-$(Al_{1-x}Si_x)_3N_4$ as the function of Si fraction x with hcp(ß)-Al_3N_4 and hcp(ß)-Si_3N_4 as reference states. From the figure it is seen that both binodal and spinodal curves show different shapes compared with those in Fig. 3.1.3.6, as well as with those in the Zr-Al-N and Zr-Si-N systems. The "secondary spinodal", which appears in a relatively narrow, Si-rich region of $x = 0.6626$ to 0.8428, is related to minor changes of the corresponding curves in Fig. 3.1.3.5 (b) which are almost linear in this range. Because the curves in Fig. 3.1.3.7 correspond to second derivatives of the curves in Fig. 3.1.3.5 (b), minor variations in the slope of the latter curves result in fairly large changes of the former ones. Therefore one should not overestimate the importance of this "secondary" spinodal.

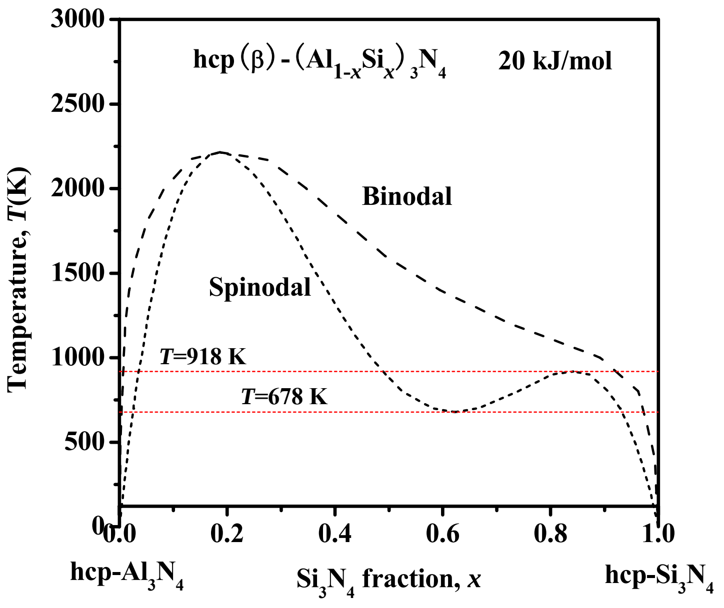

Fig. 3.1.3.7: Calculated temperature-composition phase diagram for hcp(ß)-$(Al_{1-x}Si_x)_3N_4$ showing the binodal (dashed line) and spinodal (short dashed line) curves with hcp(ß)-Al_3N_4 and hcp(ß)-Si_3N_4 as reference states.

Compared with the Zr-Si-N (see above) and Ti-Si-N system [Zhang & Veprek 08], the de-mixing energy is orders of magnitude smaller in the Al-Si-N system, Thus, although chemically spinodal regime is found which might allow the formation of the nanocomposites with a thin interfacial layer of either SiN_x or AlN in the Al- and Si-rich compositions, respectively, such process seems to be unlikely because the coherence lattice energy may hinder the system to undergo coherently spinodal decomposition. One notices that the maximum de-mixing energy of $\leq$ 3.5 kJ/mol found for this system is comparable with the elastic strain energy of semi-coherent interfaces [Zhang & Veprek 06].

This, however, does not mean that hard AlN-Si_3N_4 nanocomposites may not be possible to prepare. At the typical deposition temperature of 500°C, the average diffusion length of 5 nm is achieved on the time scale of few 100 s. As discussed recently [Veprek et al. 09], this possibly determines the average size of the diffusion-controlled phase segregation. Because with the formation of the stable hcp(ZnS)-AlN and hcp(ß)-Si_3N_4 phases, the de-mixing energy of the stoichiometric $(Al_{1-x}Si_x)_3N_4$ is strongly increased by the transitions SiN → Si_3N_4 and Al_3N_4 → AlN. However, this problem cannot be handled by conventional thermodynamics which deals with closed systems. Instead, one may try the approach of the "mechanical mixtures" of the stable phases as used in [Zhang & Veprek 06]. This is however beyond the scope of the present work.

3.1.3.4 Summary

The fundamental properties of binary stable hcp(ZnS)-AlN, hcp(ß)-Si_3N_4 and metastable hcp(ZnS)-SiN and hcp(ß)-Al_3N_4 compounds, and of ternary $Al_{1-x}Si_xN_y$ solution phases were calculated by means of *ab initio* density functional theory. The results are in good agreement with the available experimental and theoretical data.

The temperature dependence of the interaction parameters of about -1.985 J/mol·K and -1.05 J/mol·K, calculated for hcp(ZnS)- and hcp(ß)- $Al_{1-x}Si_xN_y$ phases, respectively, are much less negative than those for the Zr-Al-N (-97 and -44 J/mol·K for fcc- and hcp-$Zr_{1-x}Al_xN$, respectively) and for the Zr-Si-N systems (-13.71 and -83.25 J/mol·K for fcc- and hcp- $Zr_{1-x}Si_xN$, respectively).

The Gibbs free energies of the quasi-binary AlN_y-SiN_y system were constructed using the linear and exponential temperature dependences of interaction parameter, in order to study the relative phase stability of the metastable ternary hcp(ZnS)- and hcp(ß)-$Al_{1-x}Si_xN_y$ solution over the entire range of compositions. Because of the T-dependence of the interaction parameter is much smaller for this system than for the Zr-Si-N and Ti-Si-N ones, there is only a small difference of the results when the T-independent interaction parameter has been used, and the difference between the results obtained with linear and exponential T-dependence are negligible. The cross-over points between the hcp(ZnS) and hcp(ß) phases are in the range of x=0.3577–0.3615 indicating a higher "solubility limit" [5] of Si in hcp(ZnS)-AlN compared with the experimentally reported values, whose reliability should be subject to further tests.

The dependence of the Gibbs free energy of the mixing on composition obtained for $Al_{1-x}Si_xN_y$ ternary alloys with both hcp(ZnS) and hcp(ß) structure show that, for the typical deposition temperature of $\leq$ 773 K, the systems are immiscible with dependences typical of chemical spinodal. With increasing temperature, the Gibbs free energy of de-mixing decreases fast, and the composition range for chemical spinodal decreases as well. At lower temperature the maximum Gibbs free energy of mixing for hcp(ß)-$(Al_{1-x}Si_x)_3N_4$ phases is slightly lower than that for hcp(ZnS)-$Al_{1-x}Si_xN$. At the highest temperature of 1273 K, the hcp(ZnS)-$Al_{1-x}Si_xN$ is miscible.

---

[5] Recall that the term "solubility limit" refers to equilibrium whereas here we are dealing with the limit of stability of certain structure of an unstable solid solution. Nevertheless, we use this term because it is used in many recent papers.

The binodal and spinodal curves were constructed for both hcp(ZnS)-$Al_{1-x}Si_xN$ and hcp(ß)-$(Al_{1-x}Si_x)_3N_4$ solution phases. The results for hcp(ZnS)-$Al_{1-x}Si_xN$ show that metastable hcp(ZnS)-$Al_{1-x}Si_xN$ solution phases might spinodally decompose to isostructural hcp(ZnS)-AlN and hypothetical hcp(ZnS)-SiN. However, considering the large lattice instability of hcp(ZnS)-SiN compared with stable hcp(ß)-Si_3N_4, the decompositon is likely to be accompanied by a phase transformation from unstable hcp(ZnS)-SiN to the stable hcp(ß)/amorphous-Si_3N_4. From the comparison of the results for hcp(ZnS)-$Al_{1-x}Si_xN$ and hcp(ß)-$(Al_{1-x}Si_x)_3N_4$, it is found that in the Al-rich region with low Si content, the spinodal phase segregation is more favorable for hcp(ZnS)-$Al_{1-x}Si_xN$ phases than for hcp(ß)-$(Al_{1-x}Si_x)_3N_4$.

3.1.4 Zr-Al-O system

In the foregoing sections, we have studied the thermodynamic properties of the Zr-Al-N, Zr-Si-N and Al-Si-N systems by the combined *ab initio* DFT method and thermodynamic calculations. In this section we will focus on the oxide system Zr-Al-O because it has an "infinitive" oxidation resistance, that is important in the applications as wear protective coatings on cutting tools, and is expected to be spinodal.

Oxide systems are of large interests because of their relatively high hardness and mechanical strength, high melting point, oxidation resistance, high thermal stability, and excellent chemical inertness [Rice 00] [Knauth & Schoonman 02]. This has led to many fundamental theoretical and experimental investigations as well as to applications such as hard coatings, diffusion and reaction barriers and others. Crystalline α-alumina (α-Al_2O_3, called in this section "hcp-Al_2O_3" to account also for the ternary solid solution) is mostly used as hard, wear protection coating on tools because of its high chemical and thermal stability, and high hardness of about 20-22 GPa [Berg et al. 00] [Åstrand et al. 04]. In the past decades, thin coatings of α-Al_2O_3 were deposited by the conventional CVD at high temperature of about 1000 °C, because at lower temperature the soft tetragonal γ-phase is formed. Only recently, hard α-Al_2O_3 could be deposited by PVD at temperatures of $\geq$ 700°C by reactive sputtering (e.g. [Kohara et al. 04]) or at $\leq$ 600°C by pulsed vacuum arc [Ramm et al. 07].

Zirconia (ZrO_2) has many important applications because of its high refractive index, high melting temperature, hardness of 13-16 GPa [Berg et al. 00] and corrosion resistance. At ambient pressure, ZrO_2 forms three phases [Jomard et al. 99] [Zhao & Vanderbilt 02]: monoclinic, tetragonal and cubic. The monoclinic phase (space group $P2_1/c$) is thermodynamically stable below 1400 K, above which it transforms to the tetragonal structure (space group *P*42/*nmc*). It is a slightly distorted version of the cubic structure. At about 2570 K, the tetragonal phase transforms to the cubic one (space group *Fm*-3*m*) which is stable up to the melting temperature of 2980 K.

Inspired by the high performance of nitride based superhard nanocomposite coatings, researchers have attempted to prepare nanocomposties on the basis of Al_2O_3 and a second oxide phase [Klostermann et al. 05] [Jia et al. 06]. Because of the known immiscibility of alumina and zirconia, the system Al_2O_3 + ZrO_2 has been chosen by Klostermann et al. [Klostermann et al. 05], who succeeded to prepare nc-Al_2O_3/ZrO_2 nanocomposite films by pulsed magnetron sputtering (PMS). The hardness of these coatings reached up to 30 GPa when the ZrO_2 content has been around 7-8 at.%, i.e., significantly higher than the hardness of the pure oxides. When the ZrO_2 content increased above 10 at.%, the films were amorphous with a low hardness of 10 to 13 GPa. At low Al_2O_3 content, the films are crystalline again with ZrO_2 being the dominant phase, and their hardness of about 17 GPa is intermediate between that of ZrO_2 and α-Al_2O_3 [Koski et al. 99]. For example, in a film containing 7.5 at.% Al_2O_3, only tetragonal ZrO_2 has been found by XRD, whereas pure ZrO_2 films are monoclinic.

Trinh et al. found that the Al_2O_3-ZrO_2 thin films grown by reactive dual radio-frequency magnetron sputtering contained either an amorphous phase, γ- Al_2O_3, cubic ZrO_2 or a mixture of these, whereas pure ZrO_2 films were monoclinic and pure Al_2O_3 ones had the γ-phase [Trinh et al. 06] [Trinh et al. 08] [Trinh et al. 08b]. The grain size was around 5 nm in the nanocomposites, but larger in the pure oxide films. Electron energy loss spectroscopy showed a well defined transition from the pure Al_2O_3 to the pure ZrO_2. Because the applications of cutting tools are limited to temperatures of about ≤ 1100°C, we shall focus, in the present study, on the monoclinic ZrO_2 and α-Al_2O_3 phases.

The theoretical investigations of phase stabilities of the ternary and multi-component transition metal oxides are still absent due to their complexity. Therefore, we shall, in this work, use the combined *ab initio* DFT calculation and thermodynamic modeling, which has been successfully applied for the ternary nitrides systems Ti-Si-N [Zhang & Veprek 08], Ti-Al-N [Zhang & Veprek 07], Cr-Al-N [Zhang & Veprek 07b], Zr-Al-N [Sheng et al. 08] and Ti-B-N [Zhang et al. 08b], as well as for the Zr-Si-N and Al-Si-N systems studied in the previous sections. By analogy with the latter studies, we shall compare results obtained with temperature independent, as well as linearly and exponentially dependent interaction parameter.

3.1.4.1 Structural properties and phase stabilities by *ab initio* DFT calculation

The monoclinic structure of ZrO_2 ("mono-ZrO_2") can be described as a distorted fluorite structure with the Zr atoms in coordination sites shown in Fig. 3.1.4.1(a). The cell parameters are a, b, c and γ. There are two oxygen sites in the lattice: one O site (O_I) is coordinated to three Zr atoms in an almost planar environment, and the other O site (O_{II}) is surrounded by a distorted tetrahedron of Zr atoms. The coordinates of the atoms are given by the Wyckoff notations $\pm(x, y, z)$; $\pm(-x, y+1/2, 1/2-z)$.

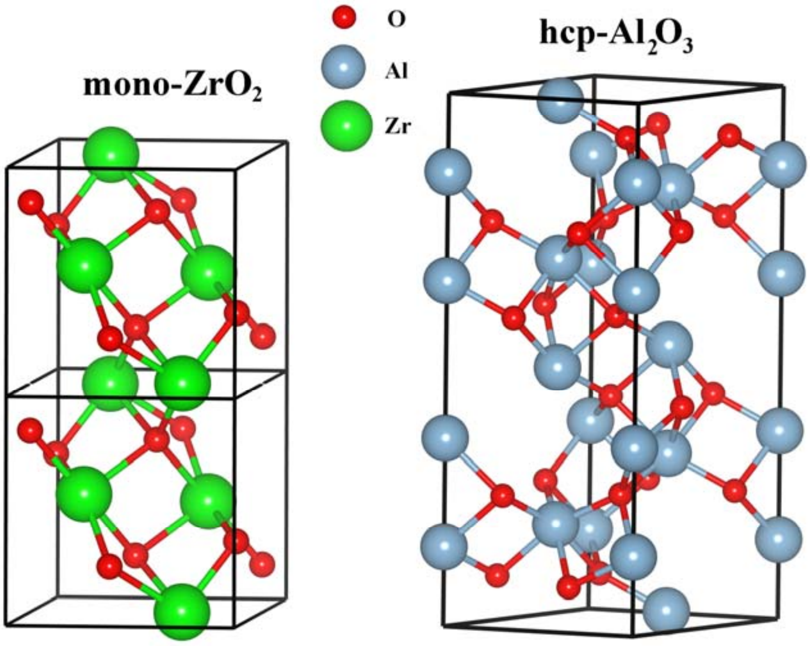

(a) (b)

Fig. 3.1.4.1: Crystal structures of (a) mono-ZrO_2 and (b) hcp-Al_2O_3; large green spheres are Zr in Fig. (a), large blue spheres are Al in Fig. (b), and small red spheres are O atoms.

Sapphire, α-Al_2O_3, belongs to the space group R-3c, and its structure is described by Kronberg [Kronberg 57] and by Lee and Lagerlof [Lee & Lagerlof 85]. Many researchers have analyzed the correlations of the structure with the plastic deformation mechanism and the formation of twins [Kronberg 57] [Scott & Orr 83]. The crystal structure is described as the O^{2-} anions arranged in an approximately hcp lattice while the Al^{3+} cations are located in two thirds of the octahedral sites. The hexagonal crystal structure of α-Al_2O_3 is shown in Fig. 3.1.4.1(b). The close-packed directions in the anion sublattice lie along $<10\bar{1}0>$, whereas the close-packed directions of the metals are along $<11\bar{2}0>$ direction. The hexagonal unit cell, which properly accounts for the combined anion and cation sublattices, is twice the volume of the morphological unit cell as defined by mineralogists, and rotated by 180^{o} around the c-axis.

The standard crystallographic data of α-Al_2O_3 structure are specified in the *International Tables for X-ray Crystallography* [Kasper & Lonsdale 72] as follows: Lattice constants: a_0 = 0.47589 nm, c_0 = 1.2991 nm, cell volume V = 0.2548 nm^3**,** formula units per cell n = 6 and atomic positions 12 Al^{3+} ions located at 12c positions ((0, 0, 0); (1/3, 2/3, 2/3); (2/3, 1/3, 1/3)) + (0, 0, *u*); (0, 0, -*u*); (0, 0, ½+*u*)**;** (0, 0, ½-*u*) where *u* = 0.3520, and 18 O^{2-} ions located at 18e positions ((0, 0, 0); (1/3, 2/3, 2/3); (2/3, 1/3, 1/3)) + (*v*, 0, 1/4); (0, *v*, 1/4); (*v*, *v*, -1/4); (-*v*, 0, -1/4); (0, -*v*, -1/4); (-*v*, -*v*, 1/4) where *v* = 0.306. The conversion between hexagonal Miller-Bravais indices and rhombohedral Miller indices for the structural unit cells is easily performed by a matrix multiplication (see [Lee & Lagerlof 85] for more details).

In view of the complexity of the structure of the Zr-Al-O system, we use special *k* points of the 5×5×5 Monkhorst-Pack grid for the integration in the Brillouin zone with the energy cutoff of 600 eV. The conjugate gradient method has been used for the relaxation of structural parameters. By application of the above crystallographic specifications, we set up a 24 atoms and a 30 atoms cell for the mono-ZrO_2 and hcp(α)-Al_2O_3, respectively, and perform the optimization of the geometry and full relaxation for the cell axes, as well as of all internal structure parameters. These structures will be used for the construction of the substitution ternary solution with monoclinic and hcp- structures.

The optimized values of α_{rho} (an angle between lattice vectors), u_{Al} and v_O (internal parameters for Al and O in rhombohedral representation) for hcp(α)-Al_2O_3, the internal structural parameters for mono-ZrO_2, as well as the published experimental and theoretical data, are listed in Table 3.1.4.I. It is seen that our calculated values are in good agreement with the experimental and theoretical data. In the following, the hexagonal cell is used to describe the hcp(α)-Al_2O_3.

Table 3.1.4.I: The internal structural parameters for the mono-ZrO_2 and hcp-Al_2O_3 obtained from the *ab initio* calculation and their comparison with published experimental and theoretical data.

Phase	Parameter	Present (GGA)	Expt.	GGA	LDA
hcp-Al_2O_3 (Rhombohedral representation)	α_{rho} (deg)	55.32	55.28[b,c]	55.32[a]	55.37[a]
	u_{Al}	0.352	0.352[b,c]	0.353[a]	0.352[a]
	v_O	0.307	0.306[b,c]	0.306[a]	0.306[a]
mono-ZrO_2	γ (deg)	99.59	99.23[d]	99.23[f]	99.23[f], 99.21[e]
	x_{Zr}	0.2766	0.2758[g,f], 0.2754[d]	0.2773[f]	0.2777[f] 0.2769[e]
	y_{Zr}	0.0432	0.0404[g,f], 0.0395[d]	0.0416[f]	0.0418[f], 0.0422[e]
	z_{Zr}	0.2098	0.2089[g,f], 0.2083[d]	0.2103[f]	0.2101[f], 0.2097[e]
	x_{OI}	0.0687	0.069[g,f], 0.0700[d]	0.071[f]	0.071[f], 0.0689[e]
	y_{OI}	0.3333	0.342[g,f], 0.3317[d]	0.336[f]	0.337[f], 0.3333[e]
	z_{OI}	0.3446	0.345[g,f], 0.3447[d]	0.341[f]	0.342[f], 0.3445[e]
	x_{OII}	0.4499	0.451[g,f], 0.4496[d]	0.448[f]	0.449[f], 0.4495[e]
	y_{OII}	0.7577	0.758[g,f], 0.7569[d]	0.757[f]	0.757[f], 0.7573[e]
	z_{OII}	0.4782	0.479[g,f], 0.4792[d]	0.479[f]	0.480[f], 0.4798[e]

Note : [a] = [Matsunaga et al. 03]; [b] = [Amour et al. 78]; [c] = [Lee & Lagerlof 85]; [d] = [Stefanovich et al. 94]; [e] = [Zhao & Vanderbilt 02]; [f] = [Jomard et al. 99]; [g] = [Wyckoff 63].

Using our optimized geometry for hexagonal and monoclinic structure, the total energies and the cell volumes of the stable mono-ZrO_2 and hcp-Al_2O_3, and of the hypothetical hcp-Zr_2O_3 and mono-AlO_2 were calculated. In order to study the composition dependence of the mixing properties, we further calculated the total energies of ternary mono-$(Zr_{1-x}Al_x)O_2$ and hcp-$(Zr_{1-x}Al_x)_2O_3$ solid solution phases with different compositions using a supercell setup containing 24 atoms for monoclinic structure and 30 atoms for hexagonal structure as for the pure terminal phases. Zr and Al atoms are randomly distributed over the metal sublattice so that Zr (or Al) is surrounded by the other element, i.e., by Al (or Zr). This avoids clustering which would decrease the total energy of the solution. In order to maintain the crystal symmetry, the cell shape is kept unchanged during the substitution, i.e., only the substitution effects on total energy are considered. This is an extreme case because the clustering, which represents the onset of the decomposition, decreases the de-mixing energy of the ternary system.

The total energies and the cell volumes of the binary stable mono-ZrO_2 and hcp-Al_2O_3, of the hypothetical hcp-Zr_2O_3 and mono-AlO_2, and of the ternary mono- and hcp-$Zr_{1-x}Al_xO_y$ solution phases were calculated. These values were then used for the determination of the lattice instabilities of hypothetical hcp-Zr_2O_3 and mono-AlO_2 phases with respect to the corresponding stable mono-ZrO_2 and hcp-Al_2O_3 phases, as well as for the determination of the interaction parameters of the ternary mono- and hcp-$Zr_{1-x}Al_xO_y$ solid solution phases at 0 K.

The formation enthalpies are obtained by considering the reaction to form (or decompose) crystalline oxides from (or into) the elementary substances, i.e., $x\cdot$Me(solid) + $(y/2)\cdot O_2$(gas) = Me_xO_y. From the respective total energies of the phases we obtain the formation enthalpies by Eq. (3.1.4.1).

$$\Delta H_f(Me_xO_y) = -E(Me_xO_y) + xE(Me-solid) + \frac{y}{2}E(O_2-gas) \qquad (3.1.4.1)$$

Where $E(Me_xO_y)$, $E(O_2\text{-}gas)$ and $E(Me\text{-}solid)$ are the total energies of the bulk Me_xO_y, of the free O_2 molecule, and of the solid Me. In agreement with the usual nomenclature, a negative formation enthalpy value applies for an exothermic, and a positive value for an endothermic reaction. In order to calculate the total energy of O_2 molecule, a cubic cell with the side length of 0.8 nm is constructed with two O atoms placed inside, and a full relaxation is then performed to get the stable geometry. The total energy of O atom is calculated by the same method. The calculated O-O bond length of 0.124 nm is in good agreement with that of 0.124 nm calculated by Shi et al. [Shi et al. 07] and with the experimental value of 0.121 nm [Huber & Herzerg 79]. The calculated O_2 binding energy of 3.34 eV per O atom is similar to other calculated values of 3.12 eV [Li et al. 02] and 3.13 eV [Perdew et al. 96], and somewhat larger than the experimental value of 2.56 eV [Huber & Herzerg 79]. This difference is typical for well-converged DFT-GGA calculations.

In order to check the reliability of our calculations of the solid phases, the equilibrium volume V_0, total energy E_0, bulk modulus B_0 and its first derivative B_0' of the binary mono-ZrO_2 and hcp-Al_2O_3 phases were calculated from the dependence of E on V using the Murnaghan equation of state (Eq. (2.2.2)) [Murnaghan 44], as outlined in Sect. 2.2. The results are summarized in Table 3.1.4.II. The formation enthalpies calculated from Eq.

(3.1.4.1) are also included in that Table. It is seen that our results agree reasonably well with the published experimental and theoretical data, thus confirming the reliability of the applied potentials and methods.

Table 3.1.4.II: The equilibrium cell volume V_0, total energy E_0, bulk modulus B_0, pressure derivative B_0' and the formation enthalpy ΔH_f for mono-ZrO_2 and hcp-Al_2O_3 obtained by fitting *E-V* data, obtained from the *ab initio* calculation, to the Murnaghan's equation of state [Murnaghan 44].

Phase		V_0 (nm^3/atom)	E_0 (eV/atom)	B_0 (GPa)	B_0'	ΔH_f (kJ/mol·atom)
mono-ZrO_2	Murnaghan	0.012214	-9.5377	222.305	4.33	-333.076
	Others	0.012343[i]		95-189[ii]	4.0[iii]	-365.821[v]
		0.01174[ii]		186[iii]		
		0.01187[iii]		212[iv]		
hcp-Al_2O_3	Murnaghan	0.008746	-7.565	227.928	4.98	-303.026
	Others	0.0082[iii]		241[iii]		-335.138[v]
		0.00849[iii]		254[iii]		

Note: [i] = [Jomard et al. 99]; [ii] = [Howard et al. 88]; [iii] = [Iuga et al. 07]; [iv] = [Desgreniers & Lagarec 99] ; [v] =[Barin 93].

Now we discuss the lattice instability of hypothetical mono-AlO_2 with respect to hcp-Al_2O_3 by the *ab initio* DFT method. For simplicity, we regard the lattice instability as a temperature-independent parameter. Based on the reaction $3AlO_2+Al = 2Al_2O_3$, a high lattice instability, $G_{Al_2O_3}^{hcp \to mono}$, of 127.644 kJ/mol·atom of mono-AlO_2 with respect to hcp-Al_2O_3 is obtained. For the reaction $4AlO_2 = 2Al_2O_3 + O_2$, which corresponds to high oxygen pressure, the calculated lattice instability of mono-AlO_2, $G_{Al_2O_3}^{hcp \to mono}$, of 57.652 kJ/mol·atom results. The difference of the two values is due to the different definitions of reaction paths and of the reference states. In both cases, the mono-AlO_2 is unstable and should transform to hcp-Al_2O_3. Similarly, the lattice instability of hcp-Zr_2O_3 with respect to mono-ZrO_2, $G_{ZrO_2}^{mono \to hcp}$, of about 16.988 kJ/mol·atom is obtained from the reaction $3ZrO_2 + Zr = 2Zr_2O_3$, and of about 97.426 kJ/mol·atom from the reaction $4ZrO_2 = 2Zr_2O_3 + O_2$. Thus, also the hypothetical hcp-Zr_2O_3 is unstable as compared to the stable monoclinic ZrO_2.

Figure 3.1.4.2 shows the calculated cell volume as a function of the Al fraction x in the $(Zr_{1-x}Al_x)$ sublattice of the ternary $Zr_{1-x}Al_xO_y$ phases with monoclinic and hexagonal structures.[6] It is found that with increasing Al fraction, the mole volumes in both curves decrease. This is due to the smaller atomic radius of Al of 0.143 nm as compared with that of Zr of 0.160 nm.

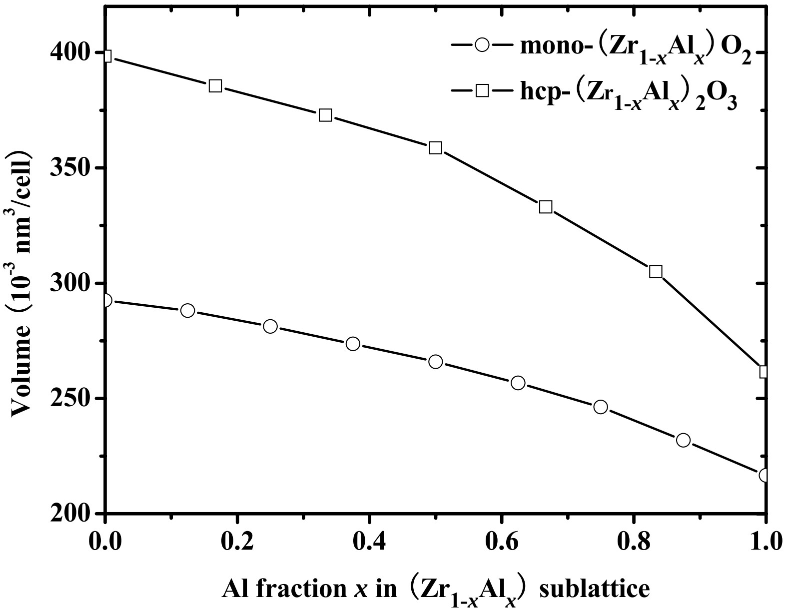

Fig. 3.1.4.2. The calculated cell volume as a function of the Al fraction x for the ternary $Zr_{1-x}Al_xO_y$ phases with monoclinic and hexagonal structures, respectively.

3.1.4.2 Combined DFT & thermodynamic calculations

For the immiscible quasi-binary ZrO_y-AlO_y systems, the ternary $Zr_{1-x}Al_xO_y$ phases with a structure ψ can be regarded as a continuous solid solution composed of a given fraction of the stoichiometric ψ-AlO_y and ψ-ZrO_y phases with the same structure ψ. According to Eq. (2.2.3), the molar Gibbs free energy of ψ-$Zr_{1-x}Al_xO_y$ solution phase can be expressed by Eq. (3.1.4.2).

$$\begin{aligned} G^{\psi}_{Zr,Al:O} &= (1-x)({}^{0}G^{mono}_{ZrO_2} + G^{mono\to\psi}_{ZrO_2}) + x({}^{0}G^{hcp}_{Al_2O_3} + G^{hcp\to\psi}_{Al_2O_3}) \\ &\quad + RT[(1-x)\ln(1-x) + x\ln x] + x(1-x)L^{\psi}_{Zr,Al:O} \end{aligned} \qquad (3.1.4.2)$$

Where ψ represents the monoclinic or hexagonal structure.

---

[6] In view of the complexity of the hexagonal and monoclinic structures of $Zr_{1-x}Al_xO_y$, we plot the dependence of the volume on the composition instead of the lattice constant as in previous sections.

The Gibbs free energies of the stable phases mono-ZrO_2 and hcp-Al_2O_3, ${}^0G_{ZrO_2}^{mono}$ and ${}^0G_{Al_2O_3}^{hcp}$, respectively, are obtained by fitting the thermodynamic data in the published literature [Barin 93] to a polynomial equation (2.2.4). The resulting polynomial coefficients *a* to *f* in Eq. (2.2.4) are listed in Table 3.1.4.III. The Gibbs free energy at 0 K is then approximately estimated from linear extrapolation of Eq. (2.2.4). The Gibbs free energy of the hypothetical hcp-Zr_3O_4 is not directly available, but it can be approximately expressed by the Gibbs free energy of the stable mono-ZrO_2 plus the lattice instability of hcp-Zr_3O_4, which has been calculated in section 3.1.4.1. The Gibbs free energy of hypothetical mono-AlO_2 is calculated in a similar way.

Table 3.1.4.III. The fitted parameters in Eq. (2.2.4).

Phase	*a* (10^5)	*b* (10^2)	*c* (10)	*d* (10^{-3})	*e* (10^5)	*f* (10^{-9})
mono-ZrO_2	-11.233	4.263	-6.965	-3.735	7.040	-4.999
hcp-Al_2O_3	-17.230	7.339	-11.319	-9.351	19.179	5.415

Next we study the mixing properties of the mono-$Zr_{1-x}Al_xO_2$ and hcp-$(Zr_{1-x}Al_x)_2O_3$ solid solutions. Taking mono-$Zr_{0.5}Al_{0.5}O_2$ as an example, we consider the reaction $8(Zr_{0.5}Al_{0.5})O_2 = 4ZrO_2+2Al_2O_3+O_2$, which applies for a sufficiently high oxygen activity at temperatures considered here. The de-mixing energy of mono-$Zr_{0.5}Al_{0.5}O_2$ phase with respect to the stable mono-ZrO_2, hcp-Al_2O_3 and pure O_2 is about 42.56 kJ/mol·atom, showing a high instability of the mono-$Zr_{0.5}Al_{0.5}O_2$ phase. In a similar way we calculate the de-mixing energy of the hcp-$(Zr_{0.5}Al_{0.5})_2O_3$ solid solution of 90.41 kJ/mol·atom by considering the reaction[7] $4(Zr_{0.5}Al_{0.5})_2O_3+O_2 = 4ZrO_2+2Al_2O_3$. Both the calculated values show that there is a large thermodynamic driving force for ternary $Zr_{1-x}Al_xO_y$ solution phase to segregate into the stable mono-ZrO_2 and hcp-Al_2O_3.

In order to determine the mixing properties of the $(Zr_{1-x}Al_x)O_y$ solid solution with respect to the isostructural terminal phases, we have to calculate the interaction parameters $L_{Zr,Al:O}^{mono}$ and $L_{Zr,Al:O}^{hcp}$ at 0 K. The isostructural mono-ZrO_2 and mono-AlO_2 were chosen as the terminal phases for the mono-$(Zr_{1-x}Al_x)O_2$, and the isostructural hcp-Zr_2O_3 and hcp-Al_2O_3 were chosen as the terminal phases for the hcp-$(Zr_{1-x}Al_x)_2O_3$. As outlined in section 2.4, the interaction parameters for the phases with a structure ψ can be obtained from Eq. (3.1.4.2)

$$E^{\psi}_{Zr_{1-x}Al_xO_y} - (1-x)E^{\psi}_{ZrO_y} - xE^{\psi}_{AlO_y} = x(1-x)L^{\psi}_{Zr,Al:O} \tag{3.1.4.2}$$

The composition dependence of the interaction parameter $L^{\psi}_{Zr,Al:O}$ is approximated by the polynomial $({}^0L^{\psi}_{Zr,Al:O} + {}^1L^{\psi}_{Zr,Al:O} \cdot x + {}^2L^{\psi}_{Zr,Al:O} \cdot x^2 + {}^3L^{\psi}_{Zr,Al:O} \cdot x^3)$, where ${}^0L^{\psi}_{Zr,Al:O}$, ${}^1L^{\psi}_{Zr,Al:O}$, ${}^2L^{\psi}_{Zr,Al:O}$ and ${}^3L^{\psi}_{Zr,Al:O}$ are the composition dependent parameters.

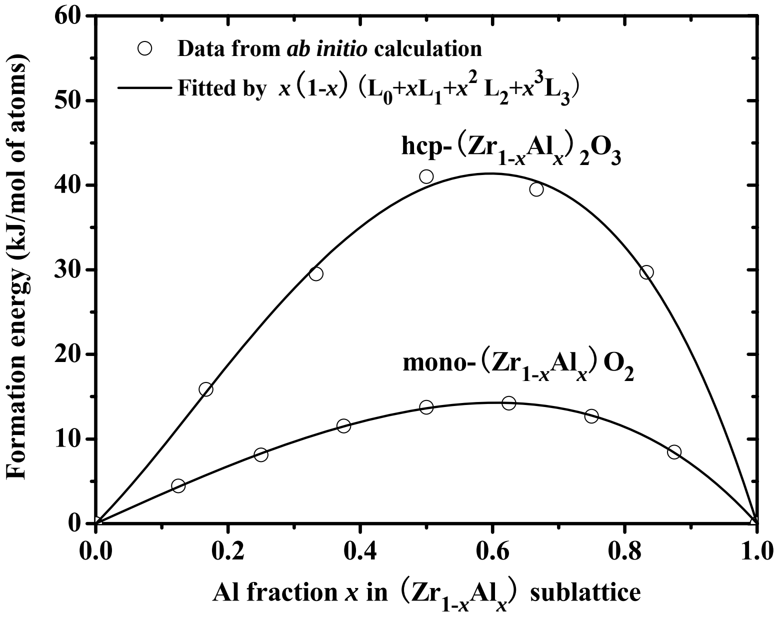

Fig. 3.1.4.3: Fit (curves) of the formation energies calculated by *ab initio* DFT (circles) with the function $x(1-x)(L_0 + xL_1 + x^2L_2 + x^3L_3)$.

Figure 3.1.4.3 shows the fit of the formation energies, with the function $x(1-x)(L_0 + xL_1 + x^2L_2 + x^3L_3)$. The circles are the data points obtained from *ab initio* calculations, and the lines in the figure show the fitted curves. The resulting composition dependent relationships are

$$L^{mono}_{Zr,Al:O} = (35.59 + 33.02 \cdot x + 1.49 \cdot x^2 + 16.39 \cdot x^3) \cdot 10^3 \text{ and}$$

$$L^{hcp}_{Zr,Al:O} = (77.85 + 236.01 \cdot x - 231.83 \cdot x^2 + 168.23 \cdot x^3) \cdot 10^3$$

J/mol·atom for mono- and hcp- $Zr_{1-x}Al_xO_y$, respectively. In both cases the formation energies are positive. Therefore, the solid solution phases are unstable and have to decompose into the isostructural terminal phases, which, as it will be discussed later, can then transform to their stable phases

We shall now study the effect of the choice of temperature independent, linear and exponential dependence of the interaction parameter on temperature following the procedure outlined in the foregoing section. This dependence is obtained from the calculated value of interaction parameter at 0 K and at another, higher temperature. According to the previous studies, there is relatively small effect of the choice between 20 and 50 kJ/mol for the interaction parameter close to the melting point on the final results. Therefore in the present work, we use only the value of 20 kJ/mol (or 10 kJ/mol·atoms) for ZrO_y-AlO_y system at its eutectic temperature of 2140 K [Jerebtsov et al. 00]. Accordingly, the linear temperature dependence of about -22.2 J/mol·K and -55.4 J/mol·K have been obtained for mono- and hcp-$Zr_{1-x}Al_xO_y$, respectively. The exponential dependence of interaction parameter on temperature has been estimated in the same way as outlined in the foregoing section for the Zr-Si-N system (see Eq. (3.1.2.3)). Accordingly, the temperature dependences of $L = (7.7847 \cdot 10^4) \cdot e^{\frac{-T}{775}}$ and $L = (3.5586 \cdot 10^4) \cdot e^{\frac{-T}{1272}}$ (J/mol·atom) have been obtained for hcp- and mono-$Zr_{1-x}Al_xO_y$ phases, respectively.

Using the values of the Gibbs free energies of the stable mono-ZrO_2 and hcp-Al_2O_3, the calculated lattice instabilities of hypothetical hcp-Zr_2O_3 and mono-AlO_2 phases, and the composition and temperature dependence of the interaction parameters, the Gibbs free energy of the mixed ternary $Zr_{1-x}Al_xO_y$ phases at different temperatures has been calculated from Eq. (2.2.3) over the entire compositions. For comparison, the results for Gibbs free energy of the formation of mono- and hcp- $Zr_{1-x}Al_xO_y$ at different temperatures of 0 K, 273 K, 573 K, 773 K, 1073 K, 1273 K with stoichiometric mono-ZrO_2 and hcp-Al_2O_3 chosen as reference states, calculated with temperature independent, linearly and exponentially temperature dependent interaction parameter are shown in Fig. 3.1.4.4. From Fig. (a) it can be seen that at the temperature of 273 K the monoclinic solid solution is more stable within the composition range of $0 \leq x \leq 0.775$, whereas the hcp solid solution becomes more stable at higher Al fraction. With increasing temperature, there is no any significant change of the composition of the cross-over points. In Fig. (b), it is seen that with increasing temperature the cross-over point moves slightly to a lower Al fraction with the values of 0.775 at 0 K and 0.705 at 1273 K. For the case of exponential dependence in Fig. (c), the cross-over values show a stronger dependence on the temperature with the values of 0.775 at 0 K and 0.643 at 1273 K. The cross-over points correspond approximately to the "optimum" Al content where the maximum hardness is expected in nc-Al_2O_3/ZrO_2 nanocomposites if they will be deposited under the conditions that enable the formation of fully segregated stoichiometric phases.

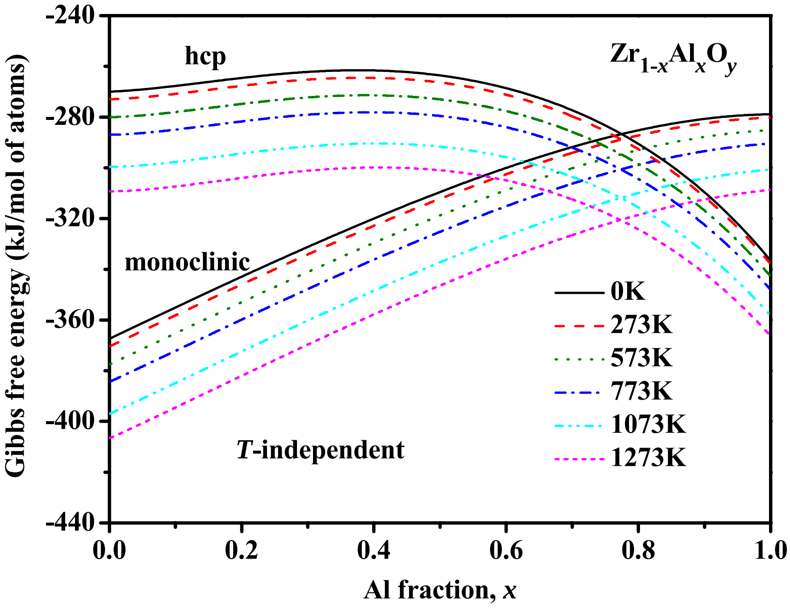

(a)

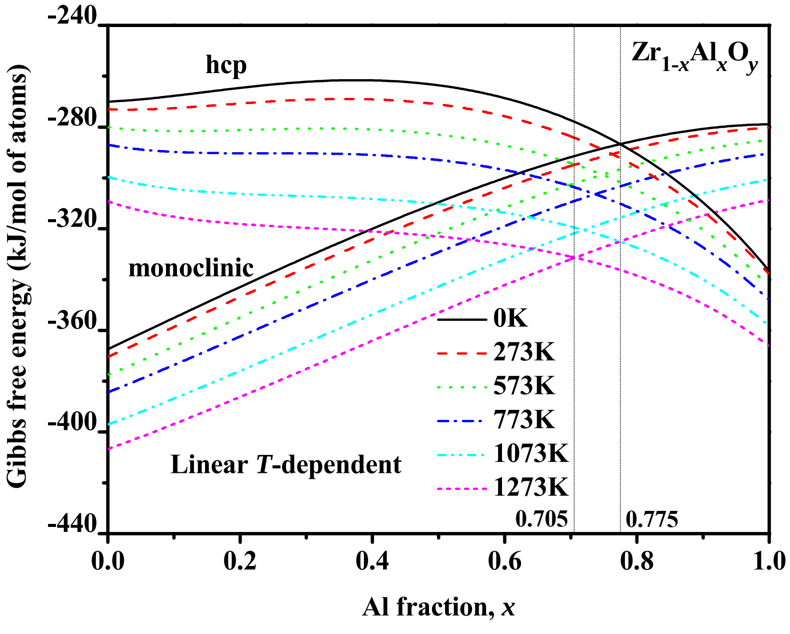

(b)

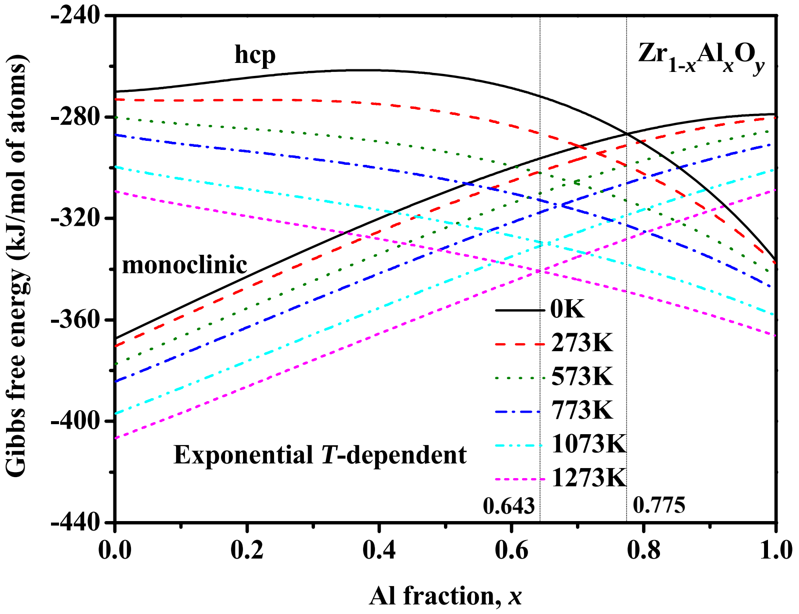

(c)

Fig. 3.1.4.4: Gibbs free energy of the formation of mono- and hcp-$Zr_{1-x}Al_xO_y$ at different temperatures of 0 K, 273 K, 573 K, 773 K, 1073 K and 1273 K with stoichiometric mono-ZrO_2 and hcp-Al_2O_3 chosen as reference states calculated with (a) temperature independent, (b) linearly and (c) exponentially temperature dependent interaction parameter.

3.1.4.3 Possibility of chemical and coherent spinodal decomposition

Figure 3.1.4.5 shows the Gibbs free energy of mixing for the mono-$Zr_{1-x}Al_xO_2$ solid solution as a function of AlO_2 fraction for temperatures 0 K, 273 K, 573 K, 773 K, 1073 K, 1273 K and nitrogen pressure of 1 atm, with isostructural, stoichiometric mono-ZrO_2 and mono-AlO_2 as the reference states, calculated with temperature independent, (Fig. (a)), linearly (Fig. (b)) and exponentially (Fig. (c)) temperature dependent interaction parameter. It is seen that for the case of temperature independent interaction parameter in Fig. (a), the Gibbs free energy of mixing changes only little with increasing temperature from 0 K to 1273 K. Comparing the linear (Fig. (b)) and exponential (Fig. (c)) temperature dependence one sees that with increasing temperature, the maximum of the Gibbs free energy of mixing decreases with increasing temperature for both cases. However, the decrease is faster for the exponential dependence than for the linear one. Moreover, the immiscibility gap with $\frac{\delta^2 G_f^0(x)}{\delta x^2} < 0$ is somewhat larger for the exponential temperature dependence, particularly in the range of low AlO_2 fraction. Furthermore, the position of the maximum of the Gibbs free energy as function of the AlO_2 fraction changes less for the exponential case.

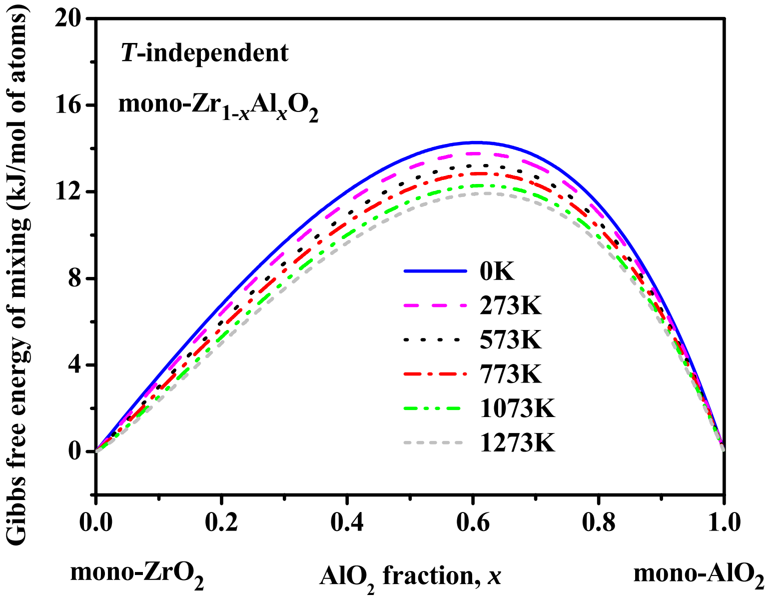

(a)

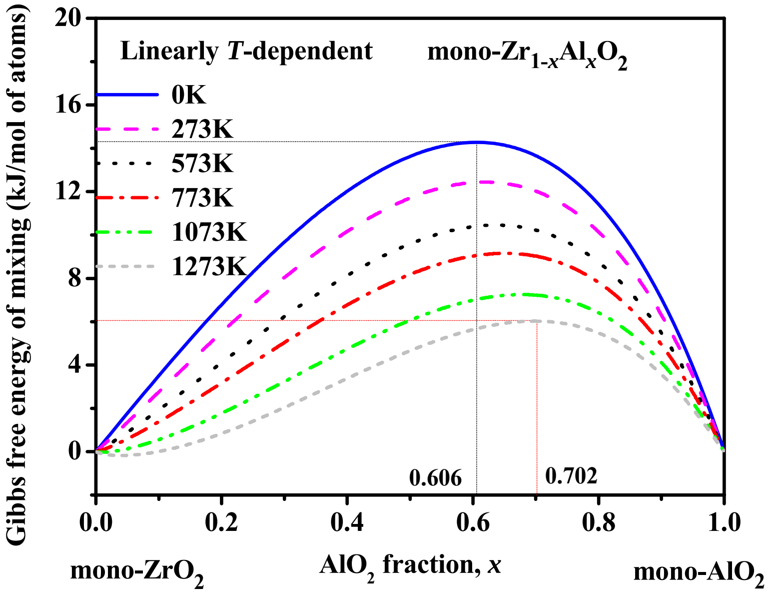

(b)

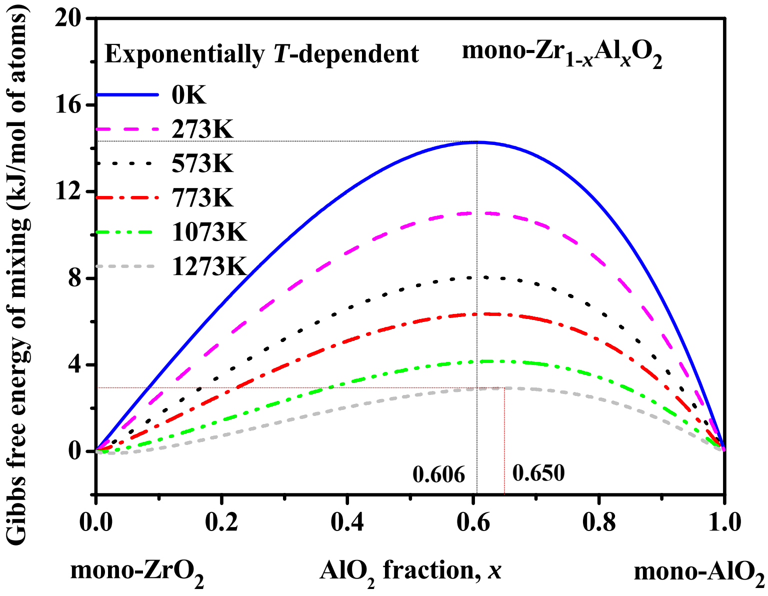

(c)

Fig. 3.1.4.5: Gibbs free energy of mixing of mono-$Zr_{1-x}Al_xO_2$ phase as a function of AlO_2 fraction for temperatures 0 K, 273 K, 573 K, 773 K, 1073 K and 1273 K, with isostructural mono-ZrO_2 and mono-AlO_2 as reference states, calculated with (a) temperature independent, (b) linearly and (c) exponentially temperature dependent interaction parameter.

Next we discuss the Gibbs free energy of mixing of the hcp-$(Zr_{1-x}Al_x)_2O_3$ solid solution with the isostructural hcp-Zr_2O_3 and hcp-Al_2O_3 phases chosen as the reference states. The results are shown in Fig. 3.1.4.6. Comparing these results with Fig. 3.1.4.5 we see similar trends for the different temperature dependences of the interaction parameters. However, the maximum de-mixing energies are higher for hcp-$Zr_{1-x}Al_xO_y$ than that for mono-$Zr_{1-x}Al_xO_y$.

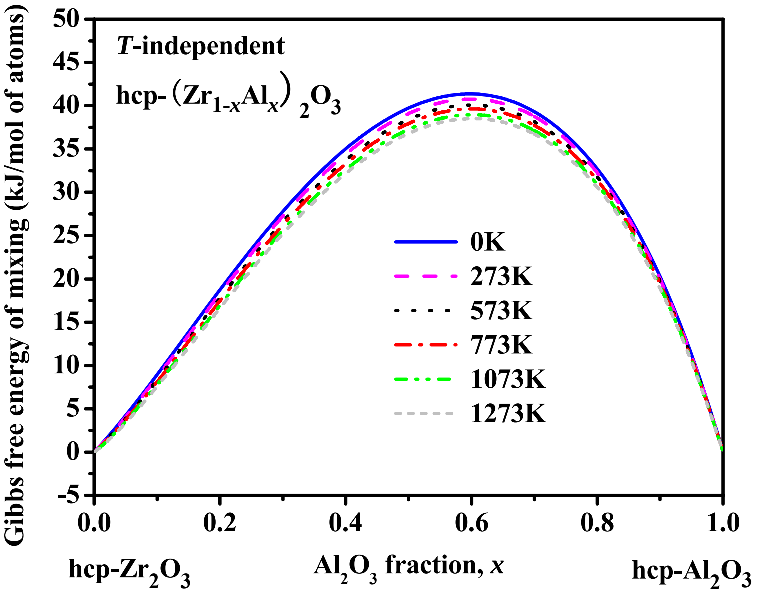
T-independent
hcp-$(Zr_{1-x}Al_x)_2O_3$
0K
273K
573K
773K
1073K
1273K
Gibbs free energy of mixing (kJ/mol of atoms)
50
45
40
35
30
25
20
15
10
5
0
-5
0.0
0.2
0.4
0.6
0.8
1.0
hcp-Zr_2O_3
Al_2O_3 fraction, *x*
hcp-Al_2O_3

(a)

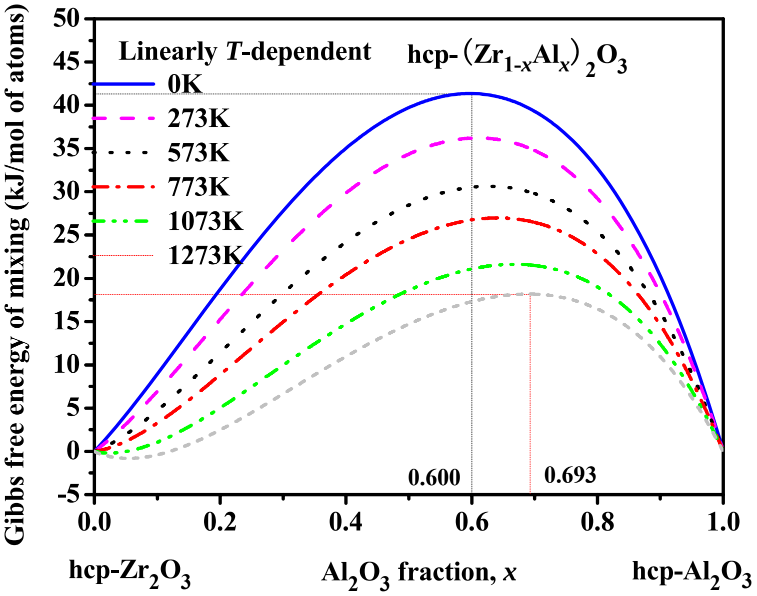
Linearly *T*-dependent
hcp-$(Zr_{1-x}Al_x)_2O_3$
0K
273K
573K
773K
1073K
1273K
0.600
0.693
Gibbs free energy of mixing (kJ/mol of atoms)
50
45
40
35
30
25
20
15
10
5
0
-5
0.0
0.2
0.4
0.6
0.8
1.0
hcp-Zr_2O_3
Al_2O_3 fraction, *x*
hcp-Al_2O_3

(b)

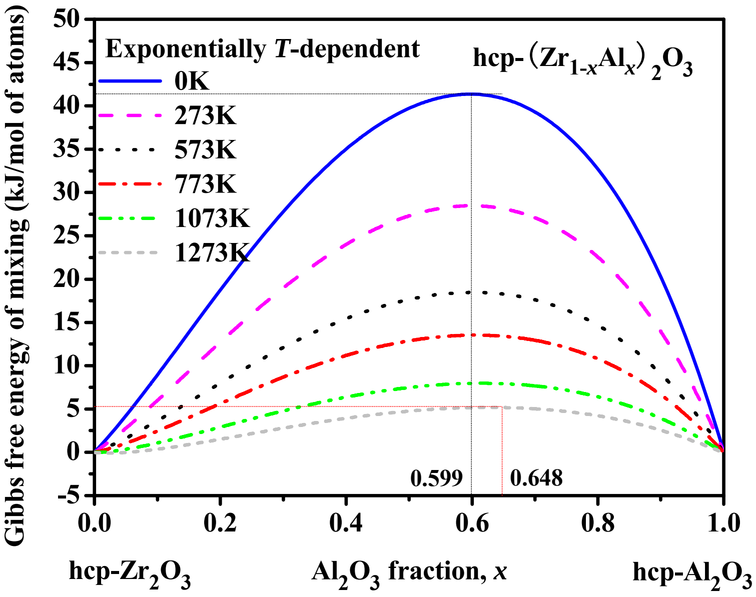

(c)

Fig. 3.1.4.6: Gibbs free energy of mixing of hcp-$(Zr_{1-x}Al_x)_2O_3$ phase as a function of Al_2O_3 fraction for temperatures 0 K, 273 K, 573 K, 773 K, 1073 K and 1273 K, with isostructural hcp-Zr_2O_3 and hcp-Al_2O_3 as reference states, calculated with (a) temperature independent, (b) linearly and (c) exponentially temperature dependent interaction parameter.

Figure 3.1.4.7 shows the phase stability diagrams of mono-$(Zr_{1-x}Al_x)O_2$ as a function of AlO_2 fraction x with mono-ZrO_2 and mono-AlO_2 as reference states calculated with (a) temperature independent, (b) linearly, and (c) exponentially temperature dependent interaction parameter. It can be seen from Fig. (a) that assuming the temperature independent interaction parameter, as it has been done in several recent papers of other groups, yields unreasonably high spinodal temperature. Therefore, this case will not be further discussed here. In the case of linear dependence, the spinodal temperature is much lower, but its maximum is still higher than the melting points of the oxides (2327 K for α-Al_2O_3 and 2950 K for ZrO_2). Therefore we concentrate on the case of the exponential dependence of the interaction parameter shown in Fig. (c). For the convenience of the reader we repeat that the chemical spinodal curve corresponds to the dependence of Gibbs free energy on the composition where $\frac{\delta^2 G_f^0(x)}{\delta x^2} < 0$, i.e., the thermodynamically driven phase segregation occurs without any activation, whereas between the spinodal and binodal curves it occurs by activated nucleation and growth because

$\frac{\delta^2 G_f^0(x)}{\delta x^2} > 0$. From Fig. (c) we conclude that, for a typical deposition (773 K) and aging (1073 K) temperature, the system is chemically spinodal within almost the whole composition range, in particular for the compositions of about x = 0.2-0.8 corresponding to the formation of the nanocomposites. Even when the system, starting the decomposition from the spinodal region is approaching, within the incompletely segregated volumes, the terminal phases where nucleation and growth might be theoretically possible (e.g., for $x < 0.1$), the mechanism of nucleation and growth will not operate because of a sufficiently high density of the segregated grains and low supersaturation. Therefore, the mechanism of nucleation and growth can be neglected. The de-mixing energies presented in Fig. (c) might appear relatively small for coherent spinodal to occur, because the elastic misfit energy is relatively high. However, one has to consider the high instability of the mono-AlO_2 terminal phase of 57.65 kJ/mol·atom as compared with the thermodynamically stable hcp-Al_2O_3 one. Therefore, the phase transformation 2mono-AlO_2 → hcp Al_2O_3 + (1/2)O_2 during the later stage of the decomposition of the mono-$Zr_{1-x}Al_xO_2$ solution will not hinder the decomposition into stoichiometric ZrO_2 and Al_2O_3 to be completed. This is an extension of the conventional concept of the spinodal decomposition developed originally for metallic system with a much smaller de-mixing energy than the oxide under consideration. Because of the high de-mixing energy of the mono-$Zr_{1-x}Al_xO_2$ solid solution, spinodal decomposition will occur within the whole composition range which is relevant for the formation of the nanocomposites.

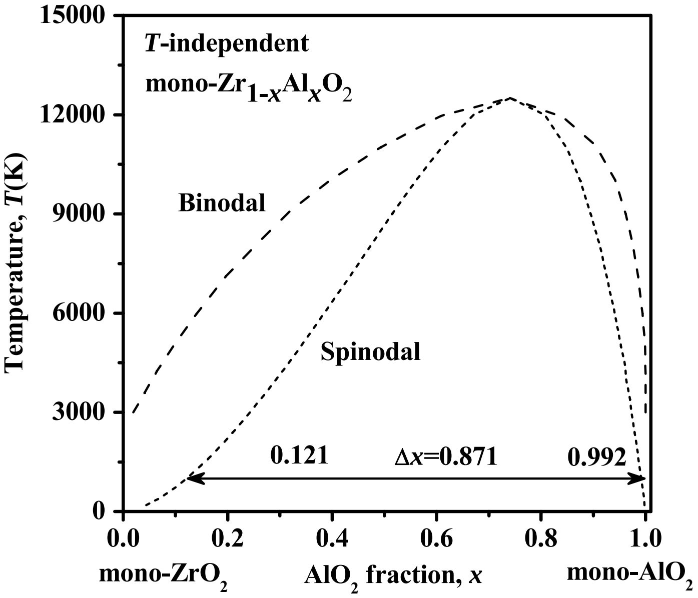

(a)

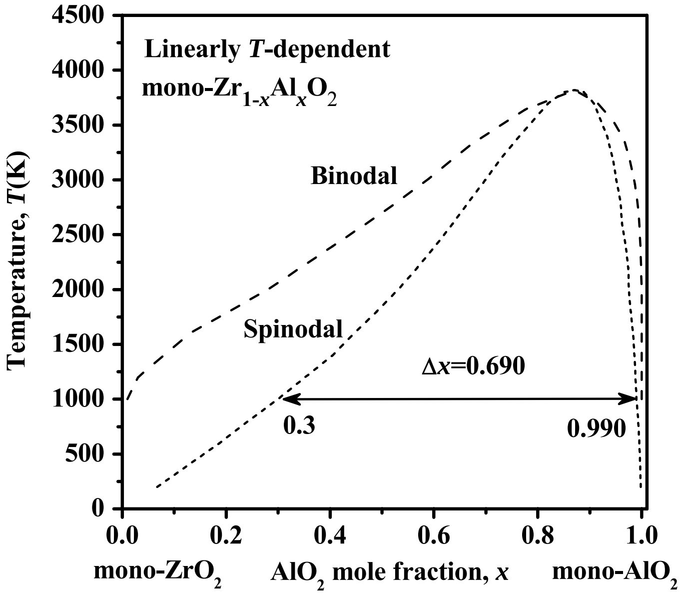

(b)

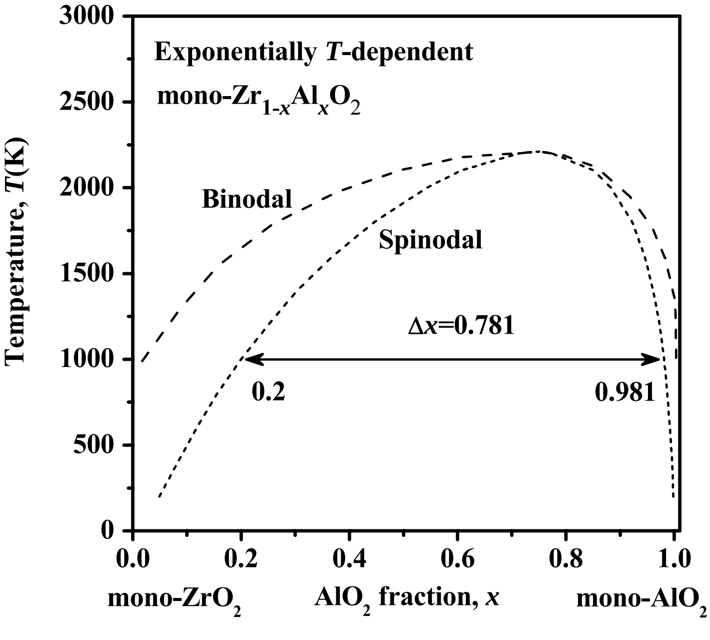

(c)

Fig. 3.1.4.7: Temperature-composition phase diagram for mono-$Zr_{1-x}Al_xO_2$ showing the spinodal (short dashed line) and binodal (dashed lines) curves with mono-ZrO_2 and mono-AlO_2 chosen as reference states calculated with (a) temperature independent, (b) linearly and (c) exponentially temperature dependent interaction parameter.

Finally, we shall discuss the phase stability of hcp-$(Zr_{1-x}Al_x)_2O_3$ solid solution. Figure 3.1.4.8 shows the phase stability diagram of hcp-$(Zr_{1-x}Al_x)_2O_3$ solid solution as function of the composition calculated by the three different temperature dependences of the interaction parameters discussed above. As for the case of the hexagonal structure, neglecting the temperature dependence yields physically unreasonable results. Also the linear dependence yields too high temperature above the melting points of both terminal phases. Therefore, we concentrate on Fig. (c), which shows the results when assuming the exponential temperature dependence of the interaction parameter. Accordingly, the chemical spinodal decomposition occurs in a large composition range from 0.197 to 0.988 at the temperature of 1000 K. The obtained maximum temperature of 2045 K for spinodal decomposition is quite reasonable. The spinodal range is somewhat smaller at the side of hcp-Zr_2O_3 as compared with the mono-ZrO_2 in Fig. 3.1.4.7 (c) because the latter is the stable whereas the hcp-Zr_2O_3 is the unstable terminal phase.

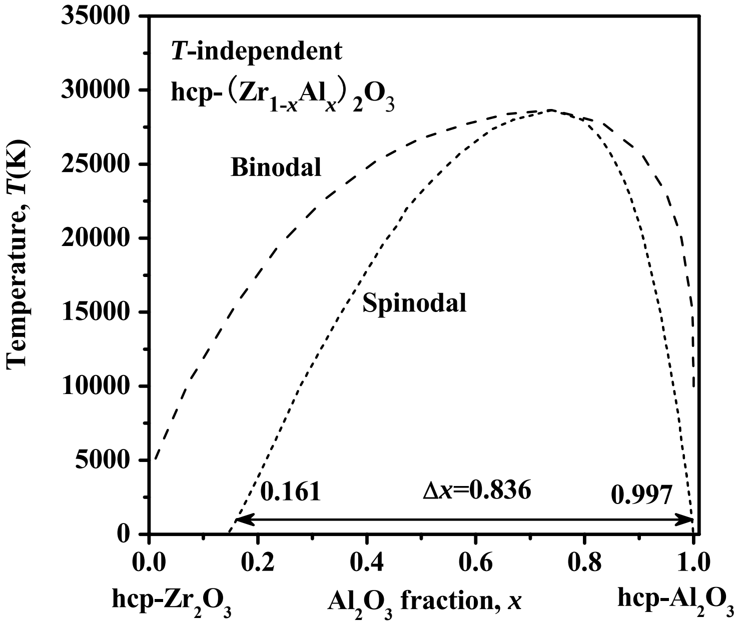

(a)

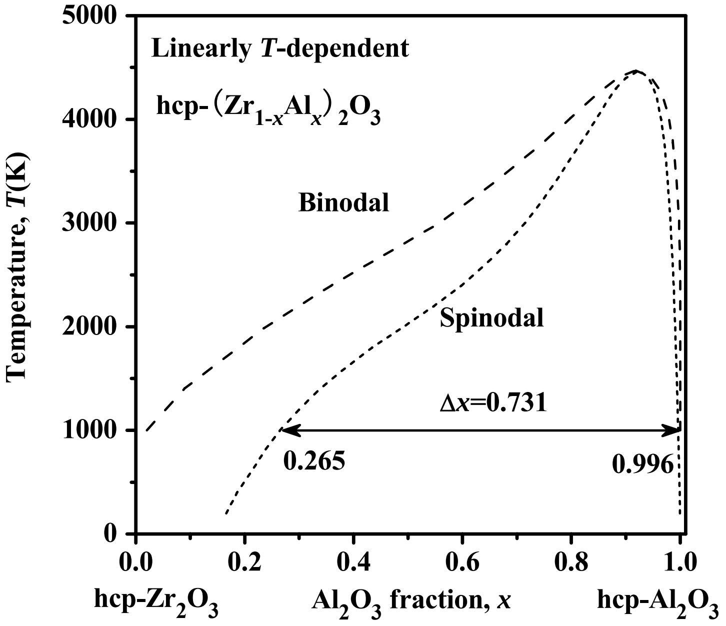

(b)

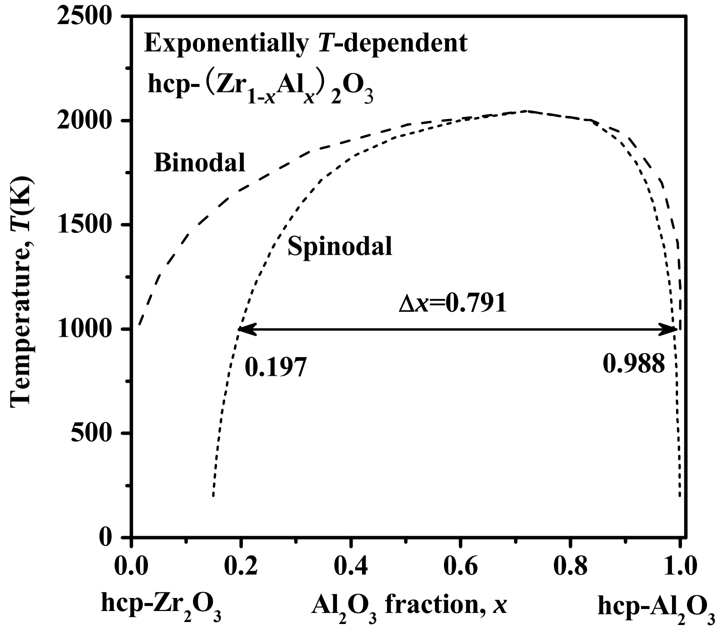

(c)

Fig. 3.1.4.8: Temperature-composition phase diagram for hcp-$(Zr_{1-x}Al_x)_2O_3$ showing the spinodal (short dashed line) and binodal (dashed lines) curves with hcp-Zr_2O_3 and hcp-Al_2O_3 as reference states calculated with (a) temperature independent, (b) linearly and (c) exponentially temperature dependent interaction parameter.

3.1.4.4 Summary

The internal structure parameters of the stable mono-ZrO_2 and hcp-Al_2O_3 phases were first optimized by *ab initio* DFT calculation, and then used for the calculation of the equilibrium properties, such as the total energy, volume, bulk modulus, and its derivative. The obtained results agree well with the published theoretical and experimental data. Therefore, the *ab initio* DFT calculations were extended to determine the relative stabilities of hypothetical, unstable binary hcp-Zr_2O_3 and mono-AlO_2 and their ternary $Zr_{1-x}Al_xO_y$ solid solution counterparts. Because of the smaller atomic radius of Al as compared with that of Zr, the calculated molar volume decreases with increasing Al fraction in the $(Zr_{1-x}Al_x)$ sublattice.

Two polynomials with four parameters have been obtained by fitting the composition dependence of the interaction parameter for mono- and hcp-$Zr_{1-x}Al_xO_y$ phases, that has been calculated by the *ab initio* DFT method. For the temperature dependence of the interaction parameter, three cases have been considered: temperature independent, linearly and exponentially temperature dependent. These dependences were then used for the calculation of the Gibbs free energy of mixing for both hcp- and mono-$Zr_{1-x}Al_xO_y$ phases, as well as for the calculation of the spinodal and binodal diagrams as function of composition. It is found that using the temperature independent interaction parameter, as done in many recent papers of other groups, yields unreasonable results. With a linearly dependent interaction parameter, the proportionality factors of -22.2 J/mol·K and -55.4 J/mol·K are obtained for mono- and hcp- $Zr_{1-x}Al_xO_y$ phases, respectively. However, the maximum spinodal temperature was above the melting points of the terminal binary oxides and, therefore still too high. The most reliable results were obtained with the exponential temperature dependences of $L = (7.7847 \cdot 10^4) \cdot e^{\frac{-T}{775}}$ and $L = (3.5586 \cdot 10^4) \cdot e^{\frac{-T}{1272}}$ for the hcp- and mono- $Zr_{1-x}Al_xO_y$ phases, respectively.

With the exponential dependence we calculated the Gibbs free energy of the mixed solid solution, as well as the spinodal and binodal curves as function of the composition for both monoclinic and hexagonal $Zr_{1-x}Al_xO_y$ solid solution. The results clearly show that the system should undergo spinodal phase segregation within the composition range that is relevant for the formation of superhard nanocomposites, provided the deposition temperature is sufficiently high in order to assure fast diffusion, which kinetically controls the segregation. These results provide guideline for more precise experimental work to be done in the future, particularly as regards the deposition temperature and partial pressure of oxygen during the deposition.

3.2 Strengthening mechanism in the ZrAlN system

In this section, we shall calculate the ideal strengths of the fcc-$Zr_{1-x}Al_xN$ solid solution with different Al content and compare it with terminal binary phases fcc(NaCl)-ZrN and fcc(NaCl)-AlN. The ideal strengths of the stable hcp-AlN reported recently by Zhang et al. [Zhang et al. 07b] will be considered as well. The results will be then used for the comparison with the ideal strengths of a ZrN/1 ML-AlN/ZrN and AlN/1 ML-ZrN/AlN sandwich.

3.2.1 $Zr_{1-x}Al_xN$ solid solutions

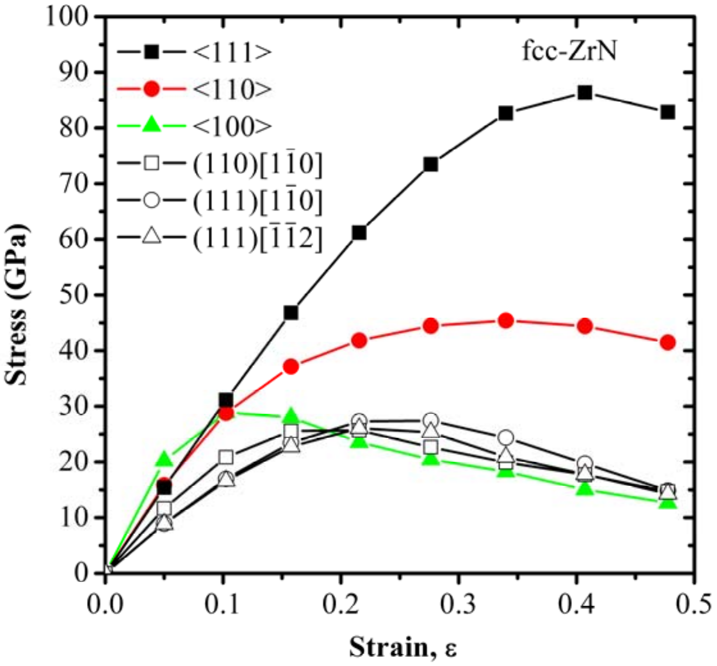

Fig. 3.2.1. Stress – strain relationships calculated by *ab initio* DFT method for fcc(NaCl)-ZrN.

The ideal de-cohesion strengths for the fcc-ZrN, fcc-AlN and three fcc-$Zr_{1-x}Al_xN$ solid solution with $x = 0.25$, 0.50 and 0.75 were calculated in three main crystal directions <100>, <110> and <111> through a projection of 8 atoms unit cell onto three Cartesian coordinate axes with one axis parallel to the direction of the strain. For the calculation of the shear deformation, one of the axes was chosen parallel to slip direction and another one was perpendicular to the slip plane. The selected slip systems were $(111)[1\bar{1}0]$, $(111)[\bar{1}\bar{1}2]$ and $(110)[1\bar{1}0]$.

Figure 3.2.1 shows the stress – strain curves calculated for fcc-ZrN. The anisotropy ratio of the ideal de-cohesion strengths of fcc-ZrN is $\sigma_{<111>}$= 86.4 GPa : $\sigma_{<110>}$= 45.4 GPa : $\sigma_{<100>}$=

28.9 GPa = 2.99: 1.57: 1. The ideal shear strengths of fcc-ZrN is 27.4 GPa for the $(111)[1\bar{1}0]$, 26.1 GPa for the $(111)[\bar{1}\bar{1}2]$, and 25.7 GPa for the $(110)[1\bar{1}0]$ slip system.

Figure 3.2.2(a) shows the stress – strain curves calculated for fcc-AlN. The anisotropy ratio of the ideal de-cohesion strengths of $\sigma_{<111>}$= 102.6 GPa : $\sigma_{<110>}$= 45.2 GPa : $\sigma_{<100>}$= 20.7 GPa = 4.96: 2.18: 1 is larger than that of fcc-ZrN shown in Fig. 3.2.1. However, the calculated lowest decohesion strength of 20.7 GPa of fcc-AlN is lower than that of fcc-ZrN of 28.9 GPa. The ideal shear strengths of fcc-AlN is 22.2 GPa for the $(111)[1\bar{1}0]$, 19.4 GPa for the $(111)[\bar{1}\bar{1}2]$, and 18.7 GPa for the $(110)[1\bar{1}0]$ slip system. It is found that the ideal shear resistance of the fcc-AlN of 18 to 22 GPa is also smaller than that of the fcc-ZrN of 25 to 27 GPa.

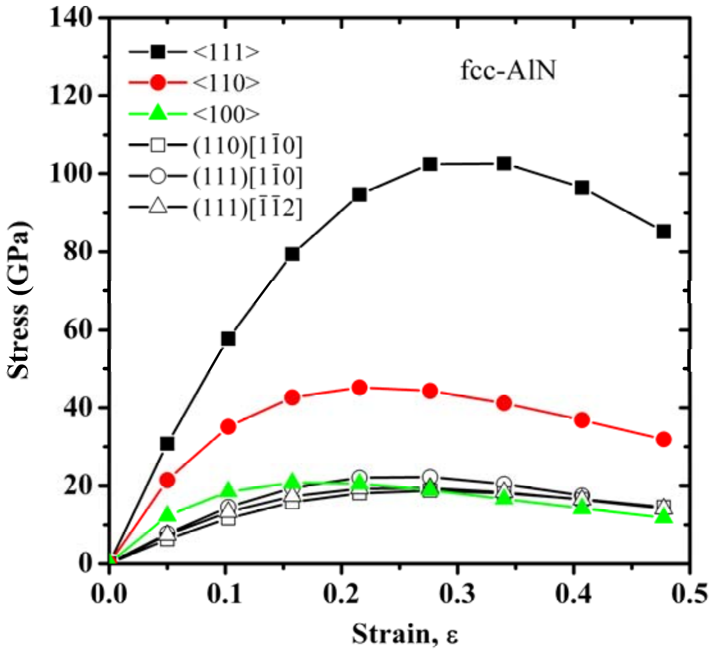

Fig. 3.2.2 (a). Calculated stress – strain relationships for fcc(NaCl)-AlN.

Figure 3.2.2(b) shows the stress – strain curves calculated for hcp-AlN by Zhang et al. [Zhang et al. 07b]. The anisotropy of the ideal de-cohesion strength is smaller, but the de-cohesion strength larger than the weakest one in the <100> direction of the fcc-AlN. The ideal shear strength compares with that of the fcc-AlN, and it is only slightly smaller than that of fcc-ZrN.

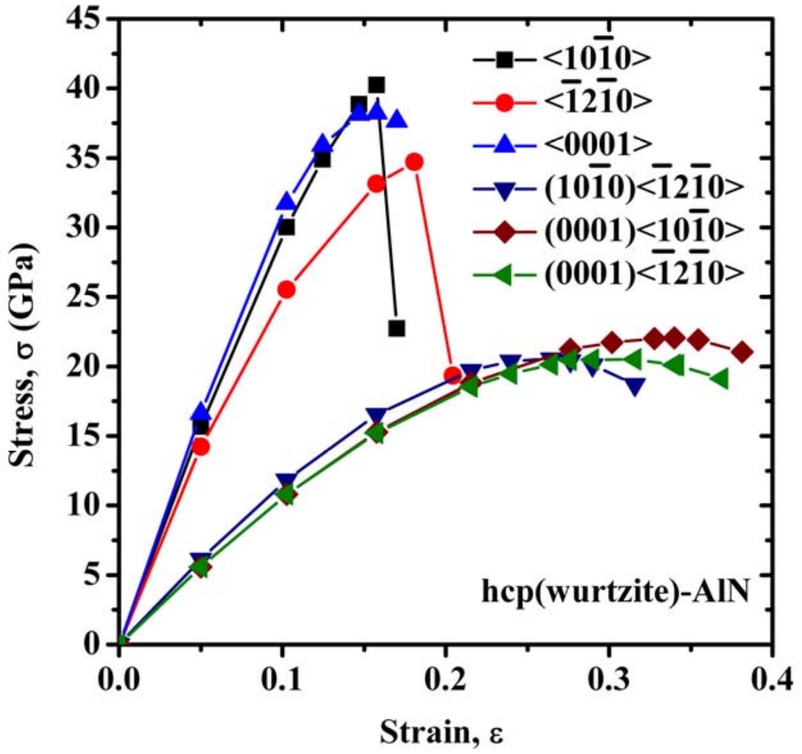

Fig. 3.2.2 (b): Calculated stress – strain relationships for hcp-AlN (from [Zhang et al. 07b]).

Figure 3.2.3 shows the stress – strain curves calculated for fcc-Zr$_{1-x}$Al$_x$N solid solution with $x = 0.75, 0.50, 0.25$. Except for a small decrease of the de-cohesion strength in the <111> direction, there is relatively small difference between the solid solution and the terminal binary phases fcc-ZrN and fcc-AlN. With the increase of the Al content, the ideal shear strengths decreases from about 25.7 GPa for pure fcc-ZrN to 18.2 GPa for the weakest (111) [$\bar{1}\bar{1}2$] slip system of Zr$_{0.5}$Al$_{0.5}$N, followed by a slight increase to 19.5 GPa for Zr$_{0.25}$Al$_{0.75}$N when compares with the calculated shear strength of fcc-AlN.

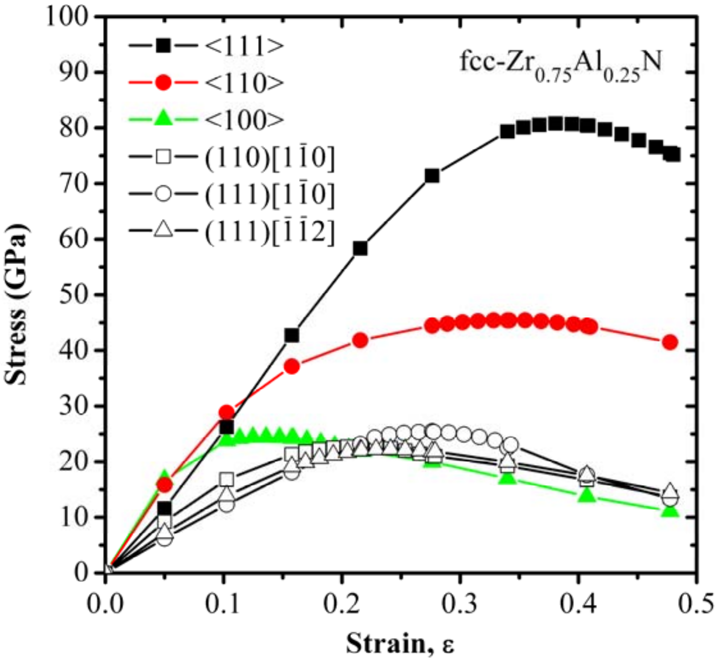

fcc-$Zr_{0.75}Al_{0.25}N$
<111>
<110>
<100>
$(110)[1\bar{1}0]$
$(111)[1\bar{1}0]$
$(111)[\bar{1}\bar{1}2]$
Stress (GPa)
Strain, ε
0
10
20
30
40
50
60
70
80
90
100
0.0
0.1
0.2
0.3
0.4
0.5

(a)

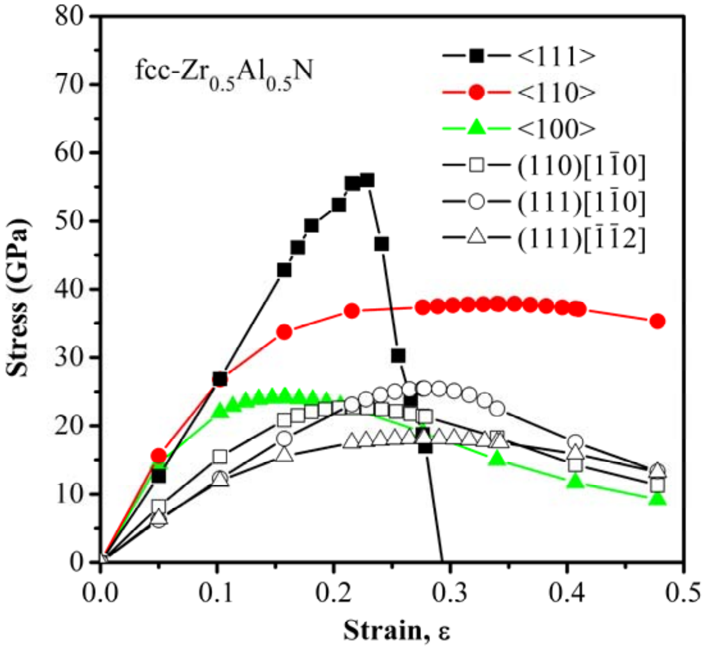

fcc-$Zr_{0.5}Al_{0.5}N$
<111>
<110>
<100>
$(110)[1\bar{1}0]$
$(111)[1\bar{1}0]$
$(111)[\bar{1}\bar{1}2]$
Stress (GPa)
Strain, ε
0
10
20
30
40
50
60
70
80
0.0
0.1
0.2
0.3
0.4
0.5

(b)

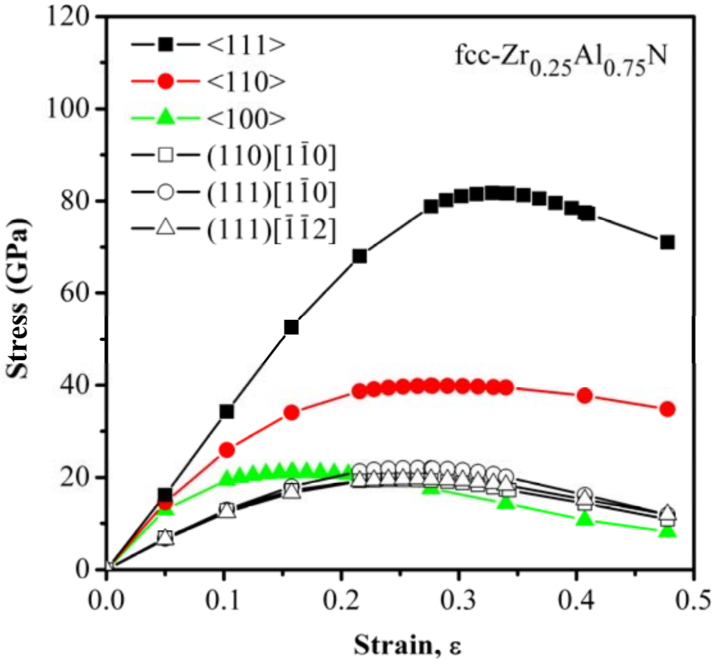

(c)

Fig. 3.2.3: Calculated stress – strain relationships for fcc(NaCl)- $Zr_{1-x}Al_xN$ solid solutions (a) $x = 0.75$, (b) $x = 0.50$ and (c) $x = 0.25$.

Table 3.2.I summarizes the maximum ideal de-cohesion strengths in the <100>, <110> and <111> directions, and the maximum ideal shear strengths in the $(110)[1\bar{1}0]$, $(111)[1\bar{1}0]$ and $(111)[\bar{1}\bar{1}2]$ slip systems for the fcc- AlN, ZrN and $Zr_{1-x}Al_xN$ with $x = 0.25, 0.5, 0.75$. One can see that:

1. The de-cohesion strength is the highest in the <111> direction for all the phases.
2. The ideal shear strength is the highest in the $(111)[1\bar{1}0]$ slip system for all phases.
3. Substitution of Al for Zr in ZrN results in a slight decrease of ideal de-cohesion and shear strength.
4. The lowest shear strength shows in the $(111)[\bar{1}\bar{1}2]$ slip system of the $Zr_{0.5}Al_{0.5}N$ solid solution.

Table 3.2.I: The maximum tensile strengths under the <100>, <110> and <111> tensile stress, respectively, and shear strengths under $(110)[1\bar{1}0]$, $(111)[1\bar{1}0]$, and $(111)[\bar{1}\bar{1}2]$ shear stress, respectively, of AlN, ZrN and $Zr_{1-x}Al_xN$ (x=0.25, 0.5, 0.75) in fcc(NaCl) structure calculated by *ab initio* DFT calculation.

Phase	Tensile strength			Shear strength		
	<100>	<110>	<111>	$(110)[1\bar{1}0]$	$(111)[1\bar{1}0]$	$(111)[\bar{1}\bar{1}2]$
fcc-ZrN	28.91	45.41	86.39	25.68	27.41	26.06
fcc-AlN	20.74	45.15	102.61	18.74	22.17	19.39
fcc-$Zr_{0.75}Al_{0.25}N$	24.43	45.44	80.80	22.81	25.49	22.24
fcc-$Zr_{0.5}Al_{0.5}N$	24.13	37.90	55.99	22.80	25.49	18.21
fcc-$Zr_{0.25}Al_{0.75}N$	21.11	39.91	81.80	19.50	22.03	19.68

It should be noted that the experimental results show that the hardness increases from 21 GPa for pure ZrN to 28 GPa for the $Zr_{0.57}Al_{0.43}N$ solid solution [Lamni et al. 05]. This is not in any discrepancy with the calculated decrease of the ideal shear strength because the solution hardening is based on the reduction of dislocation mobility caused by the solute atoms. The exact mechanism of solution strengthening depends on many factors including among others also the type of the dislocations and the structure of the material [Argon 08]. The most important effects are the a) size misfit interaction, where the solute atoms replacing the host atom in the lattice place is of a different size, and b) the modulus misfit interaction where the solute atom changes the elastic properties of its surrounding. However, other effects can also play a role: The solute atoms may segregate to the stacking faults of the dislocations (the so called "chemical interaction"). It has been also shown, that clustering, which may occur during the deposition, can also increase the hardness by the mechanism of precipitation hardening. Because of the complexity of these mechanisms [Argon 08] and limited experimental data, more detailed discussion of the mechanism of the solution strengthening in the $Zr_{1-x}Al_xN$ solid solution is beyond the scope of this work. Our calculations just show that the reduction of the ideal strengths is modest and therefore does not hinder the solid solution strengthening of the deposited coatings which are far away from being "ideal materials".

3.2.2 The strength of the ZrN/1 ML AlN/ZrN interface in comparison with the bulk phases

In this section, we shall present the results of the calculations of the stress-strain relationships, the atomistic mechanisms and the electronic structures of instability of several ZrN/1 ML-AlN/ZrN interface, and compare them with those of the bulk phases in order to find out if a similar strengthening as in the case of the TiN/1 ML-SiN_x/TiN can be expected. We do not consider the AlN/1 ML-ZrN/AlN interface because due to a somewhat lower Pauling's electronegativity of Zr (1.4) as compared with Al (1.5) no strengthening is expected in this case. In addition, we shall also check the possible effect of the chosen thickness of the ZrN slab on the results.

3.2.2.1 The stress-strain relationships of the ZrN/1 ML-AlN/ZrN interfaces

Figure 3.2.4 shows the calculated stress–strain relationship of fcc(NaCl)-ZrN/1 ML-AlN/ZrN for different crystallographic directions and slip systems as indicated. For comparison, the de-cohesion and shear strengths and the corresponding critical strains for bulk phases reported in the foregoing section and those of the interfaces shown in Fig. 3.2.4 are summarized in Table 3.2.II. The minimum de-cohesion strength of the interface of 24.26 and 22.75 GPa is found in the <001> direction for slabs with ZrN thickness of 1.8 and 2.7 nm, respectively. The minimum shear strength of 14.7 GPa is found in the $(111)\,[\bar{1}\bar{1}2]$ slip system. Both are comparable to the smallest strengths of the bulk phases fcc-ZrN, fcc-AlN and the solid solutions $Zr_{1-x}Al_xN$. Thus, we conclude that there is no obvious strengthening of the ZrN/1 ML-AlN/ZrN slab similar to that which has been found in the TiN/1 ML-SiN_x/TiN system.

In order to check the effect of the thickness of the ZrN(001) slabs on the results of the calculations, a comparison of the calculated stress-strain curves for slab thickness of 1.8 and 2.7 nm is shown in Fig. 3.2.4(d) and the values of the ideal strengths are given in Table 3.2.II. It is seen that the stress-strain curves for two different thickness are nearly the same and the values of the ideal strength and strain differ only slightly when the thickness changes. This confirms that the results are not influenced by the thickness of the ZrN slab chosen in this range, which corresponds to the average crystallite size of 3-4 nm as found in the superhard nanocomposites prepared under the optimum conditions [Veprek et al. 05].

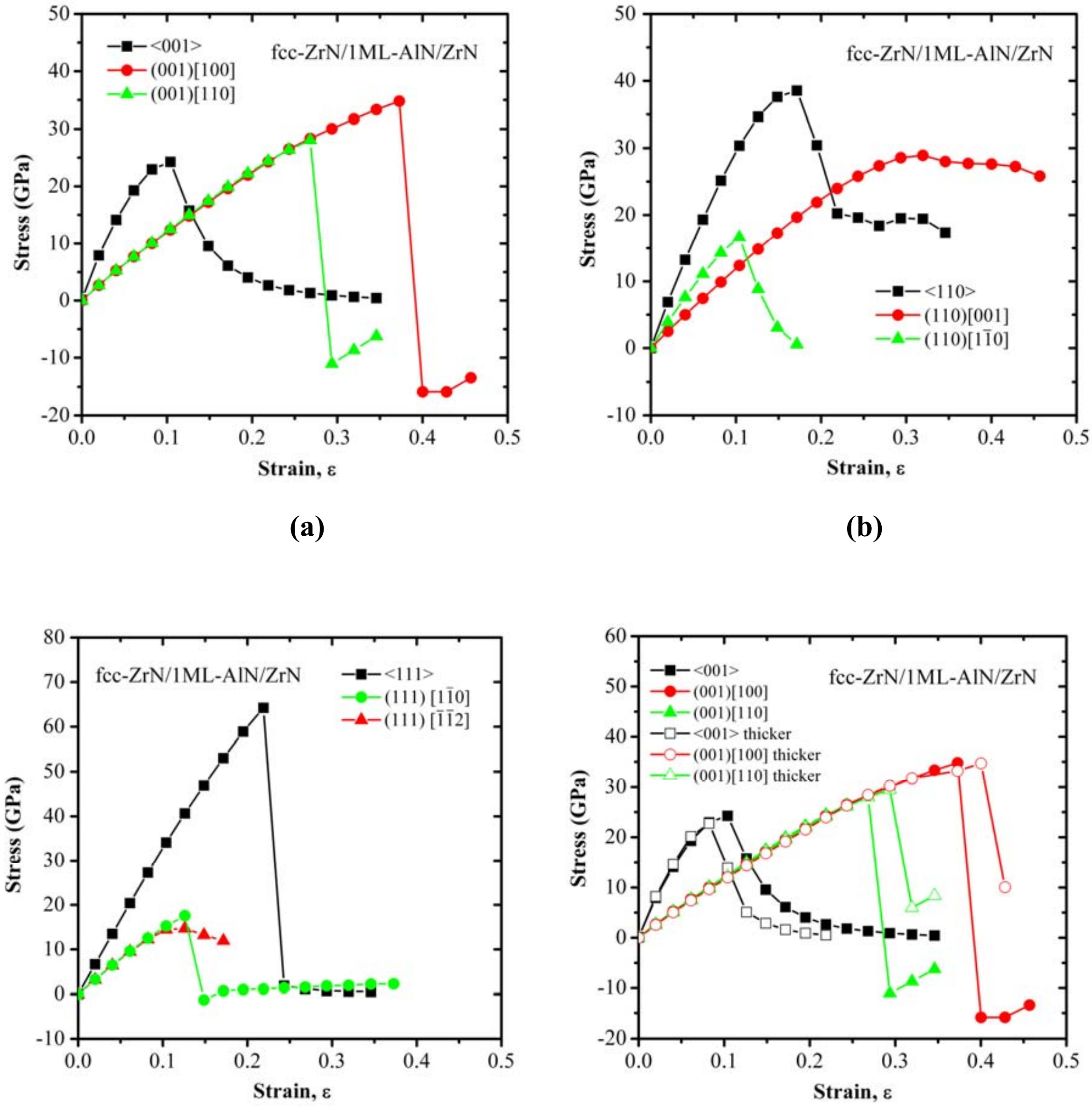

(a)

(b)

(c)

(d)

Fig. 3.2.4: Calculated stress-strain relationships for three fcc-ZrN/1 ML-AlN/ZrN interfaces in different crystallographic directions and slip systems as indicated for the (001) [Fig. (a)], (110) [Fig. (b)] and (111) [Fig. (c)] interfaces. Figure (d) shows a comparison of the stress-strain curves for (001) interface with different thickness of the ZrN slab of 1.8 nm and 2.7 nm (denoted as "thicker")**.**

Table 3.2.II: De-cohesion strengths and corresponding strains in the <001>, <110> and <111> directions and the shear strengths and strains in various slip systems of bulk fcc-ZrN, fcc-AlN and fcc(NaCl)-$Zr_{1-x}Al_xN$(x=0.25, 0.5, 0.75) in comparison with the fcc-ZrN/1 ML-AlN/ZrN interface. The strains are given in the parenthesis.

Phase	De-cohesion strength and the corresponding strain			Shear strength and the corresponding strain					
	<001>	<110>	<111>	(001)[100]	(001)[110]	(110) [001]	$(110)[1\bar{1}0]$	$(111)[1\bar{1}0]$	$(111)[\bar{1}\bar{1}2]$
fcc-ZrN	28.91	45.41	86.39				25.68	27.41	26.06
	0.1025	0.3400	0.4071				0.2155	0.2763	0.2155
fcc-AlN	20.74	45.10	102.61				18.74	22.17	19.39
	0.1576	0.2155	0.3400				0.2763	0.2763	0.2763
fcc-$Zr_{0.75}Al_{0.25}N$	24.26	42.35	80.46				22.77	25.49	22.11
	0.1576	0.3400	0.4071				0.2155	0.2763	0.2155
fcc-$Zr_{0.5}Al_{0.5}N$	24.13	37.88	55.99				22.80	25.49	18.21
	0.1576	0.3400	0.2287				0.2155	0.2763	0.2763
fcc-$Zr_{0.25}Al_{0.75}N$	21.11	39.91	81.80				19.50	22.03	19.68
	0.1704	0.2763	0.3282				0.2524	0.2649	0.2649
fcc-ZrN/1 ML-AlN/ZrN	24.26	38.54	64.23	34.79	28.07	28.93	16.65	17.58	14.70
(ZrN thickness 1.8 nm)	0.1040	0.1716	0.2189	0.3728	0.2682	0.3195	0.1040	0.1261	0.1261
fcc-ZrN/1 ML-AlN/ZrN	22.75			34.7	29.46				
(ZrN thickness 2.7 nm)	0.0824			0.4002	0.2936				

3.2.2.2 The crystal and electronic structure at equilibrium

The crystal structure and the bond length of bulk fcc-ZrN, fcc-AlN and hcp-AlN after relaxation at zero strain are shown in Fig. 3.2.5. The Zr-N bond length of fcc-ZrN of 0.2304 nm is in agreement with the experimental value of 0.2305 nm [Spillmann et al. 01]. The fcc-AlN shows only a slightly longer Al-N bond length as compared with the hcp-AlN, in agreement with the comparable mechanical strength for both polymorphs [Zhang et al. 07b].

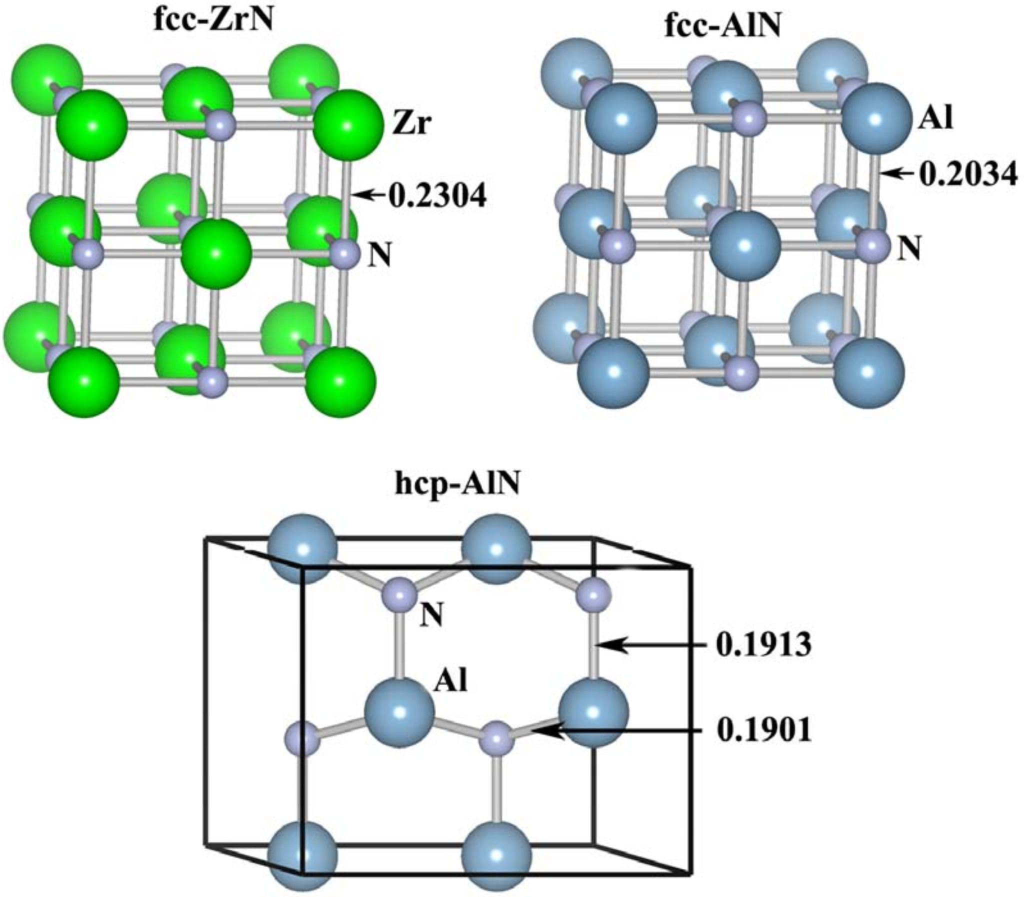

Fig. 3.2.5: The crystal structure and bond lengths (nm) of the bulk fcc-ZrN, fcc-AlN and hcp-AlN.

Figure 3.2.6 shows the structure and the variation of bond lengths of the (a) (001), (b) (110) and (c) (111) interfaces after the relaxation of the total energy at zero strain for ZrN thicknesses as indicated. The (111) interface contains only Al atoms whereas the (001) and (110) ones contain both Al and N atoms. The smallest spheres represent N, the larger ones Al, and the largest ones Zr atoms. The interatomic distances near the interface show alternations with the shortest one being the Al-N bond at the interface and the longest Zr-N bond next to it, followed by a kind of oscillations of the other Zr-N bonds lengths which are damped with increasing distance from the interface. These resemble the Friedel oscillations which occur in solids when their electronic structure is locally perturbed by foreign atoms or at solid-vacuum interfaces [Roduner 06]. The lengths of the Al-N bonds directed out of the Al-interface are larger than those in bulk fcc-AlN (0.2034 nm) for the (110) (0.2136 nm and 0.2152 nm for thinner and thicker ZrN, respectively) and (111) interfaces (0.2166 nm), but slightly smaller for the (001) interface (0.2019 nm and 0.2010 nm for the thinner and thicker ZrN, respectively). The Zr-N bond length in the layer next to the AlN interface is the largest one for the (001) interface (0.2445 nm for the thinner and 0.2444 nm for the thicker ZrN). A similar situation is found for the (110) interface, where the longest Zr-N bond length is next to the AlN interface (0.2417 nm for the thinner and 0.2488 nm for the thicker ZrN). Also in the case of the (111) interface, the longest Zr-N bond of 0.2354 is next to the AlN interface (for the time reason, we have considered only the case with the slab thickness of 2.4 nm). All these values are larger than that of bulk fcc-ZrN of 0.2304 nm.

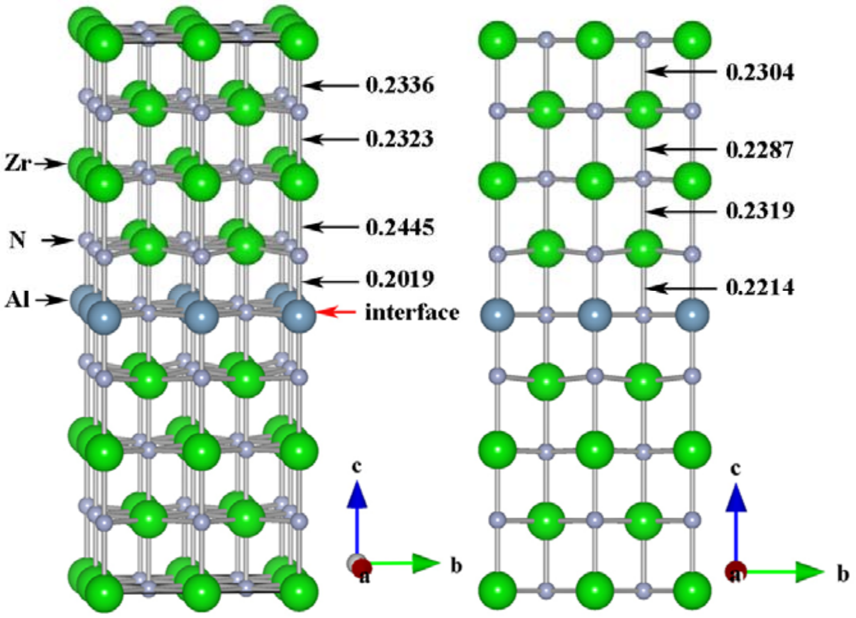
(001) interface 1.8 nm thickness

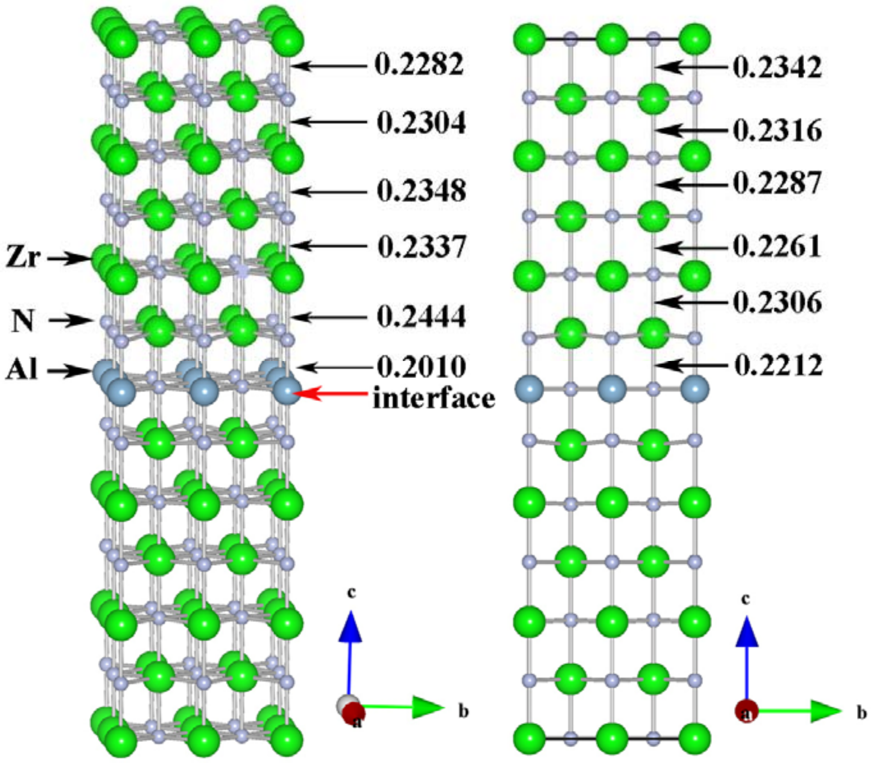
(001) interface 2.7 nm thickness

(a) (001) interface

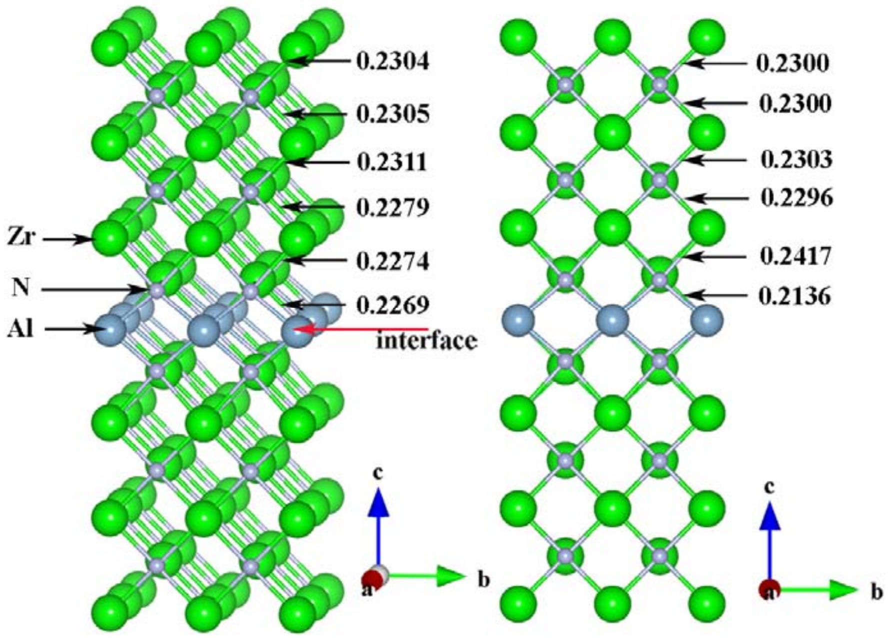

(110) interface 2 nm thickness

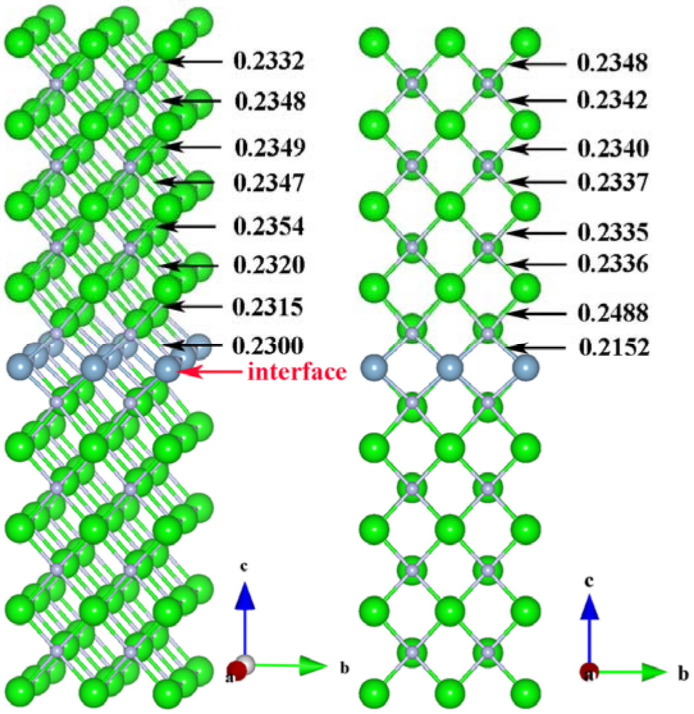

(110) interface 2.7 nm thicknees

(b) (110) interface

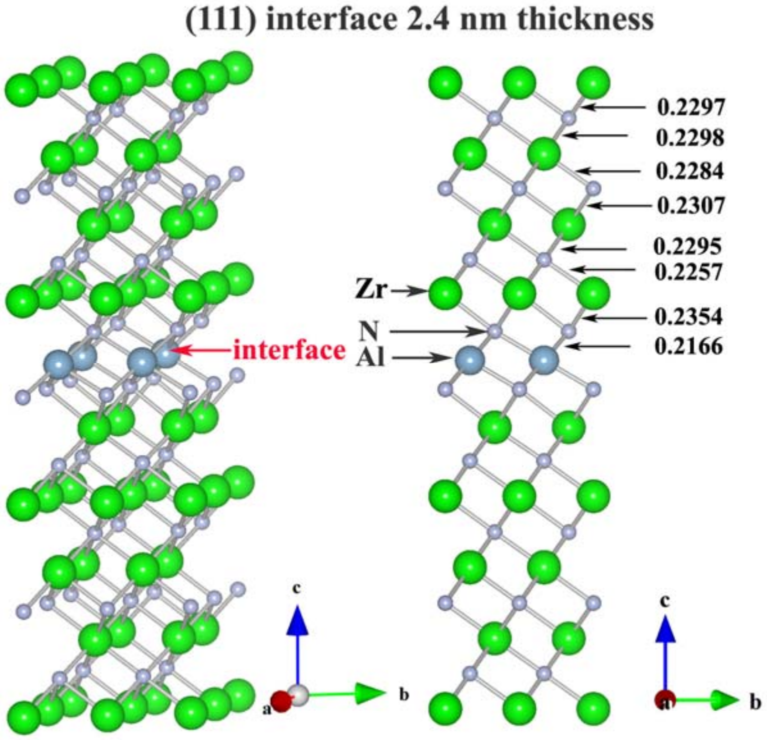

(c) (111) interface

Fig. 3.2.6: The structure and interatomic distances (in nm) of the (a) (001), (b) (110) and (c) (111) ZrN/1 ML-AlN/ZrN interfaces after full relaxation at zero strain. The bond lengths and ZrN thicknesses are shown in the figures.

Figure 3.2.7 shows the interatomic bond lengths plotted as function of distance from the AlN interface. One can see the damped Friedel-like oscillations spreading from the (001) and (111) interfaces whereas for the (110) interface only the second plane shows an enlarged bond distance. The oscillations are somewhat more pronounced for the thicker ZrN slabs, but the essential features remain preserved, i.e., the overall mechanism of the instabilities during deformation will not change with the thickness of the slabs in this range, which approximately corresponds to the crystallite size in the superhard nanocmposites.

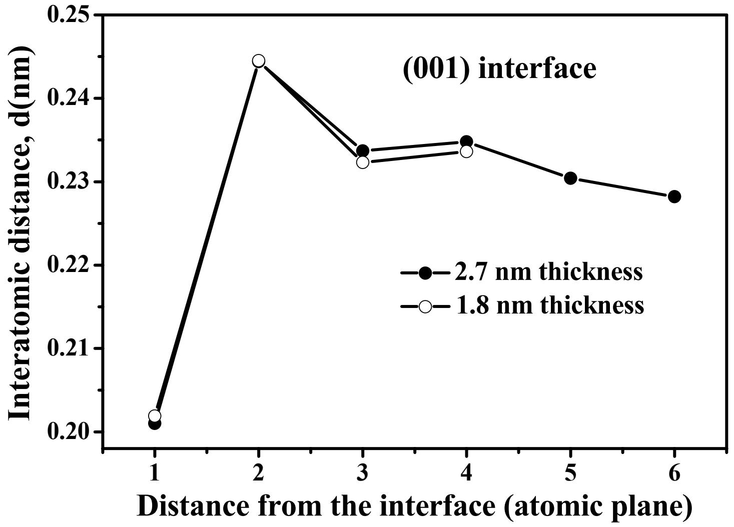
(001) interface
Interatomic distance, d(nm)
0.25
0.24
0.23
0.22
0.21
0.20
1
2
3
4
5
6
Distance from the interface (atomic plane)
2.7 nm thickness
1.8 nm thickness

(a)

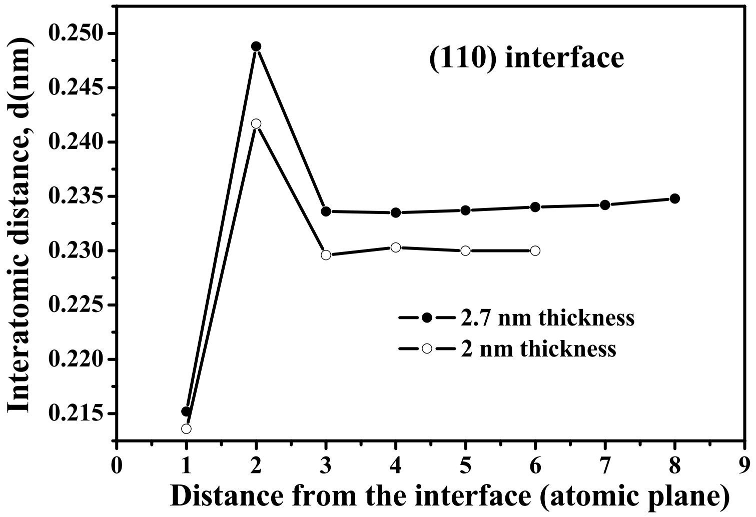
(110) interface
Interatomic distance, d(nm)
0.250
0.245
0.240
0.235
0.230
0.225
0.220
0.215
0
1
2
3
4
5
6
7
8
9
Distance from the interface (atomic plane)
2.7 nm thickness
2 nm thickness

(b)

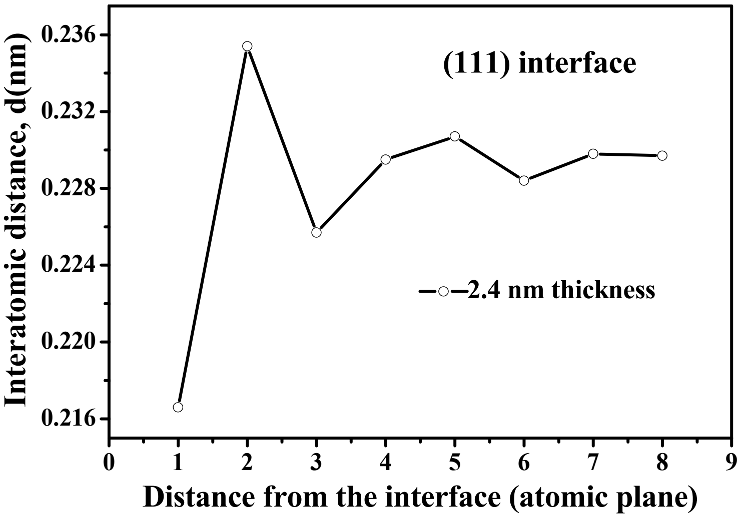

(c)

Fig. 3.2.7: The dependence of the interatomic bond length on the distance from the AlN interface for the (a) (100), (b) (110) and (c) (111) interfaces, respectively. The "position" 1 corresponds to the Al-N bond directed out of the interface.

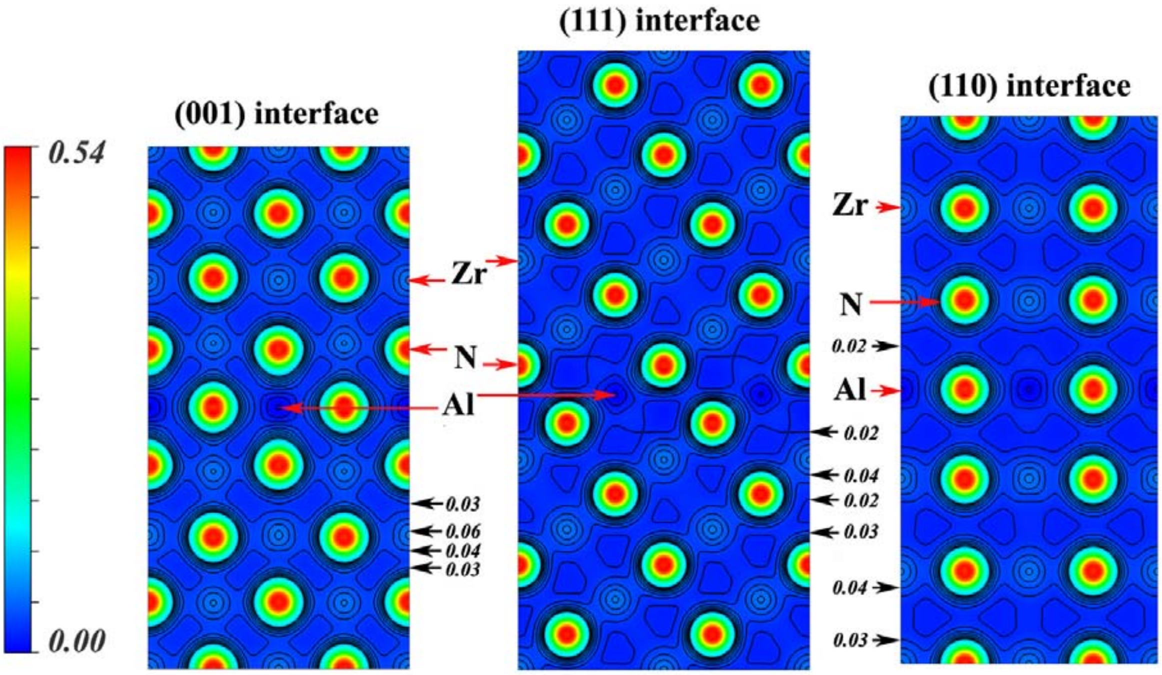

Fig. 3.2.8: Valence charge densities of the (001), (111) and (110) interfaces after full relaxation at zero strain. The scale ranges from 0.54 electrons/Bohr^3 (red) to 0 (blue).

The Friedel-like oscillations of the valence charge density, as indicated by the variable bond distances, reflect the oscillatory nature of the valence charge density in ZrN near the

AlN interface, because due to the somewhat larger electron negativity of Al (1.5) as compared with Zr (1.4) [Greenwood and Earnshaw 84] the interface is negatively charged as shown in Fig. 3.2.1.8. However, this effect is less pronounced than in the case of the TiN/1 ML-SiN_x/TiN.

Because the (111) interface contains only Al atoms and all atomic layers parallel to it within the ZrN slabs contain only one sort of atoms (either N or Zr), the Friedel-like oscillations are "in phase" around this interface. However, in the case of the (001) and (110) AlN interfaces which contain both Al and N atoms, the planes in the ZrN slabs parallel to these interfaces contain Zr as well as N atoms. This results in a kind of "phase shift" of the Friedel-like oscillations between the neighbour atomic planes perpendicular to the interface, which contain either Al or N atoms in that interface (See Fig. 3.2.6 (a) and (b)). This can be clearly seen on the (001) interface shown in Fig. 3.2.1.6 (a): The distances of Al-N bond perpendicular to the (001) interface (0.2019 nm) are evidently shorter than those of the N-Zr ones coming out of the AlN interface, and this feature propagates also in the subsequent layers parallel to that interface. These phase shifts of the Friedel-like oscillations have important effect on the sequence of bond ruptures during de-cohesion in tension, and bond flip-over, rotation and re-arrangement during ideal shear. In the following parts, we limit our discussion on the Al containing planes to show the instability under tension and shear deformations.

3.2.2.3 The mechanism of tensile de-cohesion

In this section, we shall study the mechanism of de-cohesion in tension for all three interfaces. Figure 3.2.9 shows the structures (Fig. (a)) and the valence charge density map (Fig. (b)) upon tension of the slab with the (001) interface in the <001> direction at strains of 0.1040 and 0.1716, which correspond to the maximum stress and to the de-cohesion instability, respectively (c.f. Fig. 3.2.4 (a)).

Both figures show that de-cohesion occurs between the second and third Zr-N layers parallel to the interface. This is surprising because one would expect that de-cohesion should occur between the planes with the largest distance at zero strain, i.e., between the first and second Zr-N planes (see Fig. 3.2.6 (a)) away from the interface. It were interesting to find out if this may be related to the phase shift of the Friedel-like oscillations in neighbor planes perpendicular to the interface as found in the TiN/1 ML-SiN_x/TiN system [Zhang et al. 09], or rather to the size effect. Nevertheless, it is clear that the weakening of the Zr-N bonds between the second and third Zr-N planes from the interface influences the strength of the whole interface "sandwich" more than the strengthening of the Al-N bonds.

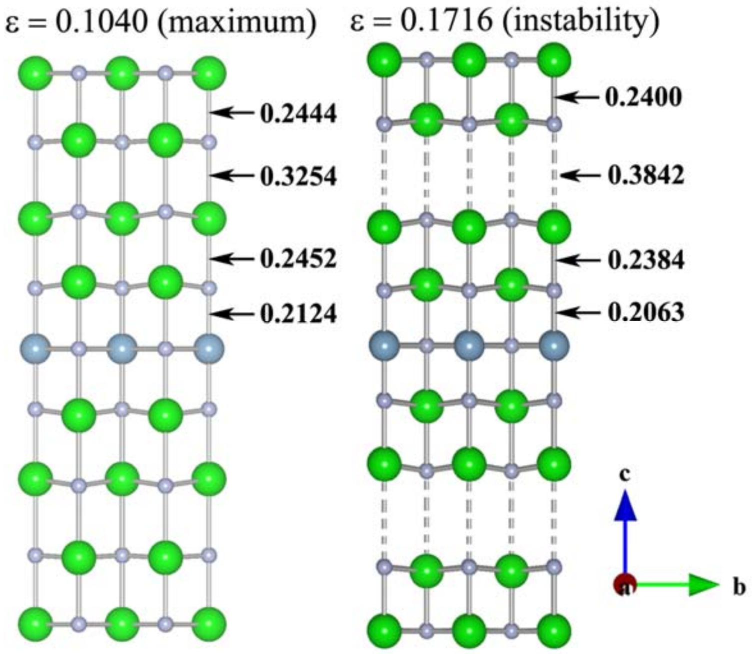

Fig. 3.2.9 (a): Changes of the interatomic distances upon tensile strain applied to the (001) interface in the <001> direction for strains as indicated. Bond lengths are given in the unit of nm.

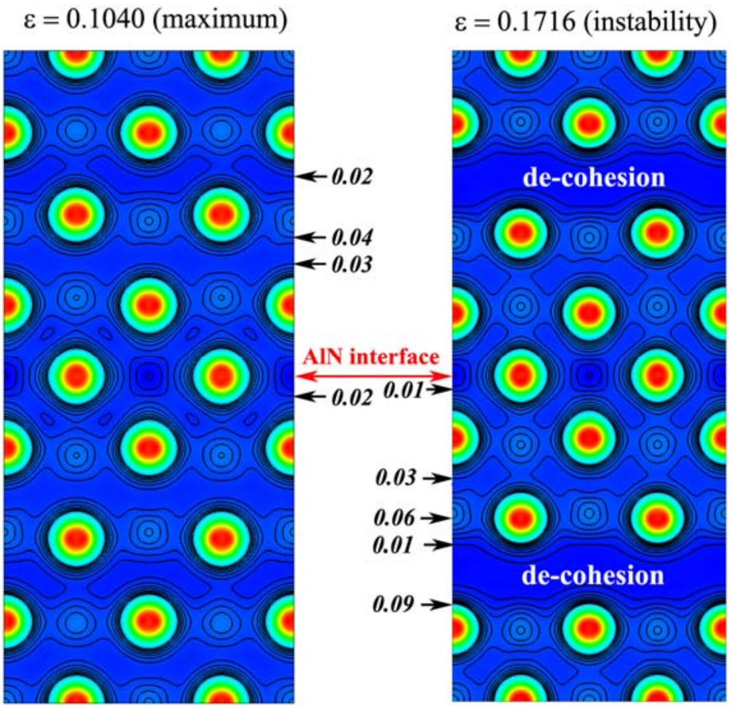

Fig. 3.2.9 (b): Changes of the valence charge density upon tensile strain applied to the (001) interface in the <001> direction for strains as indicated.

Figures 3.2.9 (c) and (d) show the changes of the interatomic distances and valence charge density upon tension strain applied to the (001) interface in the <001> direction for a thicker slab of 2.7 nm. A comparison with Figs 3.2.9 (a) and (b) reveals a close similarity in the changes of bond lengths as well as in the valence charge density. Thus also in this case the calculations performed with a thinner slab describe correctly the basic physics of the de-cohesion.

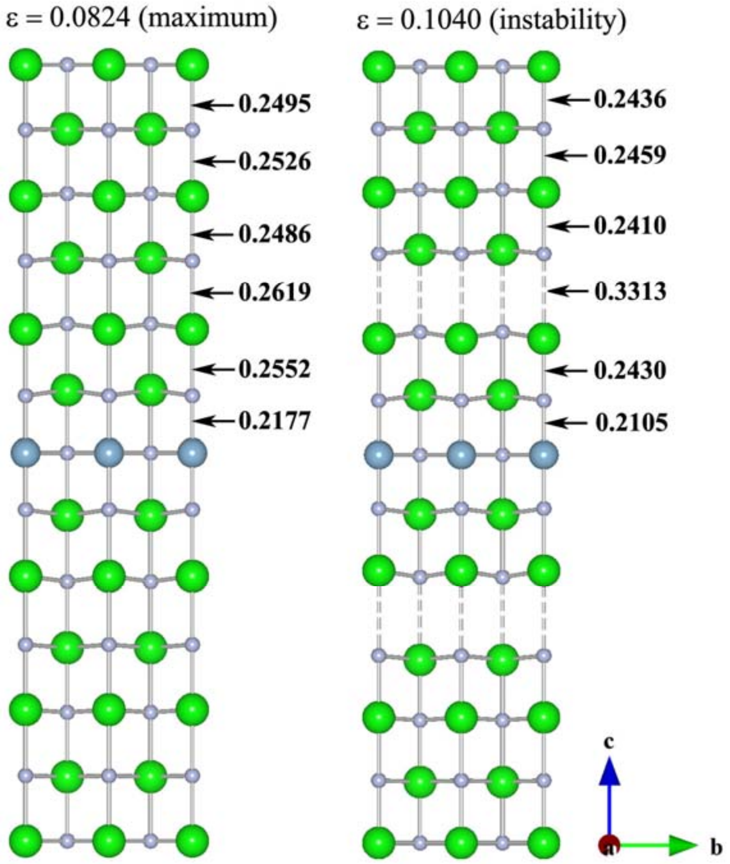

Fig. 3.2.9 (c): Changes of the interatomic distances upon de-cohesion in tension applied to the (001) interface in the <001> direction for strains as indicated. The thickness of the cell is 2.7 nm. Bond lengths are given in nm.

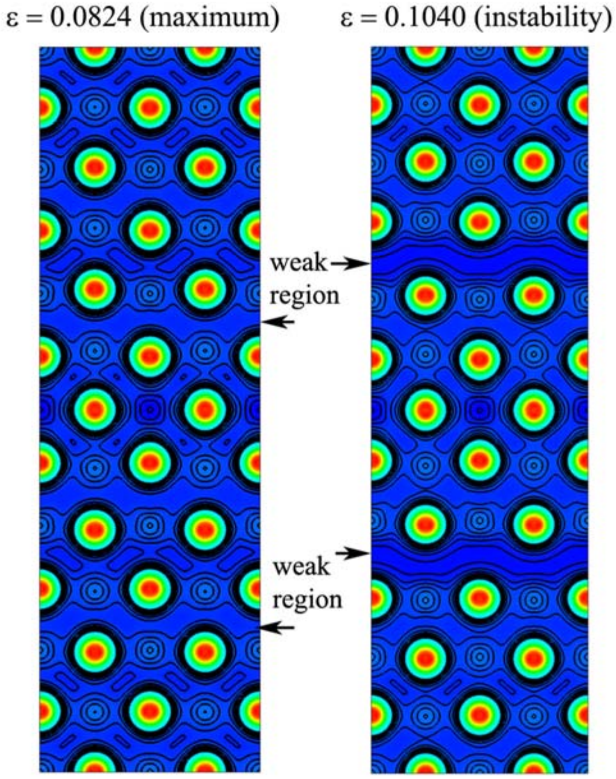

Fig. 3.2.9 (d): Changes of the valence charge density upon de-cohesion in tension applied to the (001) interface in the <001> direction for strains as indicated.

Figure 3.2.10 shows the changes of interatomic distances (Fig. (a)) and valence charge density map (Fig. (b)) upon tensile strain applied to the (111) interface in the <111> direction perpendicular to that interface for strain before and after the de-cohesion instability. One can see that in this case de-cohesion occurs between the second plane (Zr) and third palne (N) parallel to the Al interface, where the Zr-N bond length of 0.2257 nm at zero strain is the second longest one (c.f. Fig. 3.2.6 (c)). As in the previous case, the de-cohesion does not occur between the N-Zr bonds where, at zero strain, the bond distance of 0.2354 nm is the largest. Because (111) interface contains only Al atoms, the Friedel-like oscillations in the neighbor planes perpendicular to the interface are in phase.

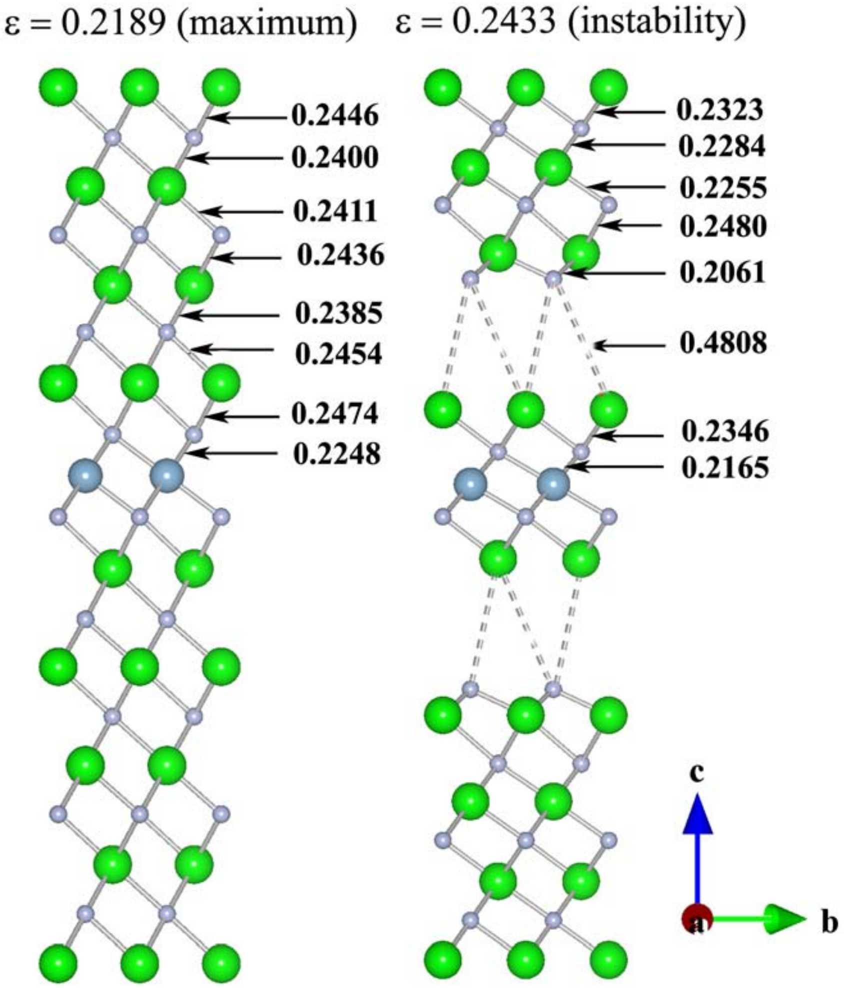

Fig. 3.2.10 (a): The atomistic mechanism of de-cohesion of the (111) interface upon the tensile strain applied in the <111> direction perpendicular to that interface for strains as indicated. The bond lengths are given in nm.

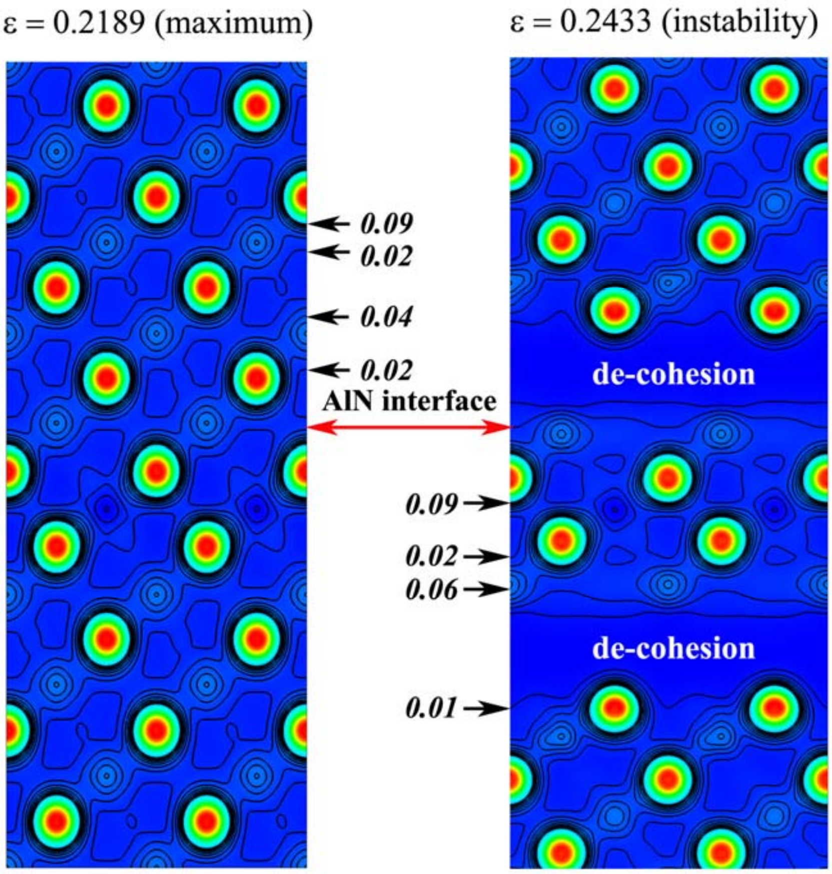

Fig. 3.2.10 (b): Changes of the valence charge density upon tensile strain applied in the (111) interface in the <111> direction perpendicular to that interface for strains as indicated.

Figure 3.2.11 shows the atomistic mechanism (Fig. (a)) and the changes of valence charge density (Fig. (b)) upon tension applied to the (110) interface in the <110> direction perpendicular to that interface for strain before and after the de-cohesion instability. One can see that in this case the instability is due to the weakening between the first and second Zr-N plane parallel to the interface. However, before and after instability, the atomic lattice still remains partially connected. This can be also seen from the stress-strain curve shown in Fig. 3.2.4 (b): after the instability, the stress does not fall to zero, but remains at a relatively high level for strain increasing up to 0.35. This is probably due to the phase shift of Friedel-like oscillations in neighbor planes perpendicular to that interface, and a complex re-distribution of the valence charge density in a similar manner as described for the TiN/1 ML-SiN$_x$/TiN system by Zhang et al. [Zhang et al. 09].

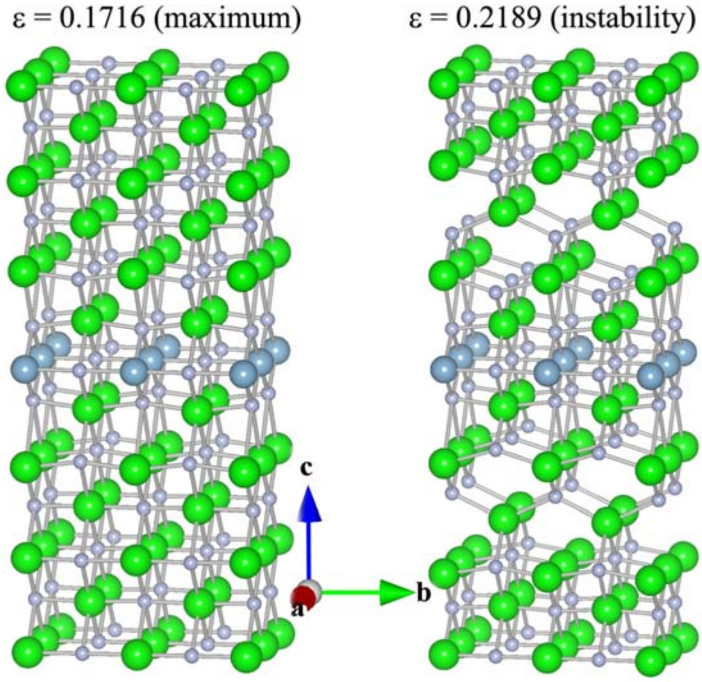

Fig. 3.2.11 (a): Three-dimensional atomistic structure pictures of de-cohesion upon tension applied to the (110) interface in the <110> direction perpendicular to that interface for strains as indicated. Bond lengths are given in the unit of nm.

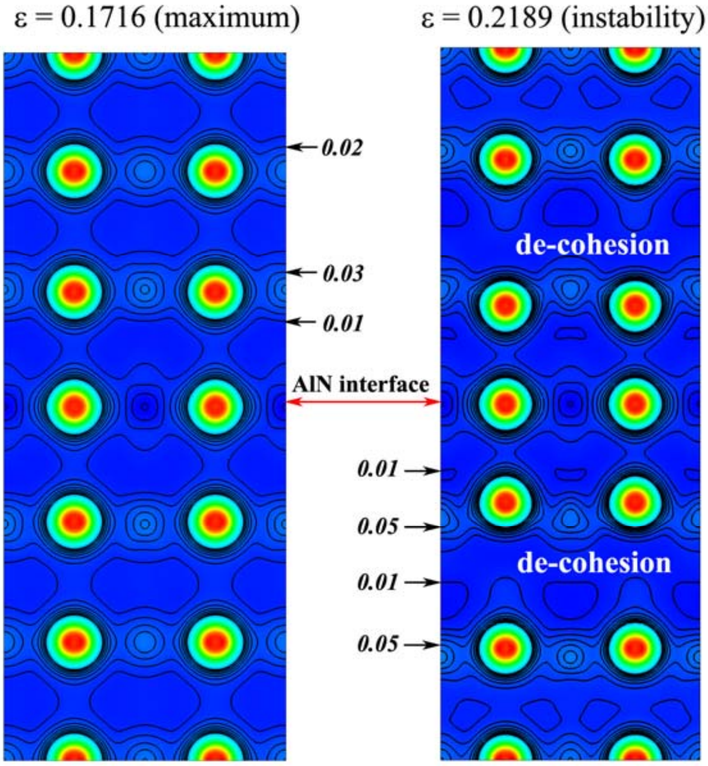

Fig. 3.2.11 (b): Changes of the valence charge density upon de-cohesion in tension applied to the (110) interface in the <110> direction perpendicular to that interface for strains as indicated.

3.2.2.4 The mechanism of shear deformation

Plastic deformation occurs in shear under constant volume (compatibility conditions). The following analysis of the changes of the valence charge density upon shear will be conducted by comparing them before and after the ideal shear instability. The atomistic structures are used to illustrate how the atoms move before and after the ideal shear deformation.

Figure 3.2.12 shows the behavior of the (001)[100] slip system as atomistic structure (Fig. (a)) and the valence charge density (Fig. (b)) for shear strains of 0.3728 and of 0.4002, which corresponds to the maximum of the stress-strain curve and to the shear instability, respectively (c.f. Fig. 3.2.4(a)). In order to see easily the shear, the atoms on the left, just before the instability, have been numbered. One can see that, by analogy with the de-cohesion discussed above, the shear occurs between the first and the second Zr-N planes parallel to the interface. The movement of the atoms between the first and second Zr-N planes is shown in Fig. 3.2.12(b). The white arrows in Fig. 3.2.12(b) show the flip-over of the Zr-N bond upon the shear instability. The valence charge densities in the regions labeled by black arrows in the Fig. 3.2.12(b) are nearly zero (see the numbers in the figure), which indicates that they are weak links.

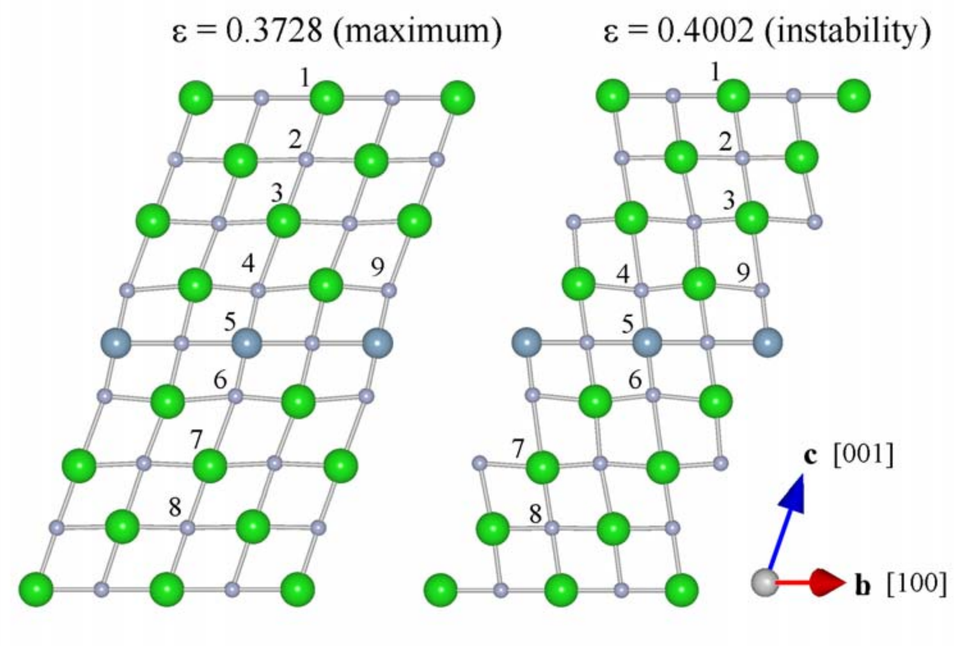

Fig. 3.2.12 (a): The atomistic structure upon the shear deformation applied to (001)[100] slip system for values of strain as indicated.

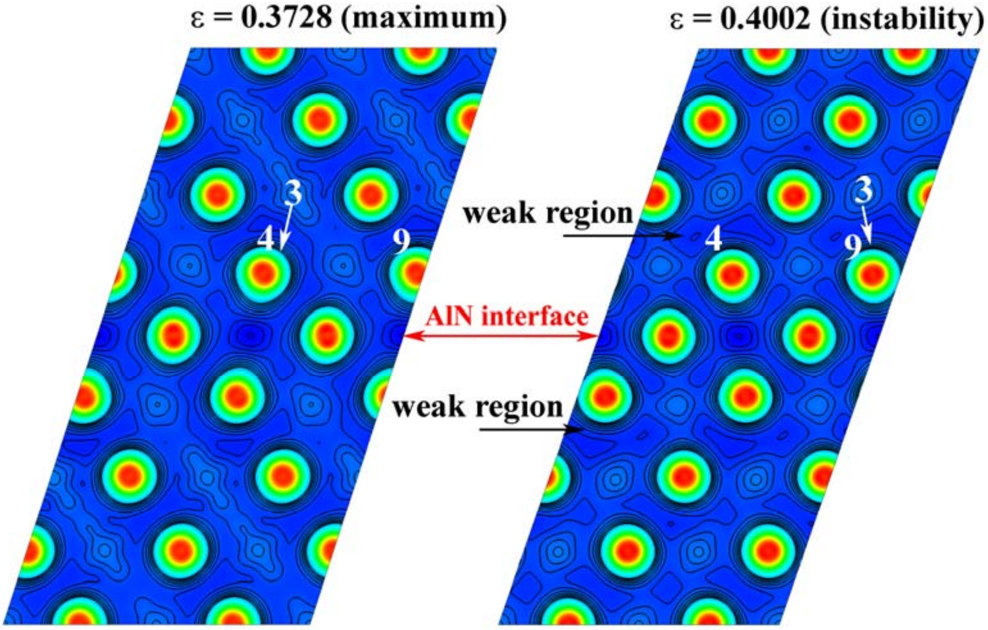

Fig. 3.2.12 (b): Changes of the valence charge density upon the shear deformation applied to (001)[100] slip system for values of strain as indicated (see text).

Figure 3.2.13 shows the behavior of the (001)[110] slip system as atomistic structure and the valence charge density for shear strains of 0.2682 and 0.2936 which correspond to the maximum of the stress-strain curve and to the shear instability, respectively (c.f. Fig. 3.2.4(a)). Figure 3.2.13 (a) shows the three-dimensional figures of the atomistic configuration. We distinguish between planes perpendicular to the interface which pass through Al atoms in that interface (Figs. (b) and (c)), and those which pass through N atoms within the (001) interface (Figs. (d) and (e)). The movement of the atoms is indicated by labeling the relevant atoms in Fig (b) and (d), whereas the flip-over of the Al-N and Zr-N bonds is shown by white arrows in the figures (c) and (e), respectively. One can see that the shear occurs between the Al and N atoms next to the interface in the first set of planes, but between Zr and N atoms remote from that interface in the second set of the planes.

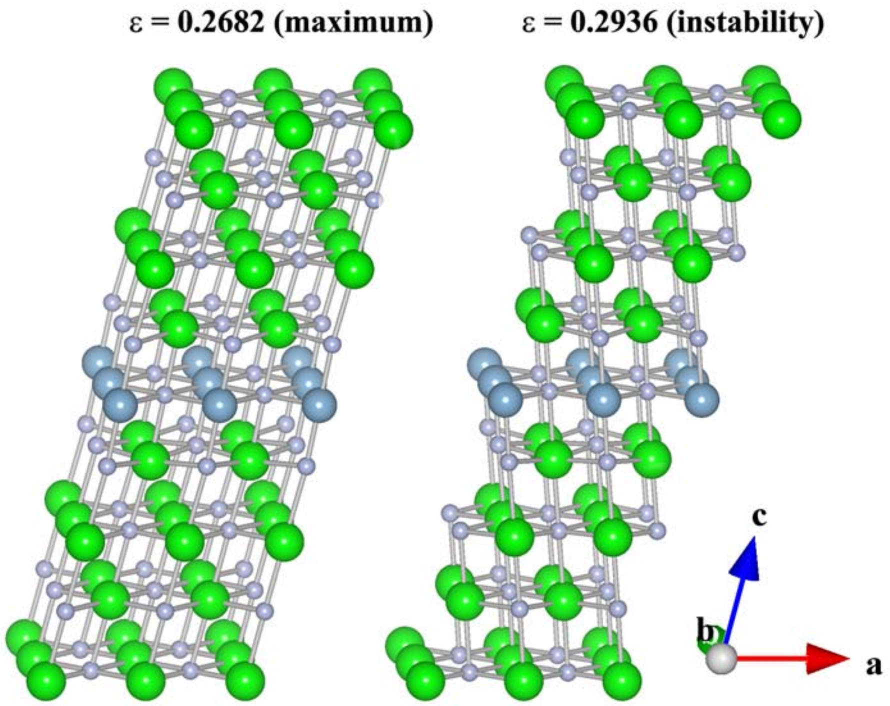

Fig. 3.2.13 (a): The three-dimensional atomistic structure pictures of shear deformation applied to (001)[110] slip system.

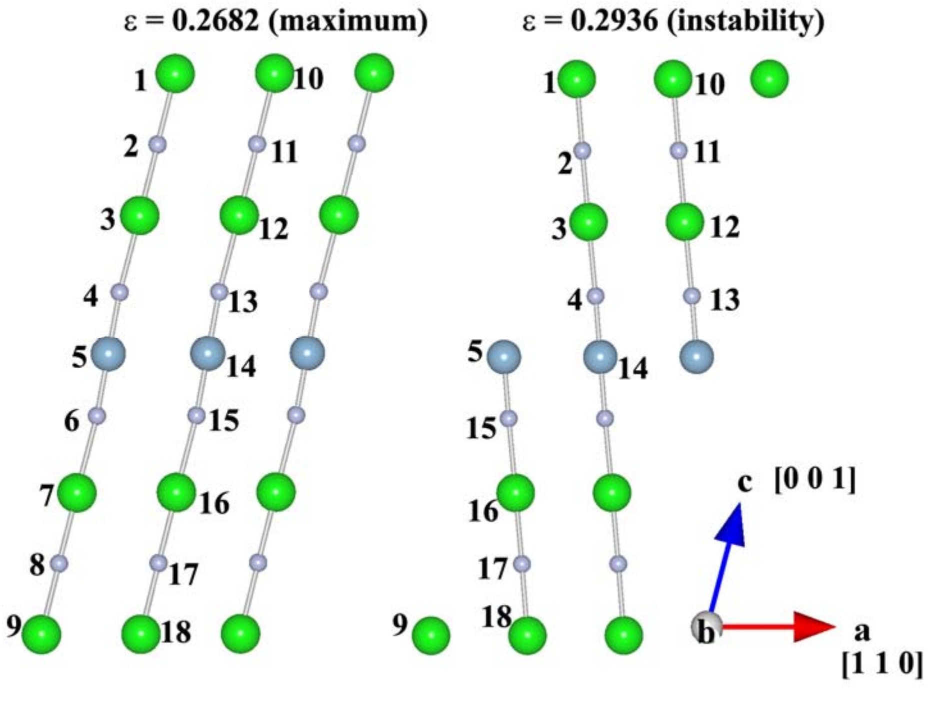

Fig. 3.2.13 (b): Movement of the atoms during the shear deformation applied to slip system (001)[110] for planes passing through Al atoms in the interface.

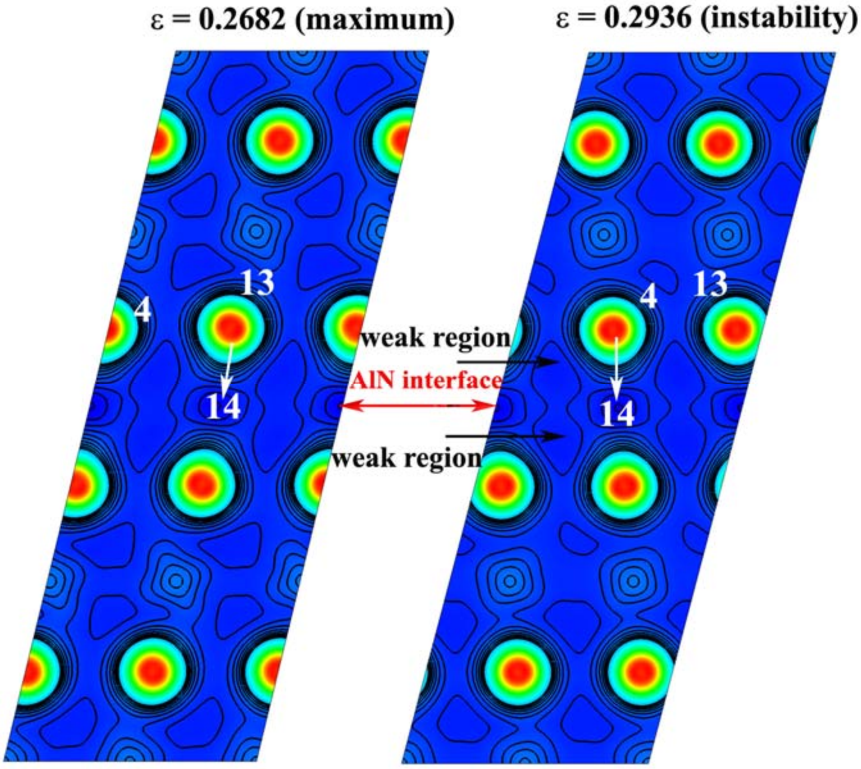

Fig. 3.2.13 (c): Changes of the valence charge density upon the shear deformation applied to (001)[110] slip system for planes passing through Al atoms in the interface.

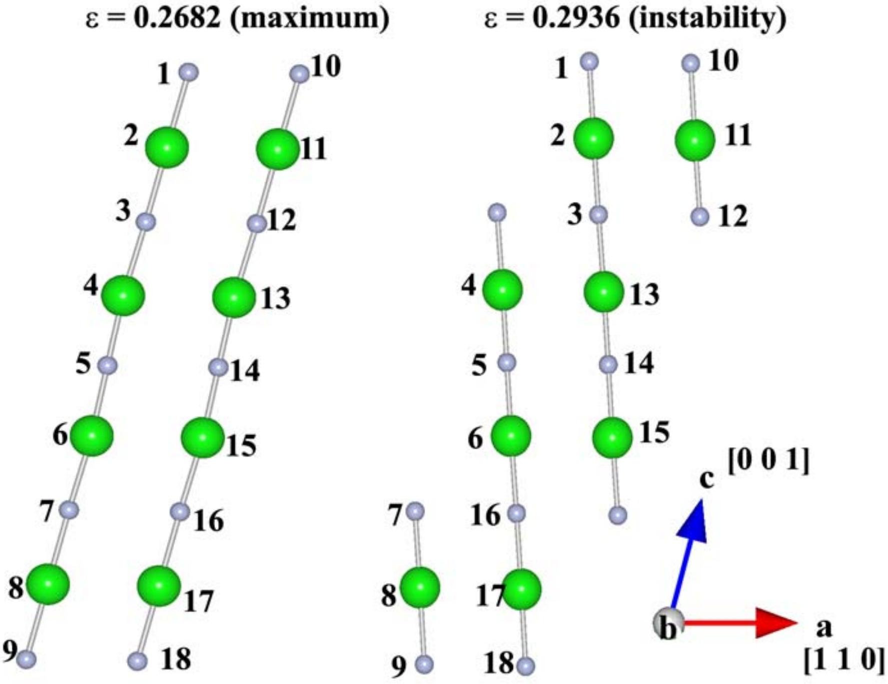

Fig. 3.2.13 (d): Movement of the atoms during the shear deformation applied to slip system (001)[110] for planes passing N atoms within the AlN interface.

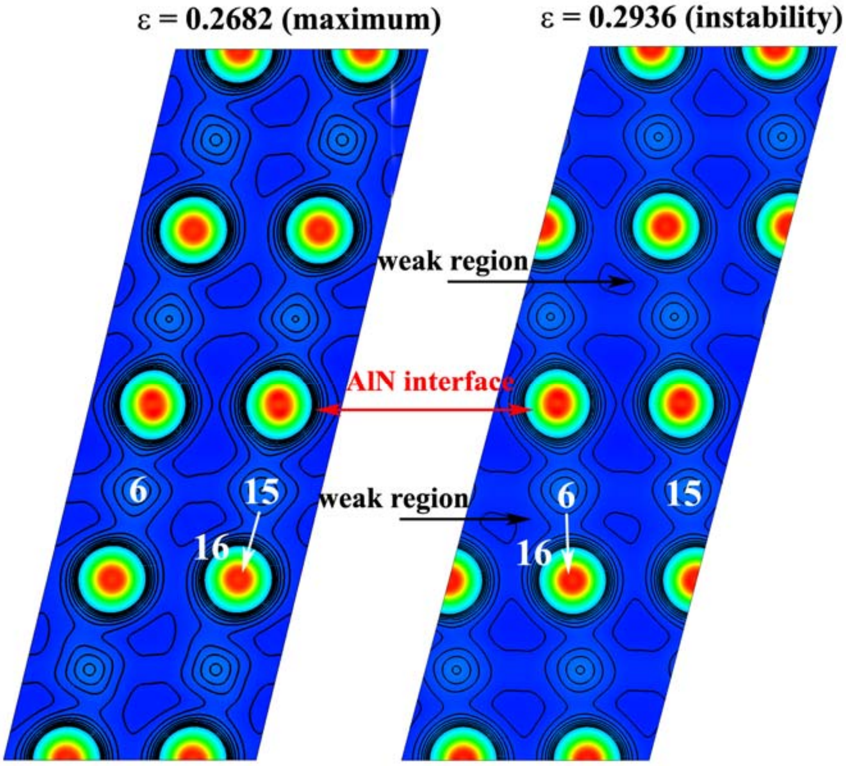

Fig. 3.2.13 (e): Changes of the valence charge density upon shear deformation applied to (001)[110] slip system for planes passing N atoms within the AlN interface.

Figure 3.2.14 shows the behavior of the (111) interface upon shear applied in the $[1\bar{1}0]$ direction. It is clearly seen that the shear occurs between the Al containing (111) interface and N atoms next to it. Figure (a) shows the atomic pictures and Fig. (b) the valence charge density. The bond flip-over is clearly seen from these figures.

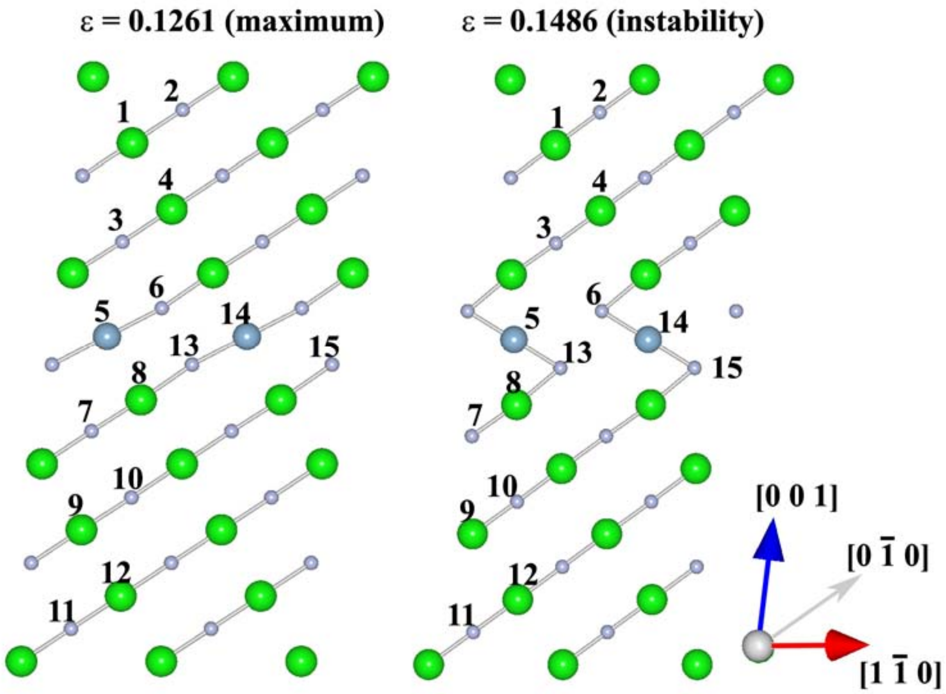

Fig. 3.2.14 (a): The atomic pictures upon shear deformation applied to $(111)[1\bar{1}0]$ slip system for values of strain as indicated.

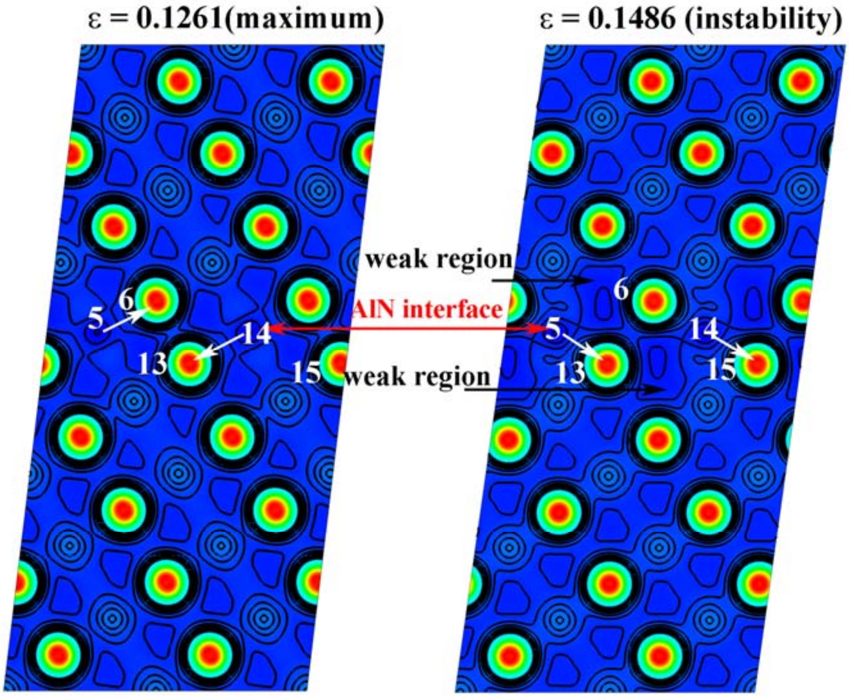

Fig. 3.2.14 (b): Changes of the valence charge density upon shear deformation applied to $(111)[1\bar{1}0]$ slip system for values of strain as indicated.

A significantly different behavior is found for the $(111)[\bar{1}\bar{1}2]$ slip system shown in Fig. 3.2.15. From the three-dimensional atomic figures in Fig. (a) and the valence charge densities maps in Fig. (b) it is seen that there is not any dramatic difference in the structure and in the valence charge density before and after the strain corresponding to the maximum of the stress-strain curve which does not show any pronounced instability but rather a smooth shape (see Fig. 3.2.4 (c)).

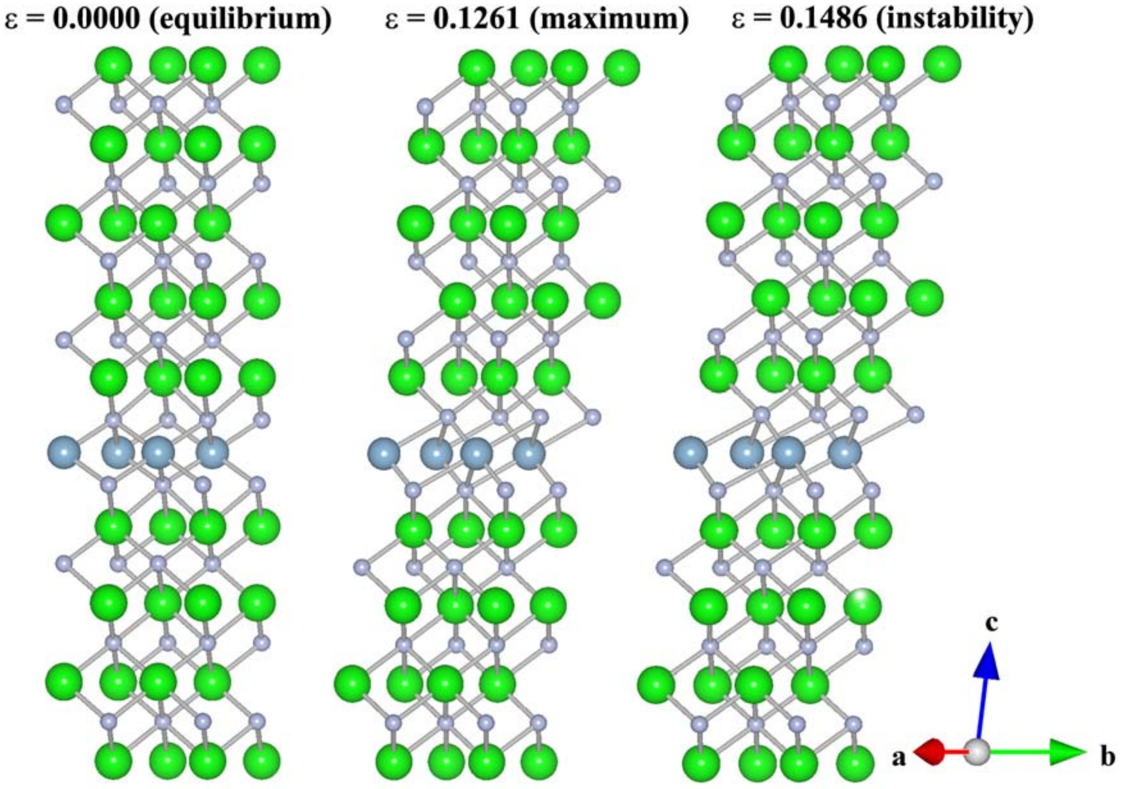

Fig. 3.2.15 (a): The three-dimensional atomic configuration pictures upon shear deformation applied to $(111)[\bar{1}\bar{1}2]$ slip system for values of strain as indicated.

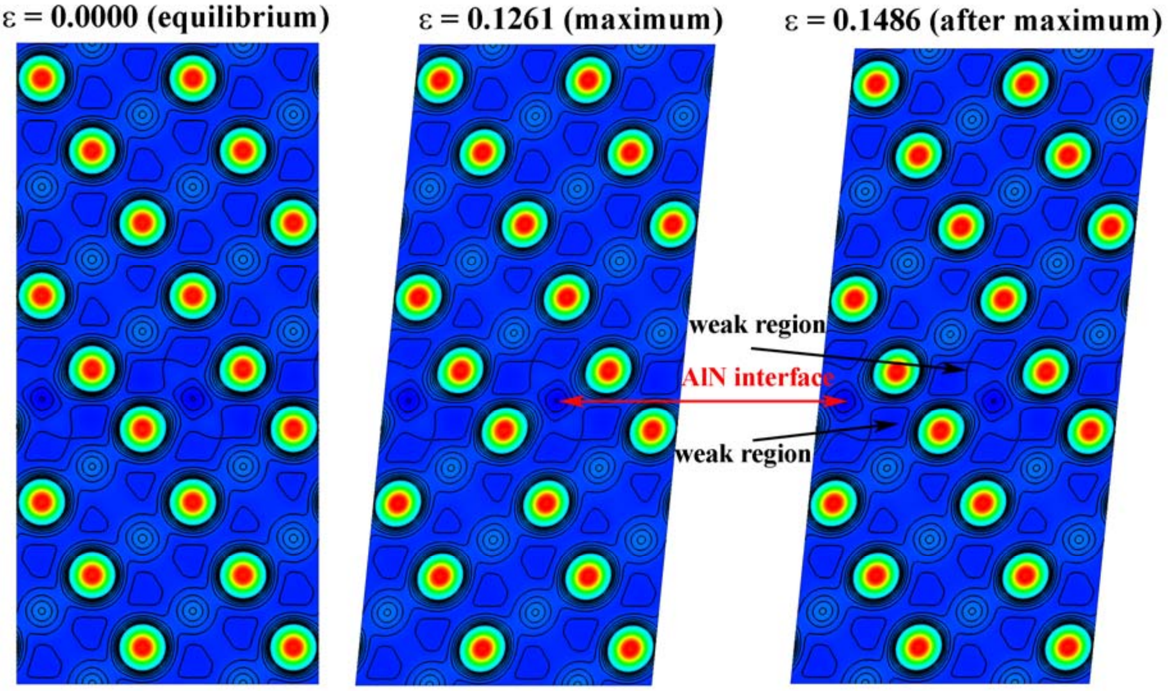

Fig. 3.2.15 (b): Changes of the valence charge density upon shear deformation applied to $(111)[\bar{1}\bar{1}2]$ slip system for values of strain as indicated.

Figure 3.2.16 shows the behavior of the (110) interface upon shear strain applied in the $[1\bar{1}0]$ direction. Referring to Fig. 3.2.4(b), this is the weakest shear direction for the (110) interface. It is seen that the sliding occurs next to the AlN interface. The atomic pictures are shown in Fig. (b) and the valence charge density in Fig.(c). During the instability, the bonds between N atom 4 and Al atom 6, and between N atom 3 and Al atom 7 are broken resulting in shear with a new configuration.

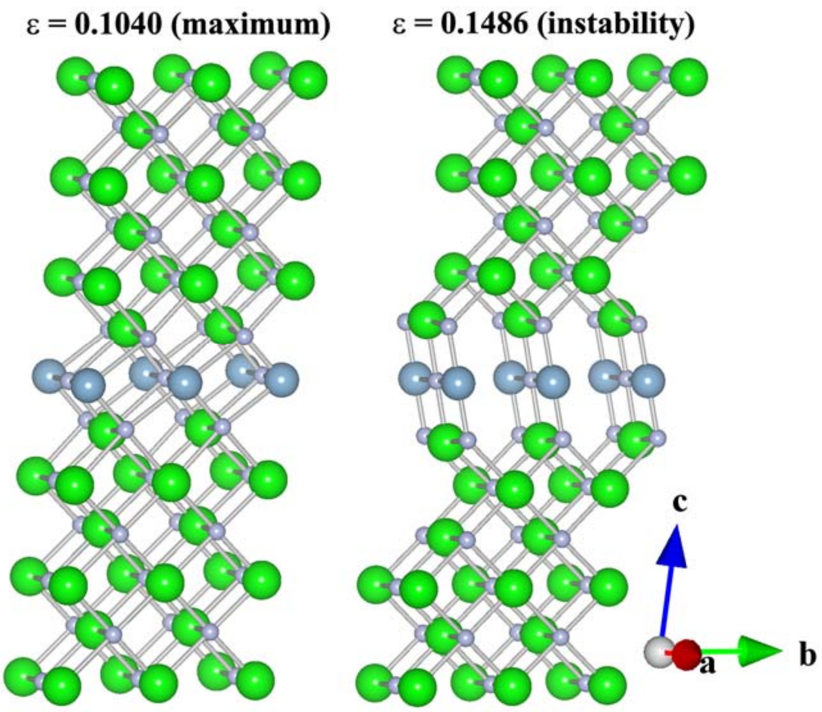

Fig. 3.2.16 (a): Three-dimensional atomic pictures upon shear deformation applied to (110) $[1\bar{1}0]$ slip system for values of strain as indicated.

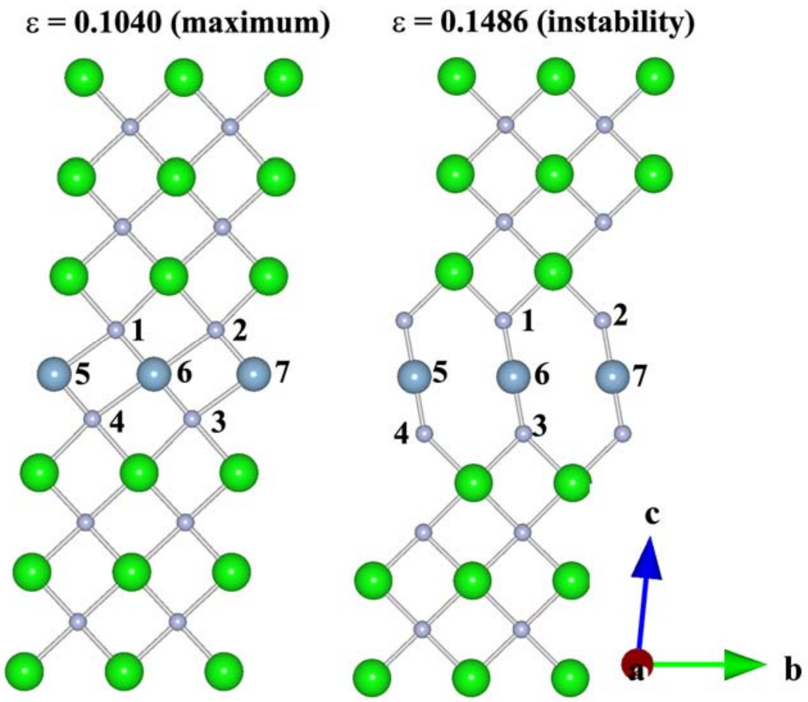

Fig. 3.2.16 (b): The atomic pictures of the (110) plane upon shear deformation applied to (110) $[1\bar{1}0]$ slip system for values of strain as indicated.

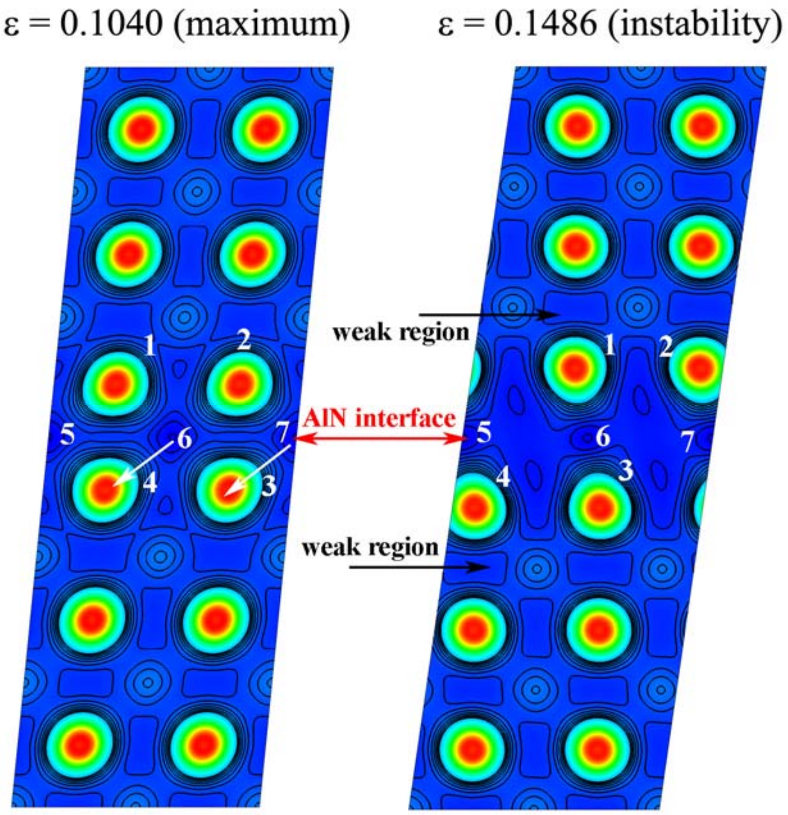

Fig. 3.2.16(c): Changes of the valence charge density upon shear deformation applied to $(110)[1\bar{1}0]$ slip system for values of strain as indicated.

3.2.2.5 Summary

The results presented in this section show that there is no enhancement of the strength in the ZrN/1 ML-AlN/ZrN system comparable to that which has been found for the TiN/1 ML-SiN$_x$/TiN one. This is somewhat surprising because Dong et al. reported a similar hardness enhancement for the ZrN/SiN$_x$/ZrN heterostructures [Dong et al. 06] as it has been found by several groups for the TiN/SiN$_x$/TiN [Söderberg et al. 05] [Söderberg et al. 07] [Hu et al. 05] [Kong et al. 07]. However, in the VN/AlN/VN heterostructures, only a small hardness enhancement with decreasing period has been reported and attributed to the Hall-Petch mechanism. In that work, no maximum of hardness has been found for an about 1 ML thin AlN interface [Li et al. 04], although nc-VN/a-Si_3N_4 nanocomposites showed clearly a hardness maximum of > 40 GPa for about 1 ML thick Si_3N_4 –like interface [Veprek 99] [Veprek et al. 05]. Therefore the results obtained in the present work seem to be in accord with the experimental findings.

The full physical explanation is beyond the scope of this work, because it would require a much detailed DFT and possibly also MD studies of several other systems.

Therefore we limit our discussion to some suggestions for the future work: The possible explanation may be searched for in the smaller difference of the electronegativity between Al and Zr of 0.1 as compared with Si and Ti of 0.3, combined with a larger difference in atomic size between Al and Zr of 0.027 nm as compared with Ti and Si of 0.021 nm. Therefore, the larger elastic strain energy caused by the misfit of the atomic sizes probably destabilize the ZrN/1 ML-AlN/ZrN system more than the small difference in the electronegativity can stabilize it. However, this suggestion should be considered as a preliminary one because processes at interfaces and their impact on mechanical properties are very complicated. For example it is known for about 100 years that 100 ppm of Bismuth makes copper very brittle, and all researchers agree that it is due to grain boundary embrittlement by segregation of Bismuth (e.g., [Rühle et al. 99] [Vitek et al. 99]), but there is still ongoing discussion whether it is dominated by size [Schweinfest et al. 04] or electronic effect [Duscher et al. 04].

Chapter 4: Conclusions and outlook

The main part of this work deals with combined, *ab initio* DFT and thermodynamic modelling of the Zr-Al-N, Zr-Si-N, Al-Si-N and Zr-Al-O systems in order to study their de-mixing properties and possibility of forming new, advanced superhard nanocomposites for industrial applications. The advantage of the combined method, developed recently by Zhang and Veprek, as compared with the quantum molecular dynamic (e.g. Car-Parrinello) approach is orders of magnitude shorter computing time needed (we estimated a factor of about 10^5). In the combined method, we first calculate, by means of *ab initio* DFT, the fundamental properties, such as the total energy vs. volume, lattice constant, bulk modulus, its derivative and cohesive energy of the relevant binary compounds ("terminal phases", such as fcc(NaCl)-ZrN, hcp(ß)-Si_3N_4 and others) and compare them with published data in order to verify the reliability of our *ab initio* DFT code and potentials used. Because in all cases very good agreement has been obtained, these calculations were extended to the ternary solid solution phases of interest, and to their corresponding hypothetical terminal phases (e.g. hcp(ß)-Zr_3N_4, fcc(NaCl)-SiN etc.) which have to be used in the DFT calculations in order to maintain the given crystal symmetry, because the calculations are done in the reciprocal space. From the formation energy calculated by the *ab initio* DFT at 0 K as function of the composition, we determined the composition-dependent interaction parameter which has been then used in the sub-lattice solution model to calculate the Gibbs free energy of the mixing of the solid solution phases at ambient pressure and different temperatures. The results were then used to study the phase stabilities and de-mixing properties of the solid solutions with the appropriate structures. Finally, the temperature-composition diagrams were constructed to determine the spinodal and binodal regimes of each of the above mentioned systems. Because in the work of other groups, a temperature independent interaction parameter has been used resulting in values of spinodal temperature which appeared to us to be too high, far above the melting points of the materials under consideration, we have investigated the effect of its linear and exponential temperature dependence on the final results. It has been found that the exponential dependence yields the most reliable results whereas using T-independent interaction parameter is obviously incorrect. Based on the calculated chemical spinodal and considering the effect of the interfacial lattice misfit elastic energy, we discussed the possibilities of the occurrence of "coherently" spinodal phase segregation and of the formation of stable nanocomposites.

In the Zr-Al-N system, the critical AlN content at which the phase transformation from fcc to hcp occurs is nearly independent of temperature. The chemical binodal and spinodal decomposition curves show that fcc-$Zr_{1-x}Al_xN$ solid solution coatings should undergo phase decomposition into fcc-ZrN and fcc-AlN. However, because of the relatively large misfit strain, the spinodal decompositon into the fcc-ZrN and metastable fcc-AlN is obviously hindered, and the decomposition into a mixture of thermodynamically stable fcc-ZrN and hcp-AlN is more probable.

The binodal and spinodal curves calculated for the fcc-$Zr_{1-x}Si_xN$ solid solution show that it should spinodally decompose into isostructural fcc-ZrN and and unstable fcc-SiN only at relatively high Si content, which would yield too thick SiN interface and avoid the formation of superhard nc-ZrN/a-Si_3N_4 nanocomposites.[7] However, the hcp-$(Zr_{1-x}Si_x)_3N_4$ system is, at the temperatures relevant for the deposition of the coatings, chemically spinodal within nearly the whole relevant range of the composition. Therefore, the spinodal decomposition combined with the phase transformation hcp-$(Zr_{1-x}Si_x)_3N_4$ → nc-fcc-ZrN + hcp(ß)- or a-Si_3N_4 is characterized by a large driving force, and, therefore, the formation of superhard nanocomposites is expected in this system. In view of the lower coefficient of friction as compared with other transition metal nitrides, the nc-ZrN/a-Si_3N_4 nanocomposites may be superior to the nc-TiN/a-Si_3N_4, nc-$(Ti_{1-x}Al_x)N$/a-Si_3N_4 and nc-$(Al_{1-x}Cr_x)N$/a-Si_3N_4 systems which are presently being used in large-scale industrial applications. The most likely mechanism of the phase segregation is the nucleation and growth of the fcc-ZrN within a tissue of SiN_x which, in course of continuing decomposition and reaction transform into the thermodynamically stable Si_3N_4. The spinodal decomposition of fcc-$Zr_{1-x}Si_xN$ is possible at high Si fraction. Such a system is, however, unlikely to yield strengthened thin ZrN interface because the electronegativity of Zr is lower than that of Si and, therefore, no strengthening of the ZrN interface is expected.

The Al-Si-N system has been chosen because both terminal phases are covalent nitrides with hexagonal structures. At the temperatures of interest for deposition and applications, the $Al_{1-x}Si_xN_y$ solid solutions with both hcp(ZnS) and hcp(ß) structure are immiscible with typical characteristics of chemical spinodal. Considering the instabilities of the hypothetical terminal phases hcp(ß)-Al_3N_4 and hcp(ZnS)-SiN with respect to their stable modifications hcp(ZnS)-AlN and hcp(ß)-Si_3N_4, spinodal decomposition accompanied by the

---

[7] Notice that in all superhard nanocomposites studied so far, the maximum hardnes has been achieved when the interfacial SiN_x layer was about one monolayer thick. This has been fully explained by the recent *ab initio* DFT calculations of Hao et al. and by Zhang et al.

phase transformation into the thermodynamically stable phases should occur, provided the nitrogen activity during the decomposition is sufficiently high.

Because high oxidation resistance is important for materials applied as wear protective coatings on tools for hard and dry machining (drilling, milling, turning and the like), oxides are of great interests. However, so far, only α-Al_2O_3 deposited at high temperatures of about 1000°C, which limits the choice of the substrate material to cemented carbide only, has been used. Therefore the Zr-Al-O system has been chosen as the most promising candidate which may form nanocomposites with enhanced hardness. The *ab initio* DFT calculations of such an oxide system represent a challenge because it is more difficult than that of the nitrides or carbides. Nevertheless, the obtained results have been checked to be reliable when the exponential dependence of the interaction parameter has been used. The binodal and spinodal curves show that the system should undergo spinodal phase segregation within the composition range that is relevant for the formation of superhard nanocomposites, provided the deposition temperature is sufficiently high in order to assure fast diffusion, which kinetically controls the segregation. These results provide guideline for more precise experimental work to be done in the future, particularly as regards the temperature and partial pressure of oxygen during the deposition.

In the last part of this work, we studied the mechanical properties of the stable terminal phases and the metastable $Zr_{1-x}Al_xN$ solid solution, by calculating the stress-strain curves in tension (relevant for crack growth and brittle fracture) and shear (relevant for plastic deformation) for several slip systems. The results for bulk phases showed only a small reduction of the ideal strengths for the ternary solid solution as compared with the pure binary terminal phases. These calculations have then been extended to heterostructures consisting of few nm thick slabs of ZrN with one monolayer thick pseudomorphic AlN interface. In contrast to the TiN/1 ML SiN_x/TiN system, no enhancement of the strength has been found for the ZrN/1 ML-AlN/ZrN heterostructures. These results appear to be in agreement with experimental ones because hardness enhancement has been reported for the TiN/1 ML-SiN_x/TiN and ZrN/1 ML SiN_x/ZrN heterostructures, but not for the VN/1-ML AlN/VN ones. The very long CPU time needed for these calculations did not allow their extension to other system within the time frame available for the present work. This remains a challenge for the future work because the search for new and better superhard nanocomposite systems by such "first principles design" is, in spite of the large CPU time needed, much more efficient and cheaper than experimental trial and error approach.

References

[Adibi et al. 91] F. Adibi, I. Petrov, L. Hultman, U. Wahlström, T. Shimizu, D. McIntyre, J. E. Greene and J.-E. Sundgren, J. Appl. Phys. **69** (1991) 6437.

[Aguayo et al. 02] A. Aguayo, G. Murrieta and R. de Coss, Phys. Rev. B **65** (2002) 092106.

[Alling et al. 07] B. Alling, A. V. Ruban, A. Karimi, O. E. Peil, S. I. Simak, L. Hultman and I. A. Abrikosov, Phys. Rev. B **75** (2007) 045123.

[Alling et al. 08] B. Alling, E. I. Isaev, A. Flink, L. Hultman and I. A. Abrikosov, Phys. Rev. B **78** (2008) 132103.

[Amour et al. 78] H. d'Amour, D. Schiferl, W. Denner, H. Schulz and W. B. Holzapfer, J. Appl. Phys. **49** (1978) 4411.

[Anderbouhr et al. 99] S. Anderbouhr, S. Gilles, E. Blanquet, C. Bernard and R. Madar, Chem. Vap. Dep. **5** (1999) 109.

[Arroyave & Liu 06] R. Arroyave and Z. K. Liu, CALPHAD **30** (2006) 1.

[Argon 08] A. S. Argon, *Strengthening Mechanisms in Crystal Plasticity*, Oxford University Press, Oxford 2008.

[Åstrand et al. 04] M. Åstrand, T. I. Selinder, F. Fietzke and H. Klostermann, Surf. Coat. Technol. **188–189** (2004) 186.

[Barin 93] I. Barin, *Thermochemical Data of Pure Substances*, 2nd ed., VCH-Verlag, Weinheim 1993.

[Barnett 93] S. A. Barnett, in: Physics of Thin Films, Vol. **17**, *Mechanic and Dieletric Properties*, eds. M. H. Francombe and J. L. Vossen, Academic Press, Boston 1993.

[Barnett & Madan 98] S. A. Barnett, A. Madan, Phys. World **11** (1998) 45.

[Bekalda et al. 00] R. Bekalda, T. Shibayanagi and M. Naka, J. Amer. Ceram. Soc. **83** (2000) 2449.

[Berg et al. 00] G. Berg, C. Friedrich, E. Broszeit and C. Berger, in: *Handbook of Ceramic Hard Materials*, ed. R. Riedel, Wiley-VCH, Weinheim 2000.

[Birch 47&78] F. Birch, Phys. Rev. B **71** (1947) 809; J. Geophys. Res. **83** (1978) 1257.

[Blöchl 94] E. Blöchl, Phys. Rev. B **50** (1994) 17953.

[Born & Huang 54] M. Born and K. Huang, *Dynamical Theory of Crystal Lattices*, Clarendon, Oxford 1954.

[Brazhkin et al. 02] V. V. Brazhkin, A. G. Lyapin and R. J. Hemley, Phil. Mag. **A 82** (2002) 321.

[Cahn & Hillard 58] J. W. Cahn and J. E. Hillard, J. Chem. Phys. **28** (1958) 258.

[Cahn 61] J. W. Cahn, Acta Metall. **9** (1961) 795.

[Cahn 63] J. W. Cahn, Acta Metall. **11** (1963) 1275.

[Cahn 68] J. W. Cahn, Trans. Metall. Soc. of AIME **242** (1968) 166.

[Cahn 91] J. W. Cahn, Scand. J. Metall. **20** (1991) 9.

[Chase et al. 85] M. W. Chase, C. A. Davies, J. R. Downey et al., *JANAF Thermochemical Tables*, 3rd. ed. J. Phys. Chem. Ref. Data **14** (1985), Supplement No. 1.

[Chen 02] L. Q. Chen, Ann. Rev. Mater. Res. **32** (2002) 113.

[Chen et al. 07] S. Chen, X. G. Gong and S.H. Wei, Phys. Rev. Lett. **98** (2007) 015502.

[Ching et al. 98] W. Y. Ching, Y. N. Yu, J. D. Gale and M. Ruhle, J. Am. Ceram. Soc. **81** (1998) 3189.

[Clemens et al. 99] B. M. Clemens, H. Kung and S. A. Barnett, MRS Bulleting **24** (1999) 20.

[Cohen 85] M. L. Cohen, Phys. Rev. B **32** (1985) 7988.

[Cselle 05] T. Cselle, Vacuum's best VIP, Wiley-VCH Verlag GmbH & Co KGaA, Weinheim, 2005, p. 33.

[Cselle 05b] T. Cselle, in: *Spanende Fertigung*, 4. Edition, ed. K. Weinert, Vulkan Verlag, Essen 2005, p. 229.

[Desgreniers & Lagarec 99] S. Desgreniers and K. Lagarec, Phys. Rev. B **59** (1999) 8467.

[Ditchek & Schwartz 79] B. Ditchek and L. H. Schwartz, Ann. Rev. Mater. Sci. **9** (1979) 219.

[Dimitrova et al. 98] V. Dimitrova, D. Manova, T. Paskova, Tz. Uzunov, N. Ivanov and D. Dechev, Vacuum **51** (1998) 161.

[Dong et al. 06] Y. S. Dong, W. J. Zhao, J. L. Yue and G. Y. Li, Appl. Phys. Lett. **89** (2006) 121916.

[Dove 93] M. T. Dove, *Introduction to Lattice Dynamics*, Cambridge University Press, Cambridge 1993.

[Dubrovinskaia et al. 07] N. Dubrovinskaia, V. L. Solozhenko, N. Miyajima, V. Dmitriev, O. O. Kurakevich and L. Dubrovinsky, Appl. Phys. Lett. **90** (2007) 101912.

[Duscher et al. 04] G. Duscher, M. F. Chisholm, U. Alber and M. Rühle, Nature Materials **3** (2004) 621.

[Freeman & Wimmer 1995] A. J. Freeman and E. Wimmer, Ann. Rev. Mater. Sci. 25 (1995) 7.

[Gilman 03] J. J. Gilman, *Electronic Basis of the Strength of Materials*, Cambridge University Press, Cambridge 2003.

[Greenwood and Earnshaw 84] N. N. Greenwood and A. Earnshaw, *Chemistry of Elements*, Pergamon Press, Oxford 1984.

[Haines et al. 01] J. Haines, J. M. Leger and G. Bocquillon, Ann. Rev. Mater. Res. **31** (2001) 1.

[Hao et al. 06] S. Hao, B. Dellay, S. Veprek and C. Stampfl, Phys. Rev. Lett. **97** (2006) 086102.

[Hao et al. 06b] S. Hao, B. Dellay and C. Stampfl, Phys. Rev. B **74** (2006) 035402.

[Hao et al. 06c] S. Hao, B. Dellay and C. Stampfl, Phys. Rev. B **74** (2006 035424.

[Hasegawa et al. 05] H. Hasegawa, M. Kawate and T. Suzuki, Surf. Coat. Technol. **200** (2005) 2409.

[Hermann et al. 05] M. Hermann, F. Furtmayr, A. Bergmaier, G. Dollinger, M. Stutzmann and M. Eickhoff, Appl. Phys. Lett. **86** (2005) 192108.

[Hertzberg 89] R. W. Hertzberg, *Deformation and Fracture Mechanics of Engineering Materials*, 3rd ed., J. Wiley & Sons, New York 1989.

[Hillert et al. 61] M. Hillert, M. Cohen and B. L. Averbach, Acta Metall. **9** (1961) 536.

[Hillert 98] M. Hillert, *Phase Equilibria, Phase Diagrams and Phase Transformations: Their Thermodynamic Basis*, Cambridge University Press, Cambridge (U.K.) 1998.

[Hillert & Jonsson 92] M. Hillert and S. Jonsson, Calphad **16** (1992) 199.

[Hirai et al. 00] M. Hirai, Y. Ueno, T. Suzuki, W. Jiang, C. Grigoriu and K. Yatsui, Jpn. J. Appl. Phys. **40** (2000) 1056.

[Hofman & Jehn 90] S. Hofmann and H. A. Jehn, Werkstoffe und Korrosion **41** (1990) 756.

[Hohenberg & Kohn 1964] P. Hohenberg and W. Kohn, Phys. Rev. **136** (1964) 864.

[Holleck 86] H. Holleck, J. Vac. Sci. Technol. A **4** (1986) 2661.

[Holleck 88] H. Holleck, Surf. Coat. Technol. **36** (1988) 151.

[Holubar et al. 00] P. Holubar, M. Jilek and M. Sima, Surf. Coat. Technol. **133-134** (2000) 145.

[Howard et al. 88] C. J. Howard, R. J. Hill and B. E. Reichert, Acta Crystallogr. B **44** (1988) 116.

[Howe 97] J. M. Howe, *Interfaces in Materials*, Wiley Interscience, New York 1997.

[Hu & Chen 04] S. Y. Hu and L. Q. Chen, Acta Mater. **52 (**2004) 3069**.**

[Hu et al. 05] X. P. Hu, H. J. Zhang, J. W. Dai, G. Y. Li and M. Y. Gu, J. Vac. Sci. Technol. A **23** (2005) 114.

[Huber & Herzerg 79] K. P. Huber and G. Herzberg, Molecular Spectra and Molecular Structure IV: Constants of Diatomic Molecules, Van Nostrand Reinhold, New York 1979.

[Hugosson et al. 01] H. W. Hugosson, U. Jansson, B. Johansson and O. Eriksson, Science **293** (2001) 2434.

[Hugosson et al. 03] H. W. Hugosson, H. Högberg, M. Algren, M. Rodmar and T. I. Selinder, J. Appl. Phys. **93** (2003) 4505.

[Iuga et al. 07] M. Iuga, G. Steinle-Neumann and J. Meinhardt, Eur. Phys. J. B **58** (2007) 127.

[Jain et al. 97] S. C. Jain, A. H. Harker, R. A. Cowley, Phil. Mag. A **75** (1997) 1461.

[Jain et al. 00] S. C. Jain, M. Willander, J. Narayan and R. Van Overstraeten, J. Appl. Phys. **87** (2000) 965.

[Jehn et al. 86] H. A. Jehn, S. Hofmann, V.-E. Rückborn and W.-D. Münz, J. Vac. Sci. Technol. A **4** (1986) 2701.

[Jerebtsov et al. 00] D. A. Jerebtsov, G. G. Mikhailov and S. V. Sverdina, Ceramics International **26** (2000) 821.

[Jia et al. 06] Y. Jia, Y. Hotta, K. Sato and K. Watari, J. Am. Ceram. Soc. **89** (2006) 103.

[Jilek et al. 03] M. Jilek, T. Cselle, P. Holubar, M. Morstein, M. G. J.Veprek-Heijman and S. Veprek, Plasma Chem. Plasma Processing **24** (2004) 493.

[Jilek et al. 03b] M. Jilek, P. Holubar, M. G. J. Veprek-Heijman and S. Veprek, MRS Symp. Proc. **750** (2003) 393.

[Jomard et al. 99] G. Jomard, T. Petit, A. Pasturel, L. Magaud, G. Kresse and J. Hafner, Phys. Rev. B **59** (1999) 4044.

[Kalss et al. 06] W. Kalss, A. Reiter, V. Deflinger, C. Gey and J. L. Endrin, Int. J. Refract. Metals & Hard Mater. **24** (2006) 399.

[Kaner et al. 05] R. B. Kaner, J. J. Gilman and S. H. Tolbert, Science **308** (2005) 1268.

[Kaptay 04] G. Kaptay, CALPHAD **28** (2004) 115.

[Kasper & Lonsdale 72] *International Tables for X-Ray Crystallography*, Vol. I., edited by J. S. Kasper and K. Lonsdale, Kynoch Press, Birmingham 1972.

[Kasu et al. 01] M. Kasu, Y. Taniyasu and N. Kobayashi, Jpn. J. Appl. Phys. **40** (2001)1048.

[Kawate et al. 03] M. Kawate, A. K. Hashimoto and T. Suzuki, Surf. Coat. Technol. **165** (2003) 163.

[Klostermann et al. 05] H. Klostermann, B. Böcher, F. Fietzke, T. Modes and O. Zywitzki, Surf. Coat. Technol. **200** (2005) 760.

[Knauth & Schoonman 02] P. Knauth and J. Schoonman, *Nanocrystalline Metals and Oxides :Selected Properties and Applications,* Knauth P, Kluwer Academic Publishers, New York, Boston, Dordrecht, London, Moscow 2002.

[Knotek et al. 86] O. Knotek, M. Bohmer and T. Leydendecker, J. Vac. Sci. Technol. A **4** (1986) 2695.

[Knotek et al. 91] O. Knotek, F. Löffler and H. J. Scholl, Surf. Coat. Technol. **45** (1991) 53.

[Kohn & Sham 1965] W. Kohn and L. Sham, Phys. Rev. **140** (1965) 1133.

[Kohara et al. 04] T. Kohara, H. Tamagaki, Y. Ikari and H. Fuji, Surf. Coat. Technol. **185** (2004) 166.

[Koski et al. 99] K. Koski, J. Holsa and P. Juliet, Surf. Coat. Technol. **120-121** (1999) 303.

[Kong et al. 07] M. Kong, W. Zhao, L. Wei, G. Y. Li, J. Phys. D: Appl. Phys. **40** (2007) 2858.

[Kresse & Hafner 93] G. Kresse and J. Hafner, Phys. Rev. B **47** (1993) 558.

[Kresse & Furthmüller 96] G. Kresse and J. Furthmüller, Comput. Mat. Sci. **6** (1996) 15.

[Kresse & Furthmüller 96b] G. Kresse and J. Furthmüller, Phys. Rev. B **54** (1996) 11169.

[Kresse & Joubert 99] G. Kresse and D. Joubert, Phys. Rev. B **59** (1999) 1758.

[Kronberg 57] M. L. Kronberg, Acta Metall. Mater. **5** (1957) 507.

[Lamni et al. 05] R. Lamni, R. Sanjinés, M. Parlinska-Wojtan, A. Karimi and F. Lévy, J. Vac. Sci. Technol. A **23** (2005) 593.

[Lazar 06] P. Lazar, Ph D Thesis, University of Vienna, Faculty of Physics 2006.

[Lee & Lagerlof 85] W. E. Lee and K. P. D. Lagerlof, J. Electron Micr. Tech. **2** (1985) 247.

[Léonard & Desai 98] F. Léonard and R. C. Desai, Phys. Rev. B **58** (1998) 8277.

[Li et al. 02] W. X. Li, C. Stampfl and M. Scheffler, Phys. Rev. B **65** (2002) 075407.

[Li 06] D. J. Li, Science in China Series E: Technological Sciences **49** (2006) 576.

[Li et al. 02] J. Li, K. J. Van Vliet, T. Zhu, S. Yip and S. Suresh, Nature **418** (2002) 307.

[Li et al. 04] G. Y. Li, J. Lao, J. Tian, Z. Han and M. Gu, J. Appl. Phys. **95** (2004) 310104.

[Liu & Cohen 90] A. Y. Liu and M. L. Cohen, Science **254** (1989) 841; Phys. Rev. B **41** (1990) 10727.

[Liu et al. 09] H. Liu, W. Tang, D. Hui, L. Hei and F. Lu, Thin Solid Films **517** (2009)5988.

[MACHERENA 07] EU Project MACHERENA, S. Veprek, private communication (2008).

[Martin 04] R. M. Martin, *Electronic Structure, Basic Theory and Practical Methods*. Cambridge University Press, Cambridge 2004.

[Matsunaga et al. 03] K. Matsunaga, T. Tanaka, T. Yamamoto and Y. Ikuhara, Phys. Rev. B **68** (2003) 085110.

[Mayrhofer et al. 03] P. H. Mayrhofer, A. Hörling, L. Karlsson, J. Sjölen, T. Larsson, C. Mitterer and L. Hultman, Appl. Phys. Lett. **83** (2003) 2049.

[Mayrhofer et al. 06] P. H. Mayrhofer, D. Music and J. M. Schneider, J. Appl. Phys. **100** (2006) 094906.

[Mayrhofer et al. 06b] P. H. Mayrhofer, D. Music, J. M. Schneider, Appl. Phys. Lett. **88** (2006) 071922.

[Mayrhofer et al. 07] P. H. Mayrhofer, F. D. Fischer, H. J. Böhm, C. Mitterer C and J. M. Schneider, Acta Mater. **55** (2007) 1441.

[Mazel et al. 97] A. Mazel, P. Marti, F. Henry, B. Armas, R. Bonnet and M. Loubradou, Thin Solid Films **304** (1997) 256.

[Monkhorst & Pack 76] H. J. Monkhorst and J. D. Pack, Phys. Rev. B **13** (1976) 5188.

[Münz 86] W.-D. Münz, J. Vac. Sci. Technol. A **4** (1986) 2717.

[Münz 90] W.-D. Münz, Werkstoffe und Korrosion **41** (1990) 753.

[Musil et al. 08] J. Musil, M. Šašek, P. Zeman, R. Čerstvý, D. Heřman, J. G. Han and V. Šatava, Surf. Coat. Technol. **202** (2008) 3485.

[Murnaghan 44] F. D. Murnaghan, Proc. Natl. Acad. Sci. **30** (1944) 244.

[Nagao et al. 06] S. Nagao, K. Nordlund and R. Nowak, Phys. Rev. B **73** (2006) 144113.

[Niederhofer et al. 99] A. Niederhofer, P. Nesladek, H.-D. Männling, K. Moto, S. Veprek, and M. Jilek, Surf. Coat. Technol. **120-121** (1999) 173.

[Nose et al. 02] M. Nose, W. A. Chiou, M. Zhou, T. Mae and M. Meshii, J. Vac. Sci. Technol. A **20** (2002) 823.

[PalDey & Deevi 03] S. PalDey and S.-C. Deevi, Mater. Sci. Eng. A **342** (2003) 58.

[Pan et al. 07] Z. C. Pan, H. Sun and C. F. Chen, Phys. Rev. Lett. **98** (2007) 135505.

[Park & Baik 05] J. K. Park and Y. J. Baik, Surf. Coat. Technol. **200** (2005) 1519.

[Paul 04] D. J. Paul, Semicond. Sci. Technol. **19** (2004) R75.

[Pedrew & Wang 92] J. P. Perdew and Y. Wang, Phys. Rev. B **45** (1992) 13244.

[Pelisson et al. 07] A. Pélisson, M. Parlinska-Wojtan, H. J. Hug and J. Patscheider, Surf. Coat. Technol. **202** (2007) 884.

[Perdew et al. 1992] J. P. Perdew, J. A. Chevary, S. H. Vosko, K. A. Jackson, M. R. Pederson, D. J. Singh and C. Fiolhais, Phys. Rev. B. **46** (1992) 6671.

[Perdew et al. 96] J. P. Perdew, K. Burke and M. Ernzerhof, Phys. Rev. Lett. **77** (1996) 3865.

[Pokluda et al. 04] J. Pokluda, M. Cerny, P. Sandera and M. Sob, J. Comput.-Aided Mater. Des. **11** (2004) 1 and reference therein.

[Piras et al. 08] F. M. Piras, R. D. Mundo, F. Fracassi and A. Magnani, Surf. Coat. Technol. **202** (2008) 1606.

[Porter & Easterling 01] D. A. Porter and K. E. Easterling, *Phase Transformations in Metals and Alloys*, 2nd ed., Nelson Thornes, Cheltenham 2001.

[Ramm et al. 07] J. Ramm, M. Ante, T. Bachmann, B. Widrig, H. Brändle and M. Döbeli, Surf. Coat. Technol. **202** (2007) 876.

[Reiter et al. 05] A. E. Reiter, V. H. Derflinger, B. Hanselmann, T. Bachmann and B. Sartory, Surf. Coat. Technol. **200** (2005) 2114.

[Redlich & Kister 48] O. Redlich and A. Kister, Ind. Eng. Chem. **40** (1948) 345.

[Reiter et al. 07] A. E. Reiter, C. Mitterer and B. Satory, J. Vac. Sci. Technol. A **25** (2007) 711.

[Rice 2000] R. W. Rice, *Mechanical Properties of Ceramics and Composites*, CRC 2000

[Roduner 06] E. Roduner, *Nanoscopic Materials*, RSC Publishing, Royal Soc. of Chem., Cambridge 2006.

[Rogl & Schuster 92] P. Rogl and J. C. Schuster, *Phase Diagrams of Ternary Boron Nitride and Silicon Nitride Systems*, ASM, The Materials Information Society, Materials Park, Ohio 44073, 1992.

[Roundy et al. 01] D. Roundy, C. R. Krenn, M. L. Cohen and J. W. Morris, Jr., Phys. Rev. Lett. **82** (1999) 2713; Phil. Mag. A **81** (2001) 1725.

[Rühle et al. 99] M. Rühle et al., in: Inst. Phys. Conf. Series No. 161: Section 1, 1999, ed. C. J. Kiely, IOP Publ. Ltd, p. 1.

[Sandu et al. 06a] C. S. Sandu, F. Medjani, R. Sanjinés, A. Karimi and F. Lévy, Surf. Coat. Technol. **201** (2006) 4219.

[Sandu et al. 06b] C. S. Sandu, R. Sanjinés, M. Benkahoul, F. Medjani and F. Levy, Surf. Coat. Technol. **201** (2006) 4083.

[Sandu et al. 07a] C. S. Sandu, F. Medjani and R. Sanjinés, Rev. Adv. Mater. Sci. **14** (2007) 14.

[Sandu et al. 07b] C. S. Sandu, F. Medjani and R. Sanjinés, Rev. Adv. Mater. Sci. **15** (2007) 173.

[Sandu et al. 08] C. S. Sandu, R. Sanjinés and F. Medjani, Surf. Coat. Technol. **202** (2008) 2278.

[Sanjinés et al. 02] R. Sanjinés, O. Banakh, C. Rojas, P. E. Schmid and F. Lévy, Thin Solid Films **494** (2002) 312.

[Sanjinés et al. 06] R. Sanjinés, C. S. Sandu, R. Lamni and F. Lévy, Surf. Coat. Technol. **200** (2006) 6308.

[Saunders & Miodownik 98] N. Saunders and A. P. Miodownik, *CALPHAD (Calculation of Phase Diagrams): A Comprehensive Guide*, Pergamon Materials Series Vol. 1, Exeter 1998.

[Schram et al. 04] B. C. Schramm, H. Scheerer, H. Hoche, E. Broszeit, E. Abele and C. Berger, Surf. Coat. Technol. **188-189** (2004) 623.

[Scott & Orr 83] W. D. Scott and K. K. Orr, J. Am. Ceram. Soc. **66** (1983) 27.

[Schweinfest et al. 04] R. Schweinfest, A. T. Paxton and M. W. Finnis, Nature **432** (2004) 1008.

[Sheng et al. 08] S. H. Sheng, R. F. Zhang and S. Veprek, Acta Mater. **56** (2008) 968.

[Shi et al. 07] H. Q. Shi, R. Asahi and C. Stampfl, Phys. Rev. B **75** (2007) 205125.

[Siegel et al. 06] A. Siegel, K. Parlinski and U. D. Wdowik, Phys. Rev. B **74** (2006) 104116.

[Singh et al. 1991] D. J. Singh, W. E. Pickett and H. Krakauer, Phys. Rev. B **43** (1991) 11628.

[Söderberg et al. 05] H. Söderberg, M. Oden, J. M. Molina-Aldareguia and L. Hultman, J. Appl. Phys. **97** (2005) 114327.

[Söderberg et al. 07] H. Söderberg, M. Oden, A. Flink, J. Birch, P. O. A. Persson. M. Beckers, et al., J. Mater. Res. **22** (2007) 3255.

[Song et al. 04] Z. X. Song, K. W. Xu and H. Chen, Thin Solid Films. **468** (2004) 203.

[Speck & Chibu 09] J. S. Speck and S. F. Chibu, Mater. Res. Soc. Bull. **34** (2009) 304.

[Spencer 94] P. J. Spencer, J. Thermal Anal. **41** (1994) 1305.

[Spencer 98] P. J. Spencer, Thermochimica **314** (1998) 1.

[Spencer 01] P. J. Spencer, Calphad **25** (2001) 163.

[Spencer & Holleck 90] P. J. Spencer and H. Holleck, High Temp. Sci. **27** (1990) 295.

[Spillmann et al. 01] H. Spillmann, P. R. Willmott, M. Morstein and P. J. Uggowitzer, Appl. Phys. A **73** (2001) 441.

[Sproul 96] W. D. Sproul, Science **273** (1996) 889.

[Stampfl & Walle 99] C. Stampfl and C. G. Van de Walle, Phys. Rev. B **59** (1999) 5521.

[Stampfl et al. 01] C. Stampfl, W. Mannstadt, R. Asahi and A. J. Freeman, Phys. Rev. B **63** (2001) 155106 and reference therein.

[Stefanovich et al. 94] E. V. Stefanovich, A. L. Shluger and C. R. A. Catlow, Phys. Rev. B **49** (1994) 560.

[Stolten 91] H. Stolten, Ph D Thesis, RTWH Aachen, Germany 1991.

[Sundgren & Hentzell 86] J.-E. Sundgren and H.-T. Hentzell, J. Vac. Sci. Technol. A **4** (1986) 2259.

[Suzuki et al. 00] T. Suzuki, Y. Makino, M. Samandi and S. Miyake, J. Mater. Sci. **35** (2000) 4193.

[Tanaka et al. 92] Y. Tanaka, T. M. Gür, M. Kelly, S. B. Hagstrom, T. Ikeda, K. Wakihira, H. Satoh, J. Vac. Sci. Technol. A **10** (1992) 1749.

[Teter 98] D. M. Teter, MRS Bull. **23** (1998) 22.

[Trinh et al. 06] D. H. Trinh, H. Högberg, J. M. Andersson, M. Collin, I. Reineck, U. Helmersson and L. Hultman, J. Vac. Sci. Technol. A **24** (2006) 309.

[Trinh et al. 08] D. H. Trinh, T. Kubart, T. Nyberg, M. Ottosson, L. Hultman and H. Högberg, Thin Solid Films **516** (2008) 8352.

[Trinh et al. 08b] D. H. Trinh, M. Ottosson, M. Collin, I. Reineck, L. Hultman and H. Högberg, Thin Solid Films **516** (2008) 4977.

[Umeno et al. 07] Y. Umeno, Y. Kinoshita and T. Kitamura, Modelling Simul. Mater. Sci. Eng. **15** (2007) 27.

[Vanderbilt 90] D. Vanderbilt, Phys. Rev. B **41** (1990) 7892.

[Veprek et al. 95] S. Veprek and S. Reiprich, Thin Solid Films **268** (1995) 64.

[Veprek et al. 95b] S. Veprek, J. Weidmann and F. Glatz, J. Vac. Sci. Technol. A **13** (1995) 2914.

[Veprek et al. 96] S. Veprek, M. Haussmann and S. Reiprich, J. Vac. Sci. Technol. A **14** (1996) 46.

[Veprek 99] S. Veprek, J. Vac. Sci. Technol. A **17** (1999) 2401.

[Veprek & Argon 02] S. Veprek and A. S. Argon, J. Vac. Sci. Technol. B **20** (2002) 650.

[Veprek & Jilek 02] S. Veprek and M. Jilek, Vacuum **67** (2002) 443.

[Veprek et al. 03] S. Veprek, S. Mukherjee, P. Karvankova, H.-D. Männling, J. L. He, K. Moto, J. Prochazka and A. S. Argon, J. Vac. Sci. Technol. A **21** (2003) 532.

[Veprek et al. 05] S. Veprek, M. G. J. Veprek-Heijman, P. Karvankova and J. Prochazka, Thin Solid Films **476** (2005) 1.

[Veprek et al. 05b] S. Veprek, P. Karvankova and M. J. G. Veprek-Heijman, J. Vac. Sci. Technol. B **23** (2005) L17.

[Veprek et al. 07] S. Veprek, A. S. Argon and R. F. Zhang, Phil. Mag. Lett. **87** (2007) 955.

[Veprek & Veprek-Heijman 08] S. Veprek and M. G. J. Veprek-Heijman, Surf. Coat. Technol. **202** (2008) 5063.

[Veprek et al. 09] S. Veprek, R. F. Zhang, M. G. J. Veprek-Heijman, S. H. Sheng and A. S. Argon, invited paper at the MRS Europe Spring Meeting, June 2009, Surf. Coat. Technol. in press.

[Veprek-Heijman et al. 09] M. G. J. Veprek-Heijman, R. G. Veprek, A. S. Argon, D. M. Parks and S. Veprek, Surf. Coat. Technol. **203** (2009) 3385.

[Vetter et al. 98] J. Vetter, E. Lugscheider and S. S. Guerreiro, Surf. Coat. Technol. **98** (1998) 1233.

[Vitek et al. 99] V. Vítek et al., in: *Interfaces: Structures and Properties*, ed. S. Ranganathan, Trans. Tech. Publications, New Dehli 1999, p. 3.

[Vinet et al. 86] P. Vinet, J. Ferrante, J. R. Smith and J. H. Rose, J. Phys. C: Solid State Phys. **19** (1986) L 467.

[Vinet et al. 87] P. Vinet, J. H. Rose, J. Ferrante and J. R. Smith, J. Phys.: Condens. Matter **1** (1987) 1941.

[Vliet et al. 03] K. J. Van Vliet, J. Li, T. Zhu, S. Yip and S. Suresh, Phys. Rev. B **67** (2003) 104105.

[Vogelgesang et al. 00] R. Vogelgesang, M. Grimsditch and J. S. Wallace., Appl. Phys. Lett., **76** (2000) 982.

[Weitzer et al. 90] F. Weitzer, K. Remschnig, J. C. Schuster and P. Rogl, J. Mater. Res. **5** (1990) 2152.

[Willmann et al. 06] H. Willmann, P. H. Mayrhofer, P. O. Å. Persson, A. E. Reiter, L. Hultman and C. Mitterer, Scripta Mater. **54** (2006) 1847.

[Wyckoff 63] R. W. G. Wyckoff, *Crystal Structures*, 2nd ed. Vol. 1, Wiley, New York 1963.

[Zhang & Veprek 06] R. F. Zhang and S. Veprek, Mater. Sci. Eng. A **424** (2006)128.

[Zhang & Veprek 07] R. F. Zhang and S. Veprek, Mater. Sci. Eng. A **448** (2007) 111.

[Zhang & Veprek 07a] R. F. Zhang and S. Veprek, Phys. Rev. B **76** (2007) 174105.

[Zhang & Veprek 07b] R. F. Zhang and S. Veprek, Acta Mater. **55** (2007) 4615.

[Zhang & Veprek 08] R. F. Zhang and S. Veprek, Thin Solid Films **516** (2008) 2264.

[Zhang et al. 07] R. F. Zhang, S. H. Sheng and S. Veprek, Phys. Rev. B **76** (2007) 075208.

[Zhang et al. 07b] R. F. Zhang, S. H. Sheng and S. Veprek, Appl. Phys. Lett. **91** (2007) 031906.

[Zhang et al. 07c] R. F. Zhang, S. Veprek and A. S. Argon, Appl. Phys. Lett. **91** (2007) 201914.

[Zhang et al. 07d] R. F. Zhang, S. H. Sheng and S. Veprek, Appl. Phys. Lett. **90** (2007) 191903.

[Zhang et al. 08a] R. F. Zhang, S. H. Sheng and S. Veprek, Acta Mater. **56** (2008) 4440.

[Zhang et al. 08b] R. F. Zhang, S. Veprek and A. S. Argon, Phys. Rev. B **77** (2008) 172103.

[Zhang et al. 09] R. F. Zhang, A. S. Argon and S. Veprek, Phys. Rev. Lett. **102** (2009) 015503; Phys. Rev. B **79** (2009) 245426.

[Y. Zhang et al. 05] Y. Zhang, H. Sun and C. F. Chen, Phys. Rev. Lett. **93** (2004) 195504; **94** (2005) 145505.

[Y. Zhang et al. 06] Y. Zhang, H. Sun and C. Chen, Phys. Rev. B **73** (2006) 064109.

[Y. Zhang et al. 06b] Z. C. Pan, H. Sun and C. F. Chen, Phys. Rev. Lett. **98** (2007) 135505.

[Zhao & Vanderbilt 02] X. Y. Zhao and D. Vanderbilt, Phys. Rev. B **65** (2002) 075105.

[Zhou et al. 03] M. Zhou, M. Nose, Y. Deguchi, T. Mae and K. Nogi, J. Vac. Sci. Technol. A **21** (2003) 1791.

[Ziambaras & Schröder 03] E. Ziambaras and E. Schröder, Phys. Rev. B **68** (2003) 064112.

[Zirinsky & Irene 78] S. Zirinsky and E. A. Irene, J. Electrochem. Soc. **125** (1978) 305.

[Zoroddu et al. 01] A. Zoroddu, F. Bernardini and P. Ruggerone, Phys. Rev. B 64 (2001) 045208.